CZECH TECHNICAL UNIVERSITY IN PRAGUE

Faculty of Nuclear Sciences and Physical Engineering

Department of Dosimetry and Ionizing Radiation

Doctoral thesis

Detection of Cosmic Radiation in the Atmosphere and Radiation Induced in Thunderclouds

Marek Sommer

2022

Summary

Measurement of cosmic rays onboard aircraft has been used to evaluate the aircrews radiation doses, to create models of radiation field in the atmosphere, to explore influences of space weather to radiation field in the atmosphere and to test new detectors. Due to the complexity of radiation field encountered onboard aircraft the comprehensive measurement is challenging. Moreover, often the size, weight and power consumption restrictions are imposed on radiation detectors onboard aircraft which makes the task even more challenging. This thesis introduces a concept of small, light-weight detector based on plastic scintillator which can be used in combination with silicon diode detectors to precisely measure dose equivalent without the need for correction factors based on the location. The characterization and calibration of the detector is described and dosimetric method is demonstrated on two flights.

It has been debated if passengers onboard aircraft and aircrews can be irradiated, apart from cosmic rays, by recently discovered rare phenomenon of Terrestrial Gamma Ray Flashes. Although it is very unlikely according to Monte Carlo simulations such events, can cause doses up to 1 Sv. Hence, the research of Terrestrial Gamma Ray Flashes is needed to quantify the likelihood of such severe events and to explore radiation field characteristics. This thesis introduces a detector based on liquid scintillators which focuses on detection of neutrons created by photonuclear reactions during Terrestrial Gamma Ray Flash. The focus on neutrons should increase the probability of detection of such event as the neutrons have larger lateral spread, range in the air and spread in time compared to electrons and photons that are also generated. The detector was placed at a high–mountain observatory at Lomnický štít and there are plans to place it on a coast in Japan where several Terrestrial Gamma Ray Flashes have been observed.

Acknowledgement

I am very grateful to many people who I would like to thank for their support, encouragement, and help, or simply for being there for me.
First of all, I would like to thank my supervisor: Ing. Ondřej Ploc Ph.D., who has always supported me and provided me with time and opportunity to grow into a better researcher who I believe I am today than I was at the beginning of my PhD studies. Thanks to him, I was able to visit many foreign countries, meet world experts in ionizing radiation research, and participate in various ambitious space projects. For that, I am very grateful to him. He is also a founder of the CRREAT project, which played an essential role in shaping this thesis and without it, this thesis would have probably never been written.
I am very grateful to my unofficial thesis advisor Dr. Eric R. Benton, who came up with the topic of this thesis and advised me during our consultations. He gave me the opportunity to learn from him and his students at a short internship at Oklahoma State University.
I would also like to thank the whole CRREAT project and to all the people who made it happen. This project allowed me not only to fund my research but also find my love in creative and technical work. Along with the CRREAT project, I thank all of my colleagues and friends at Department of Radiation Dosimetry, Nuclear Physics Institute, The Czech Academy of Sciences who I drank many coffees with, consulted countless issues, had numerous laughs and struggled through thousands of hours at meetings with.
I am very grateful to my family and friends who cared about me and kept asking me about my work to make me happy and also for helping me forget about my work.
Most of all I want to thank the love of my life, soon to be wife, Ing. Roberta Bimbová for her endless support, encouragement, and pep talks which have always boosted my determination. I have always felt her love. I hope that I have been providing her with similar support through her PhD studies. A special thanks goes to the best doggie in the world Bad who has spent years adorably sleeping by my side while I was working.

Bibliografický záznam

Název práce: Detekce kosmického záření v atmosféře a ionizujícího záření z bouřek

Autor: Ing. Marek Sommer

Studijní program: Aplikace přírodních věd

Studijní obor: Jaderné inženýrství

Školitel: Ing. Ondřej Ploc Ph.D., ODZ ÚJF AV ČR, v. v. i., Na Truhlářce 39/64, 180 00 Praha 8

Školitel specialista: prof. Ing. Tomáš Trojek, Ph.D., FJFI ČVUT , Břehová 7, 115 19 Praha 1

Akademický rok: 2022/2023

Počet stran: 127

Klíčová slova: Kosmické záření, detektory ionizujícího záření, Terrestrial Gamma Ray Flashes, scintilátory, tvarová diskriminace pulzů

Abstrakt: Měření kosmického záření na palubách letadel jsou používána na stanovení radiačních dávek posádek letadel, ke vzniku modelů radiačních polí v atmosféře, ke zkoumání vlivu vesmírného počasí na radiační pole v atmosféře Země a také k testování detektorů ionizujícího záření. Souhrnná měření na palubách letadel jsou složitá kvůli komplexitě radiačních polí a také kvůli omezením na váhu, velikost a spotřebu detektorů. Tato práce představuje koncept malého, scintilačního detektoru. Tento detektor může být použit v kombinaci s detektorem s křemíkovou diodou k měření dávkového ekvivalentu bez nutnosti použití korekčních faktorů závislých na pozici letadla. Výsledky z tohoto detektoru jsou ukázány pro dva lety spolu s popisem charkaterizace a kalibrace detektoru.
Podle posledních poznatků mohou být posádky letadel ozářeny kromě kosmického záření také zářením vznikajícím v jevu pojmenovaném Terrestrial Gamma Ray Flashes. Tyto jevy jsou spojovány s bouřkovou aktivitou. Z výpočtů vyplývá, že radiační dávka z těchto jevů by mohla dosahovat až 1 Sv. Ačkoliv Monte Carlo výpočty ukazují, že takovéto extrémni dávky jsou velice nepravděpodobné je nutné tyto jevy zkoumat, abychom mohli kvantifikovat pravděpodobnost podobných událostí a charakterizovat jimi generované radiační pole. Tato práce představuje detektor založený na tekutém scintilátor specializující se na detekci neutronů vytvořených fotojadernou reakcí během Terrestrial Gamma Ray Flash. Detektor byl umístěn na vysokohorskou observatoř na Lomnickém štítě a je plánováno jeho poslání na pobřeží Japonska, kde bylo pozorováno několik Terrestrial Gamma Ray Flashes.

Bibliographic Entry

Title: Detection of Cosmic Radiation in the Atmosphere and Radiation Induced in Thunderclouds

Author: Ing. Marek Sommer

Degree programme: Aplications of Natural Sciences

Field of Study: Nuclear Engineering

Supervisor: Ing. Ondřej Ploc Ph.D.

Supervisor specialist: prof. Ing. Tomáš Trojek, Ph.D.

Academic Year: 2022/2023

Number of Pages: 127

Key words: Cosmic rays, ionizing radiation detectors, Terrestrial Gamma Ray Flashes, scintillators, pulse shape discrimination

Abstract: Measurement of cosmic rays onboard aircraft has been used to evaluate the aircrews radiation doses, to create models of radiation field in the atmosphere, to explore influences of space weather to radiation field in the atmosphere and to test new detectors. Due to the complexity of radiation field encountered onboard aircraft the comprehensive measurement is challenging. Moreover, often the size, weight and power consumption restrictions are imposed on radiation detectors onboard aircraft which makes the task even more challenging. This thesis introduces a concept of small, light-weight detector based on plastic scintillator which can be used in combination with silicon diode detectors to precisely measure dose equivalent without the need for correction factors based on the location. The characterization and calibration of the detector is described and dosimetric method is demonstrated on two flights.

It has been debated if passengers onboard aircraft and aircrews can be irradiated, apart from cosmic rays, by recently discovered rare phenomenon of Terrestrial Gamma Ray Flashes. Although it is very unlikely according to Monte Carlo simulations such events, can cause doses up to 1 Sv. Hence, the research of Terrestrial Gamma Ray Flashes is needed to quantify the likelihood of such severe events and to explore radiation field characteristics. This thesis introduces a detector based on liquid scintillators which focuses on detection of neutrons created by photonuclear reactions during Terrestrial Gamma Ray Flash. The detector was placed at a high–mountain observatory at Lomnický štít and there are plans to place it on a coast in Japan where several Terrestrial Gamma Ray Flashes have been observed.

Contents

Chapter 1

Introduction

Pilots, flight attendants and air crews are exposed to elevated levels of cosmic ionizing radiation. Since the cosmic radiation consists of highly penetrating radiation the shielding is not a viable nor economic option for air transport operators. Therefore, the radiation doses of air crews are monitored and the precautions are implemented to affected personnel individually in the case of high radiation loads. For example the pilots can be recommended to serve flights with lower expected radiation doses or to spend less time in the air. Nowadays, the radiation load from cosmic radiation received by civilian aircraft personnel is expressed by effective doses calculated by computer programs. The programs are often based on Monte Carlo simulations of galactic cosmic rays propagating through air in the Earth's atmosphere. Various galactic cosmic rays models [1, 2] are used as input sources and they take into consideration various effects that influence the ionizing radiation doses such as location of the airplane, shielding of crew by the airplane structure, and Sun cycle [3, 4]. In rare cases of solar particle events that can influence the radiation doses at flight altitudes, the doses are assessed retrospectively based on the readings of neutron monitors [5].

The computer programs that can be legally used for assessment of aircrew doses, need to be verified by independent measurement or by comparison with reference data. The code is verified if the ambient dose equivalent agrees in a relatively broad range of 30% with the measurement or reference data [6]. The broad verification range is given mainly by complexity of the cosmic radiation in the atmosphere which makes it challenging to correctly determine the effective dose. The ionizing radiation field in the atmosphere consists of many particle types with a large range of energies.

The recent intercomparison measurement between various detectors and various groups shows that the variance of results is relatively large and in many cases the verification limit would be exceeded or barely passed [7]. This is especially significant for silicon-based solid state detectors. Similar results were obtained in another two intercomparison flights that were performed in 2021 [8]. These results suggest systematic error in measurement with silicon-based semiconductor detectors that do not agree with the computer programs.

Another way pilots and flight attendees can be theoretically irradiated is by ionizing radiation induced in thunderstorms. It was shown in recent years that ionizing radiation can be generated by a massive linear accelerator which is formed in thunderclouds. The electrified layers of thunderclouds act as a linear accelerator which accelerates charged particles, mainly electrons. Since it happens in the atmosphere filled with air the acceleration process has a condition that the drag forces (ionization of the air) must be lower than the acceleration forces influenced by the strength of the electric field in thunderstorms. Electrons slow down and generate bremsstrahlung. The photons are detected more often due to their longer range in the atmosphere compared to electrons. The resulting particle beams can vary in intensity and duration. Very short and intense bursts (short bursts or terrestrial gamma ray flashes - TGF) were observed at space [9, 10], onboard aircrafts [11] and on ground [12, 13] (so called downward TGFs). The long duration enhancements (long bursts or thunderstorm ground enhancements - TGE) were observed by several groups [14, 15]. The existence of downward TGFs is not accepted by all members of scientific society. Both of these phenomena are relatively new and they are not yet fully understood. Both short and long bursts have been observed together with enhancement in neutron fluxes. It was proposed that such radiation events (especially TGFs) might cause an increased radiation dose to aircraft passengers [16, 17]. Such events would be likely very rare as the plane would need to pass through the beam of accelerated particles but it cannot be ruled out. The most severe effects can be expected if the plane passes a very narrow beam of accelerated electrons which have not undergone the bremsstrahlung process. Such an event has the potential to cause mild radiation sickness. By extension the downward TGFs could also cause increased radiation load to people in thunderstorms. Since there has been only several TGFs registered on ground or in the airplanes, this thesis does not aim to investigate the radiation dose caused to passengers or people on the ground it rather focuses on designing a detector concept that would be able to detect such events, prove the existence of downward TGFs, extract as much information that could help to estimate the radiation dose and to help investigate the physical process that causes this phenomenon.

1.1 Goals

The complete set of aims and objectives of the thesis are:

- Understanding the limitation of semiconductor detectors in dosimetry in mixed radiation fields such as at flight altitudes of civilian aircrafts. Minimization of systematic error of silicon detectors which was observed in the intercomparison flights.
- Introduction of a detector design that would overcome the limitations of currently used detectors for aircrew dosimetry and that would complement them.
- Delivering proof of concept that the introduced detector can be used for verification of computer programs that are used for aircrew dosimetry and by

extension for research of space weather and its effects on the Earth's atmosphere.

- Designing a detector that is capable of measuring ionizing radiation generated by TGF and characterization and optimization of the detector.
- Testing of a detector intended for TGF measurement at a high-mountain observatory.

1.2 Author's contribution

Chapter 2 illustrates the cosmic radiation and its variations and origin, it also depicts the interactions of cosmic rays with the atmosphere and radiation fields in the atmosphere focused mainly on aviation altitudes of commercial aircraft.
Chapter 3 describes the dosimetry of cosmic radiation onboard aircraft. It focuses on descriptions of detectors historically used onboard aircraft and their limitations and capabilities.
Chapter 4 introduces the proposed detector for aviation dosimetry. It includes a characterization of the detector, dosimetric method, and results from flights.
Chapter 5 summarizes the known measurements of TGFs and describes the models that are a potential cause of this phenomenon. The focus is to describe the measurements that registered neutrons created by photonuclear reactions.
Chapter 6 describes the detector design and features for measurement of TGF. It describes the characterization and optimization of the detector and results from a short deployment at a high-mountain observatory in Lomnický štít.
Chapter 7 summarizes the results achieved in this thesis and future work on discussed topics.

Chapter 2

Cosmic radiation

Cosmic radiation was first discovered by Victor Francis Hess in 1912. Hess performed ten manned balloon flights during which he measured the dependence of atmosphere ionization using a Wulf type electroscope [18, 19, 20]. He observed an increase in the ionization rate as a function of altitude and concluded that this increase was caused by some sort of ionizing radiation arriving from space and penetrating into the atmosphere. Although the discovery of Hess showed the extraterrestrial origin of cosmic rays, their identity was unknown. The nature of primary cosmic rays was uncovered by Jacob Clay in 1927 who found out that the intensity of cosmic rays changes based on latitude [21]. This fact suggested that the rays were deflected by the magnetic field of Earth and therefore, they must be charged particles. Moreover, the directional experiments showed the so-called east/west effect which suggested that primary cosmic rays are positively charged particles [22, 23, 24]. Today, we have a much better understanding of cosmic rays' composition i.e. that they are primarily energetic protons, with a smaller fraction of energetic alpha particles and heavier nuclei. The cosmic radiation in Earth's vicinity can be separated into three sources based on their origin: (i) galactic cosmic rays (GCR) which are created in supernovae, galactic nuclei, and quasars, (ii) Solar energetic particles (SEPs) emitted by the Sun, and (iii) trapped radiation in radiation belts around Earth. Much more extensive reviews of cosmic rays can be found for example in [25, 26, 27, 28].

2.1 Galactic cosmic rays

Galactic cosmic rays are highly energetic particles which likely originate in explosions of supernovae and galactic nuclei. The energy range of such particles spans across ≈13 orders of magnitude (from 10^8 eV up to 10^{21} eV). The fluence of GCR monotonically decreases with increasing energy. The energy spectrum has two distinctive features called knee (≈4 PeV) and ancle (≈ 10^{19} eV). It is believed that GCR below 10^4 GeV are mainly generated in the explosions of stars into the interstellar medium [29]. The GCR with energy from 10^4 GeV up to $3 * 10^9$ GeV are produced by explosions of massive stars into their formal stellar wind [30, 31]. The physical mechanism responsible for acceleration of particles during supernovae

explosions is called Fermi acceleration and is described in [32, 33, 34]. The origin of the most energetic GCR is not fully understood. The low energy component of GCR with energies below 10 GeV undergoes solar modulation when entering the heliosphere. The heliosphere is a region that is occupied mainly by a solar wind which consists dominantly of ionized hydrogen and helium nuclei and electrons. The solar wind is electrically neutral plasma that travels with velocity of 300-800 km/s. The solar wind particles are accelerated by thermal energy and electrical fields that build up in the corona. That allows the solar wind to overcome the gravitational force of the Sun [35]. Since the solar wind is conductive it transports the magnetic field from the Sun. Due to the rotation of the Sun the resulting magnetic fields are shaped into spirals. There are three effects that modify flux of incoming GCR when entering the heliosphere. The first one is scattering due to irregularities in the magnetic field, second one is their drift towards the outside of the heliosphere and the third one is adiabatic cooling of the GCR due to the expansion of solar wind [27]. The solar wind can also interact with the magnetic field of the Earth creating a so-called magnetosphere. The magnetosphere imposes a cutoff for low energy particles. This effect varies as a function of geomagnetic latitude. The cutoff value is zero at magnetic poles and approximately 15 GV at magnetic equator for particles arriving vertically into the magnetic field. The solar activity may change the configuration of the magnetic field and therefore the cutoff conditions for cosmic rays. Based on the rigidity, and incoming direction of cosmic rays, the particles might be deflected or their energy might be fully absorbed in the Earth's atmosphere.

The solar activity undergoes several periodic variations. One of the variations has a periodicity of one solar day and it is called solar diurnal variation. It is caused by the rotation of the Earth. The diurnal variation has approximately sinusoidal shape with maximum at one hour after noon and minimum at midnight. The peak to peak variation is around 0.6%. The diurnal cycle has another component with the second harmonic frequency and much lower amplitude of 0.02% (semi-diurnal variation). Another variation is associated with rotation of the Sun which takes 27 days. One of the most significant solar variations is the Schwabe cycle (solar cycle) that has a period of 11 years and is anticorrelated with solar activity (often measured by number of sunspots). During high solar activity (many sunspots) the magnetic field in the heliosphere is stronger which causes that GCR are less likely to enter the heliosphere. Therefore the intensity of GCR measured on Earth is reduced. The peak to peak variation in neutron measurements on the ground is approximately 15%. An additional variation with periodicity of 22 years is linked to the reversal of the polarity of the Sun's magnetic field (Hale cycle). The minimum of Hale cycle is when the magnetic fields are aligned with one another and its maximum is when the magnetic fields are mixed up during the flipping of north and south poles of the magnetic field [25].

The composition of GCR is similar to the composition of matter in the solar system [36]. Most of the GCR is composed of fully ionized atomic nuclei, electrons, positrons and antiprotons. Most of the atomic nuclei are hydrogen and helium atoms but there are also all heavier atoms up to uranium. The knowledge of GCR composition decreases with the increasing energy because of the worsening statistics as the particles with higher energy are scarce [25]. Figure 2.1 shows the fluxes as a function of kinetic energy of some of the most abundant nuclei in cosmic radiation.

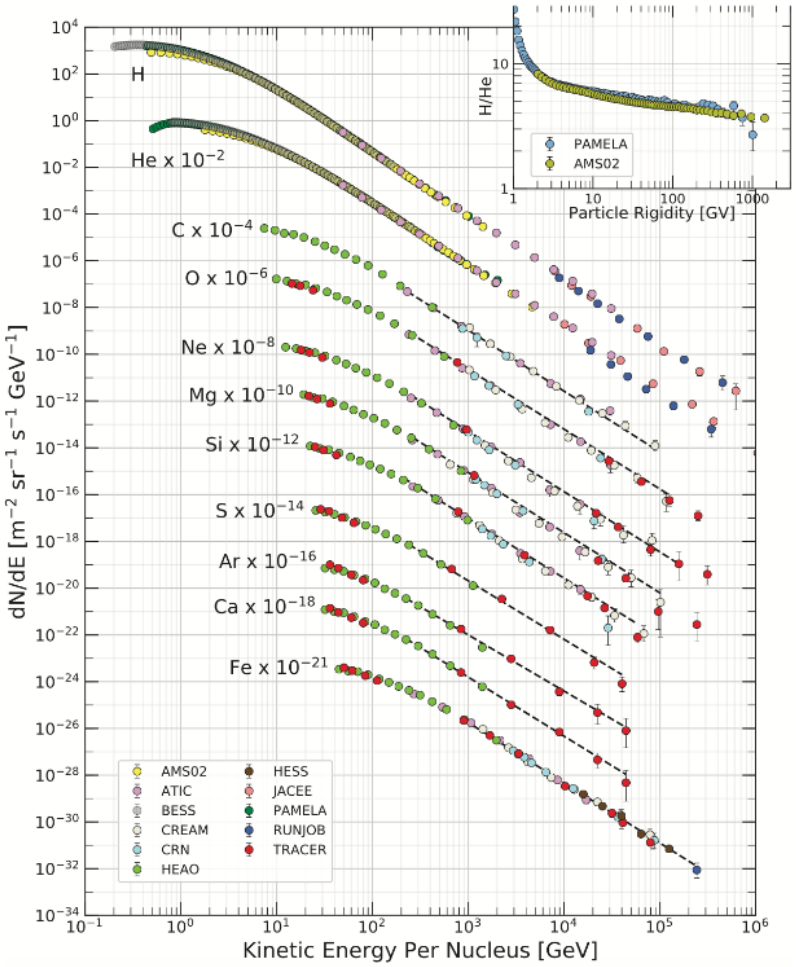

Figure 2.1: Flux of cosmic rays measured by satellites and high-altitude balloons. This picture was taken from [37].

Because the GCR are predominantly charged particles, they interact with magnetic fields present in interstellar space which causes the loss of directional information by the time they arrive in the vicinity of Earth. This makes it extremely difficult to trace the origin of cosmic rays back to a particular source, e.g. a supernova remnant. The temporal intensity of GCR is assumed to be stable with very little variation in the last millions of years [38].

2.2 Solar energetic particles

The solar energetic particles (SEP) are ionizing radiation particles emitted from the Sun during solar flares (SF) and coronal mass ejections (CME). The SF are localized eruptions of energetic particles on the surface of the Sun. The eruptions cover a small region of its surface and they are characteristic for their brightening. The SF takes from 20 minutes up to several hours. The SF are often accompanied by CME. The CME is a release of plasma into the heliosphere. The SEP emitted by SF and CME are mainly photons and charged particles such as protons, alpha particles, heavier nuclei and electrons but neutrons were also registered [25]. Two types of solar particle events have been classified - gradual and impulsive events. The duration of gradual events is usually several hours [39] and impulsive events typically last less than an hour [40]. It is believed that there are two mechanisms of acceleration taking place in SF and CME. The first mechanism is a shock acceleration which is a subclass of Fermi acceleration and is driven by a shock wave produced by CME. The second mechanism is assumed to be some kind of Fermi, stochastic, or electric acceleration generated by magnetic reconnection which is a process that converts magnetic energy into kinetic and thermal energy [41]. The energy spectrum of charged SEP typically extends up to 10 GeV, however particles with higher energies have been also detected. The energy spectrum of photons extends up to approximately 2 MeV. Neutrons that were registered in impulsive SF had energies up to 4 GeV. The fluxes of SEP can exceed the flux of GCR by several orders of magnitude. Therefore, the ionizing radiation released during solar particle events can be dangerous for satellites and humans [42, 43] which are not protected by Earth's magnetosphere.
Not all SF and CME can be observed on Earth or in its vicinity. The flux intensity of SEP depends on the strength of solar particle events and also on the location with respect to the location of the Earth. The flux of SEP can miss the Earth. The CME and SF can lead to so-called ground level enhancements (GLE) and Forbush decreases (FD). These are effects observed on the ground of Earth. The GLE is a rapid increase in the radiation dose which is caused by penetration of SEP to the atmosphere. GLEs are typically registered as an increase in count rates measured by neutron monitors and muon detectors that are placed around the globe. The GLE usually lasts from hours up to days. Another effect which is related to solar particle events is Forbush decrease which is a decrease in radiation dose from GCR. The FDs are caused by CME events that release plasma with higher velocity relative to the background solar wind. This generates a shock-sheat in front of the ejected plasma (magnetic cloud). As this structure propagates the interplanetary space it devoids GCR creating a GCR deficient region in the magnetic cloud region. When it reaches Earth it decreases the intensity of GCR [44, 45].

The FDs are classified into two categories - one step FD and two step FD. During the one step FD the Earth is hit by only the shock-sheat or only by magnetic cloud when the CME is not strong. During the two step FD the Earth is hit by shock-sheat and the following magnetic cloud. The illustration of both categories of FD are depicted in Figure 2.2 taken from [44]. The FDs can last up to several days and the associated decrease measured by neutron monitors can be up to 20% [25].

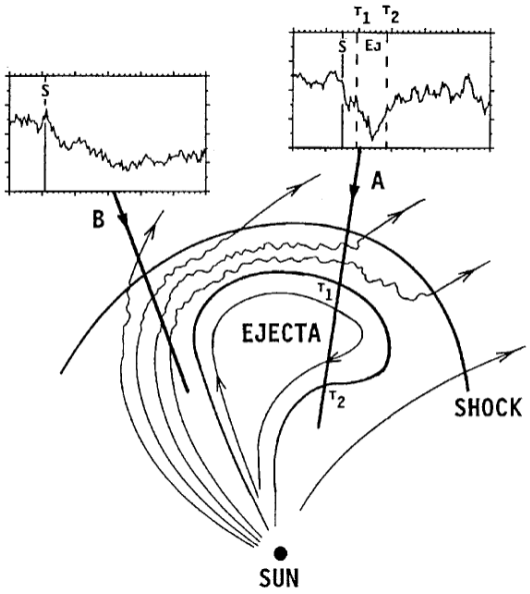

Figure 2.2: The illustration of one step and two step Forbush decreases [44].

2.3 Radiation belts

The radiation belt around Earth was first observed in 1958 by satellite Explorer I [46]. It was discovered that there are two radiation belts soon after - inner and outer. They are also called Van Allen's belts because James Van Allen was credited with their discovery. Both belts are doughnut-shaped and are a consequence of Earth's magnetosphere. There are spaces around Earth which allow the particles to stay trapped. The regions were anticipated in [47].
Inner radiation belt consists of trapped protons and ions (mainly alpha particles and oxygen) with energies up to 700 MeV. The particles are inputted by albedo neutrons that decay in the inner belt and by accelerated solar particles. The albedo neutrons are created by nuclear interactions of cosmic radiation with the atmosphere and redirected towards the radiation belts. Because they are without charge they can enter the radiation belts and decay into protons and electrons. The inner belt spreads from altitudes of 1000 - 12000 km.
The outer radiation belt consists mainly of electrons with energies 10 keV up to 10 MeV. The outer belt spreads from altitudes of 13000 - 60000 km. The flux of the trapped particles is $10^{10} - 10^{11}/cm^2/s$. The outer radiation belt is fed by solar particle events. Near polar regions the outer belts create so-called polar horns which are places where the outer belt is the closest to Earth [27].

2.4 South Atlantic Anomaly

The South Atlantic Anomaly (SAA) is a region of increased radiation in low Earth orbit (LEO). It is a place where the inner belt is the closest to the surface of Earth. The proximity is caused by the difference in the rotational axis alignment of the Earth and Earth's magnetic axis. The magnetic axis is tilted by 11° with respect to the rotational axis. The inner belt approaches the Earth surface as close as 200 km in the region of the South Atlantic of the coast of Brazil. Radiation doses in this region are much higher than doses in other places at LEO, making passage through the SAA potentially more dangerous for occupants of the International Space Station (ISS) and electronics of LEO satellites [25].

2.5 Interaction of cosmic rays with Earth's atmosphere, cosmic ray showers

Cosmic rays which overcome the barrier of the magnetosphere and enter Earth's atmosphere undergo interactions with the atoms of the atmosphere. High energetic particles collide with the atomic nuclei of the air. These nuclei can break up and produce many different types of particles such as neutrons, pions, kaons, antiparticles, etc. All particles lose their energy through hadronic and electromagnetic processes. The first interaction of protons with the atmosphere occurs after traversing roughly 1/15 of the total air mass of the atmosphere. For heavier particles the first nuclei collision occurs at even lower atmospheric density, i.e. at higher altitude [27]. The first interaction can trigger a hadronic cascade which creates more hadrons that interact with the atmosphere while creating even more hadrons and so on. Such created particles are pions, kaons, hyperons, charmed particles and nucleon-antinucleon pairs. The most abundant hadrons are π^0 mesons and $\pi\pm$ mesons. The π^0 mesons have very short lifetime and decay into two photons. These photons undergo mainly Compton scattering and pair production which create electrons and positrons. High-energy electrons and positrons produce new photons due to bremsstrahlung and positron annihilation.
Charged $\pi\pm$ mesons have a longer mean lifetime of $2.6 * 10^{-8}$ s and therefore are more likely to undergo nuclear collisions. When they decay, they produce muons and neutrinos. Muons have relatively short mean lifetime of $2.2 * 10^{-6}$ s but the majority reaches the sea level due to time dilation. Since muons are much heavier particles they emit less bremsstrahlung compared to electrons and positrons. That allows them to penetrate matter much deeper and reach the sea level. When muons decay they produce electrons, positrons and neutrinos.
The charged particles created in the cascade undergo electromagnetic processes such as bremsstrahlung, pair production and energy losses due to ionization and excitation of the atmosphere. All these mechanisms create a cascade of interactions which results in so-called cosmic ray showers - up to millions of particles which aim to the surface of Earth. In the case of a very energetic cosmic ray the shower is called an extensive cosmic ray shower. The primary high-energy particle interacts with the atmosphere which creates various types of particles which propagate further into

the atmosphere. The newly emerged particles propagate in a similar direction as the primary one. By the time they reach the surface they spread out to hundreds of meters. Many of the particles are attenuated by the atmosphere so they do not reach the Earth surface [26]. The illustration of cosmic ray showers is in Figure 2.3. The consequence of previously mentioned interactions is that the particle flux depends on the atmospheric depth. Therefore, in various altitudes the measured particle flux differs. The particle flux increases approximately up to 20 km and then slowly decreases. This maximum was firstly observed by Regener and his student Pfotzer in 1936 [48] and thus it is named after him as Regener-Pfotzer maximum.

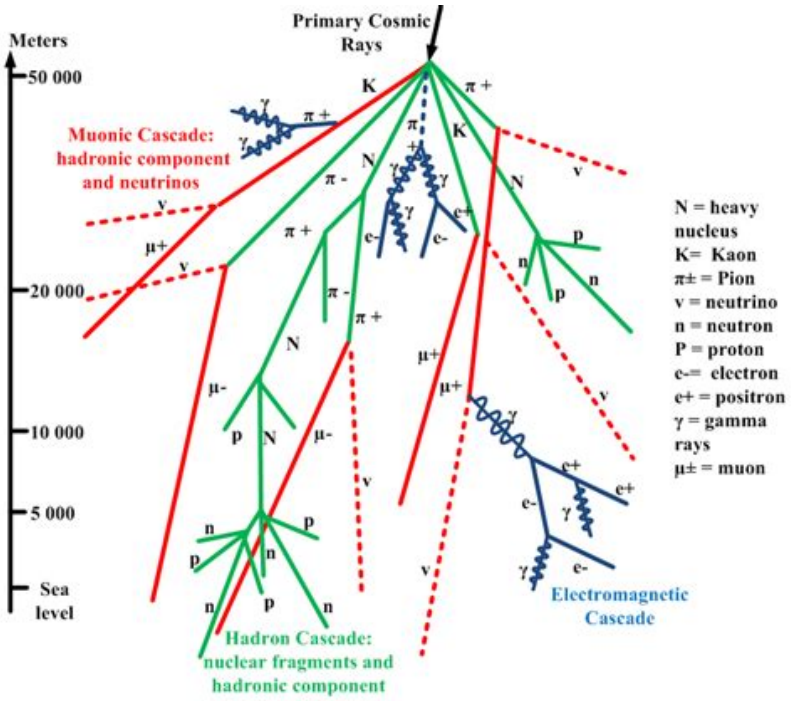

Figure 2.3: Illustration of the development of individual cascades in the air shower caused by a cosmic ray [49].

2.6 Mixed radiation fields in the atmosphere

The close vicinity of Earth is isotropically irradiated by high energy cosmic rays which create cosmic ray showers. That causes a complex mixed radiation field in the Earth's atmosphere. Although there are many different types of particles emerging from the interactions of cosmic rays with the atoms of atmosphere, there are eight particle types that make a significant contribution to effective dose - neutrons, protons, alpha particles, positive and negative muons, electrons, positrons, and photons. The effective dose is a variable that is used to evaluate the radiation risks to humans. It takes into consideration the radiation dose received by humans, the harmfulness of the different radiation types and different sensitivity of tissue (organs) to ionizing radiation.

The amount and composition of ionizing radiation in the atmosphere is a function of many variables - geomagnetic and heliospheric effects. The geomagnetic effects

that influence cosmic ray fluxes and energy spectra are latitude, longitude effects and east-west asymmetry. Moreover, the cosmic ray fluxes and energy spectra are significantly influenced by the altitude since the atmosphere provides a medium for proliferation of ionizing particles by hadronic and electromagnetic cascades as well as an attenuation shield that slows the ionizing radiation down. The latitude effect is caused by geomagnetic cutoffs that were discussed in section 2.1. The longitude effect is due to the asymmetry of the geomagnetic dipole axis with respect to the rotation axis of the Earth. The east-west asymmetry is caused by the fact that primary cosmic rays have predominantly positive charge and are therefore affected by Earth's magnetic field - some of the trajectories are forbidden. This causes for the cosmic rays arriving from the east side to be suppressed compared to the cosmic rays from the west side. The east-west asymmetry is more pronounced at the equator region whereas at higher latitudes its effect is greatly reduced. These factors and relationships are demonstrated in figures 2.4 2.5 2.6 2.7 2.8, they were created using the computer programs CARI-7A [50] and EXPACS/PARMA [51, 52]. CARI-7A and EXPACS/PARMA contain algorithms that can calculate the effective dose of cosmic radiation in the atmosphere. The effective dose was selected instead of absorbed dose because it is important for the reader to understand the overall changes in radiation risks to humans as a function of various geomagnetic and heliospheric factors.

Figure 2.4 shows the contribution of the eight particle types to the effective dose as a function of altitude (latitude and longitude of Prague, time close to solar minimum). It can be seen that contributions of different particle types change as a function of altitude. For example, the muon component is relatively significant at sea level but diminishes significantly at higher altitudes. Protons and alpha particles increase their effective dose rate and at approximately 20 km above the ground they become major contributors to effective dose. For commercial aircraft altitudes (up to 15 km) the largest contribution to effective dose comes from secondary neutrons. Although there are relatively small differences between results from CARI-7A and EXPACS, a slight change of internal parameters within models or use of other models can lead to significant changes in effective dose rates as was shown in [50]. This is especially pronounced at high altitudes (above 20km) where some models differ significantly. Figure 2.5 shows the distribution of effective dose around the Earth at the altitude of 12 km (calculated by CARI-7A model). It can be clearly seen that the effective dose in the vicinity of polar regions is significantly higher than at the equator (latitude effect). The longitude effect is visible in the region above North America where the effective dose rates are slightly increased. In order to understand the changes in contribution of individual particle types to effective dose at different locations, Figure 2.6 shows the normalized contributions as a function of latitude at altitude of 12 km. The neutron contribution to effective dose is influenced more by the latitude effect than any other particle type. Its contribution spans from 30% up to 55%. Almost the whole change in neutron contribution occurs in the latitude region between 30° and 60° which covers most of Europe and the USA. Similarly, in the same latitude region between 30° and 60° the effective dose increases rapidly. The time variation of cosmic rays is illustrated in Figure 2.7. The plot shows 34 years of time variation which is the length of approximately three solar cycles. The influence of solar activity on galactic cosmic rays strongly affects the effective dose

rate at the commercial flight altitudes. The second part of the plot shows change of the effective dose contribution from individual particle types. It shows that during the solar cycle the individual contributions of different particle types change slightly. Neutrons undergo the most significant change of approximately 5%. During solar maximum the contribution from neutrons, protons, and alpha particles rises whereas that from electrons, positrons, muons,and photons decreases. On the contrary during solar minimum the contribution from neutrons, protons, and alpha particles decreases whereas that from electrons, positrons, muons, and photons increases. This suggests that the solar cycle changes not only the intensity of cosmic ray radiation but also the quality of the radiation in terms of ratios between different particle types. The contributions are also plotted as a function of total effective dose rate in Figure 2.8.

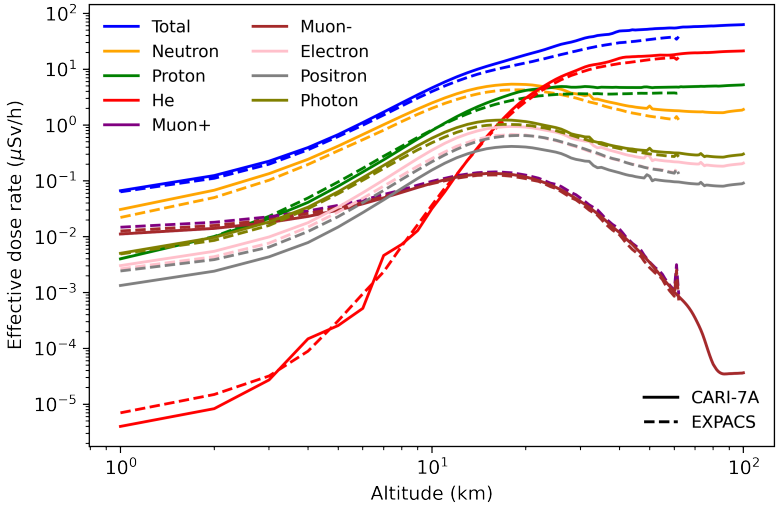

Figure 2.4: The contribution of individual particle types to the effective dose rate as a function of altitude. The latitude and longitude coordinates were fixed to Prague (50.09°, 14.42°) and date 01/01/2020. Results were calculated by CARI-7A and EXPACS software.

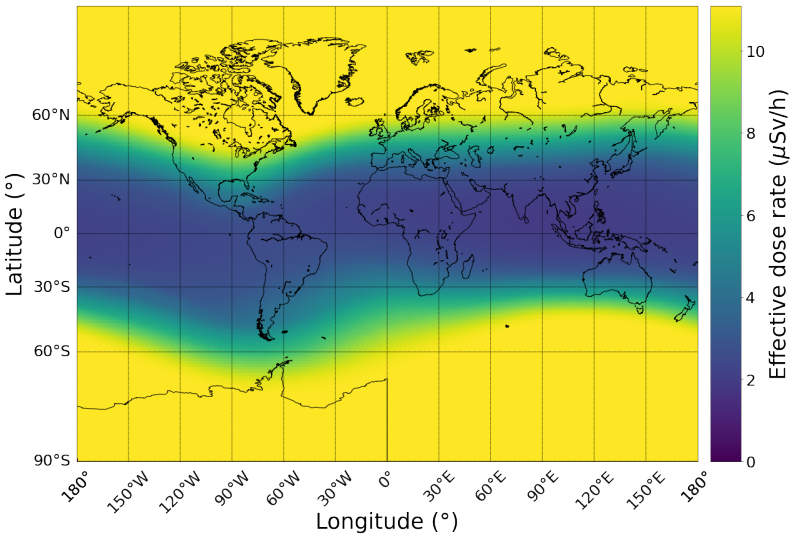

Figure 2.5: Map showing distribution of effective dose rates at altitude of 12 km around the world. The date was fixed to 01/01/2020. Results were calculated by CARI-7A.

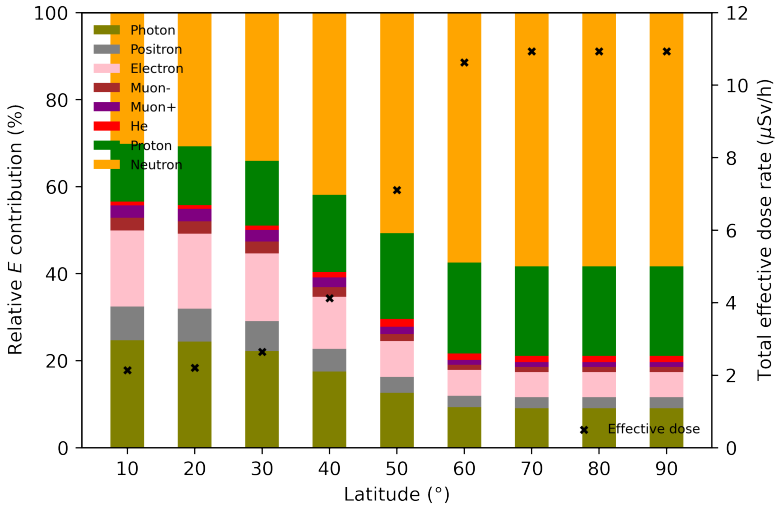

Figure 2.6: Relative contribution of eight different particle types to effective dose rate as a function of latitude at altitude of 12 km. The longitude was fixed to 14.42° at date 01/01/2020. Plot also shows the change of the absolute effective dose rate. Results were calculated by CARI-7A.

Figure 2.7: Top plot shows time series data of effective dose rate during 01/01/1986 - 01/01/2020 period (approximately 3 solar cycles) at the altitude of 12 km and coordinates of (50.09°, 14.42°). The bottom plot shows change contributions of different particle types to effective dose rate during the examined period. Results were calculated by CARI-7A.

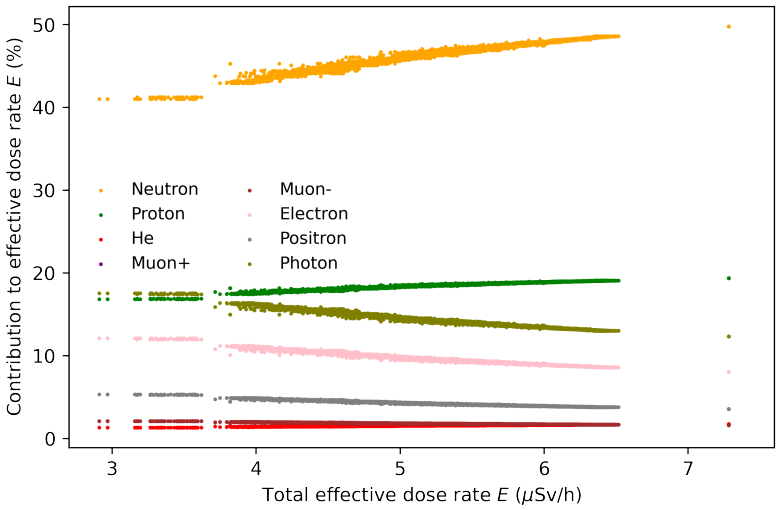

Figure 2.8: Contribution of individual particle types to effective dose rate as a function of effective dose rate. Data were taken from period 01/01/1986 - 01/01/2020. Other fixed parameters were the same as in Figure 2.7

Chapter 3

Dosimetry onboard aircraft

Given the complexity of the ionizing radiation environment present at aircraft altitudes as described in Chapter 2, the dosimetry at aircraft altitudes requires highly specialized instrumentation and measurement techniques.
In the last 30 years there have been many measurements onboard aircraft which were performed with various detectors and for various purposes. The purposes can be generalized into following categories: (a) characterization of the radiation field [53, 54, 55, 56, 57, 58], (b) as a part of the large databases [59, 60, 61, 62], and (c) for comparison of detectors or testing of the detector performance [7, 69, 70, 71, 72, 73, 74, 75, 76, 63, 64, 65, 66, 67, 68, 8], and (d) for other purposes [77, 78, 79]. Selected references about these measurements are summarized in Table 3.1. As can be seen in the table, most of the measurements are done with silicon detectors and tissue-equivalent proportional counters (TEPC). Some of the measurements were made with passive detectors - thermoluminescent detectors (TLD), track-etched detectors (TED), bubble detectors and other with less common detectors such as phoswich-type detectors and moderator-type neutron detectors.

The basic task of the active detectors used for dosimetric purposes is to measure the dosimetric quantity that reflects radiation risks for the humans. Typically the active detectors have similar concepts which are illustrated in the schematic model in Figure 3.1. The cornerstone of active detectors is a sensor that can collect the electric charge that is created in the sensor medium by the interactions of ionizing radiation with the medium. The medium can be for example silicon or gas. The electric current is induced by movement of charge carriers. Typically high voltage is used to put the charge carriers into the motion and to prevent the recombination of electron/ion pairs. The induced electric current pulses are transformed into voltage signals, amplified and shaped if necessary in the amplification circuitry. Usually, the charge sensitive amplifiers (CSA) are used as preamplifiers - conversion and amplification of current signal to voltage signal and Gaussian shaping amplifier are used for shaping and amplification of the voltage signal. The resulting voltage pulses are processed, analyzed and the useful information is saved or shown. Typically the amount of ionization in the sensor is proportional to a feature of the resulting pulse, e.g. height of the pulse, duration of the pulse. If the equivalency between absorbed energy and the number of created charge carriers is assumed (some of the energy might be used for the excitation processes, thermal and vibration movements, etc.)

Table 3.1: A list of onboard aircraft measurements.

Measurement	Detectors	Purpose	Number of flights
[7]	Si, TEPC, TLD	Comparison of detectors	1
[59]	Si	Database	213
[69]	Si, TEPC	Comparison of detectors	7
[70]	Si, TEPC	Comparison of detectors	1
[60]	Si	Database	3699
[53]	Si, TEPC, bubble det.	Characterization of radiation field	23
[77]	Si	Multiple	400
[78]	TLD	Assessment of radiation risks	Unspecified
[71]	Si telescope	Detector testing and characterization of radiation field	14
[72]	TEPC, TED	Comparison of detectors	Unspecified
[55]	Si	Space weather influence	35
[73]	Si, Si telescope	Detector testing	8
[74]	Si	Detector testing	12
[54]	Si, TLD, TED	Characterization of radiation field	494
[56]	TEPC	Space weather influence	>450
[75]	TEPC	Detector testing	74
[79]	Si	Effect of shielding by aircraft	10
[76]	Phoswich-type neutron detector	Detector testing	1
[63]	Si, TEPC	Detector testing	4
[64]	TEPC	Detector testing	4
[65]	Si	Detector testing	1
[57]	Si, TED	Effect of SAA on radiation doses	13
[66]	TED	Detector testing	5
[58]	Si, TEPC, GM	Space weather influence	10
[67]	Moderator-type neutron detectors	Detector testing	4
[68]	Si telescope, TEPC	Detector testing	28
[8]	Si	Detector testing	2
[61]	TEPC	Database	Unspecified
[62]	Si, (TEPC)	Database	42 (160)

the deposited energy due to ionizing radiation can be measured by a detector. This process is called energy calibration.

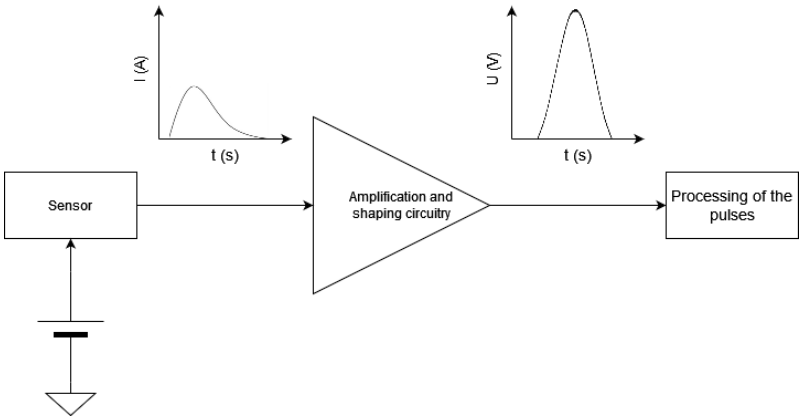

Figure 3.1: The schematic of general ionizing radiation detector concept.

In general each ionizing particle interacts differently with various materials so the material of the ionizing radiation sensor influences its sensitivity to different types of particles and different energies. Therefore, it is very difficult to design a single detector which would be able to sufficiently cover all particle types and energies especially in complex mixed radiation fields such as the ones in avionic altitudes. For dosimetry, there is an effort to use sensors that are similar in their composition to tissue so the interactions of ionizing radiation with the sensors are similar to those in the human body. In the following sections, three different detector types are discussed in further detail namely tissue-equivalent proportional counter, Si detectors, and phoswich-type detector.

3.1 Tissue-equivalent proportional counter

The TEPC is considered to be the most accurate detector for use in aviation dosimetry and is used as a reference detector for mixed radiation fields onboard aircraft. The TEPC is a detector made of low-pressure tissue-equivalent gas encapsulated in a tissue-equivalent plastic cavity (usually of spherical or cylindrical shape). The pressure of the gas is sufficiently low that the gas volume simulates mass of several cubic micrometers of tissue. The ionization of the gas caused by ionizing radiation is measured in a proportional counter. A high voltage anode wire runs through the center of the gas volume, while the walls of the cavity are electrically grounded. When an energetic charged particle passes through the gas volume, it collides with the electrons in the gas, producing electron/ion pairs. The electrons are then collected on the central anode wire. The primary reading from the TEPC is deposited energy that is then converted to lineal energy by dividing the deposited energy by the mean chord of the volume. Lineal energy is often considered as a sufficient approximation of linear energy transfer (LET) hence it can be used to calculate the quality factor of the incident ionizing radiation. The LET indicates how much the particle is able to ionize the environment along its path. The quality factor Q reflects the harmfulness of the ionizing radiation. Its value ranges from 1-30

and it is a function of LET [80]. Typically the radiation that can ionize the medium densely (heavy ions) will have higher Q value than ionizing radiation that produces electron/ion pairs scarcely (electrons). Since the active volume has very low mass the probability of interactions of neutrons and photons is very low. The neutral particles interact mainly with the plastic walls of the detector. Charged particles that are produced during these interactions can then enter the active volume and their lineal energy can be measured. It is important that the cavity walls of the TEPC have sufficient thickness to exceed the range of these secondary particles.
The main advantage of TEPC is that only a deposited energy calibration is needed to determine the dose equivalent as the radiation quality factor Q is calculated alongside the absorbed dose measurement. The dose equivalent is assumed as an adequate conservative estimate of the ambient dose equivalent. In addition the ambient dose equivalent is assumed to be a conservative estimate of effective dose which can be finally used to evaluate the radiation risks to humans onboard aircraft [4]. The energy calibration is usually performed on heavy ion beams and neutron beams such as ^{252}Cf [81]. The TEPC measurements are independent of the location in the atmosphere. It can measure the ionizing radiation up to LET of 1024 keV/µm. [82]. It has several minor disadvantages such as relatively large size (typically a size of a cabin luggage or a large shoe box), and usually the commercially available TEPC units do not last long when operated from battery (up to a couple of days) and commercially available TEPCs are expensive. It is also influenced by a microphonic effect which is caused by a vibration of the charged anode inside of the detector. A small vibration can induce enough electric charge which can influence the detector noise level. Moreover, it is not particularly sensitive to the low LET component of ionizing radiation as was shown in [83, 75, 84].

3.2 Silicon based detectors

The Si detectors have been used for all sorts of radiation detection and dosimetry purposes. Mainly they have proved to be useful for gathering data to the databases and analysis of the space weather influence on radiation doses received by aircrew and passengers flying onboard aircraft. One of the main features of Si detectors is their low power consumption which allows them to stay operational for a long period of time (up to couple of months) and small size of the detectors which makes them very portable and compact.
Commonly, the diode sensors of Si detectors have a thickness of several hundreds of micrometers and a surface of a couple squared centimeters. The Si detectors can be designed in monopixel configuration when the Si diode is read out as a whole or it can contain multiple analog and digital electronic circuits which leads to reading out the Si diode in pixels. In polypixel configuration the absorbed energy in each pixel is measured individually whereas in monopixel configuration the detector gives information about absorbed energy in the whole Si diode. An example of a monopixel Si detector is Liulin [85] and AIRDOS [86], an example of a polypixel Si detector is Timepix [87]. The advantage of polypixel Si detectors is that it provides additional information about energy deposit location within the Si diode and information about the properties of the radiation such as incident angle, LET can be partially derived

from the features of the clusters [88, 89]. The cluster is a group of neighboring pixels that have a nonzero absorbed energy. Another advantage is that it has much lower noise which leads to a lower detection threshold. The disadvantage of such detectors is that they are more power consuming and they can generate a large amount of data that needs to be saved compared to monopixel Si detectors.

3.2.1 Limitations of silicon based detectors in mixed radiation fields

Although Si detectors are often used for measurements in complex mixed radiation fields, they have a series of limitations which impact their accuracy and precision. The first type of limitations regards the energy calibration of monopixel detectors Liulin and Airdos. In various publications one set of energy calibration factors is used for different units of Si detectors. An illustrative example can be seen in the case of Liulin in which the commonly used calibration factors were derived in [90]. The same calibration factors are used in other research publications where different Liulin units were used [60, 91, 7]. This is because Si detectors like Airdos and Liulin need to be calibrated at particle accelerators using beams of suitable charge and energy, and because experiment time at such accelerators is extremely limited, it is often not possible to properly calibrate each and every individual Si detector. This has led to the use of Si detectors that were not individually calibrated and instead use calibration factors from other similar detectors. However, detectors made from identical components will nevertheless possess different sensitivity to radiation such that use of calibration factors measured for other instruments may lead to significant errors.
Related to the translation of calibration coefficients is the assumption of the same detection threshold of each detector unit. The first channels of Si detectors are influenced by the noise of the electronic which artificially adds counts to those channels hence overestimate the absorbed dose at low energies. In order to avoid that, the first channel that is not influenced by noise should be identified for each detector and the detection threshold of this channel should be determined. The amount of omitted absorbed dose onboard aircraft due to detection threshold was estimated in [8] and can be seen in Figure 3.2. This was done by analyzing the deposited energies obtained by the Timepix pixel detector with a very low detection threshold of only 5 keV. It was estimated that for detection threshold of 100 keV the omitted dose is approximately 15% whereas for detection threshold of 200 keV the omitted absorbed dose increases up to 40%. Ideally, the detection threshold should be below 50 keV in order to keep the omitted absorbed dose within 5%.

The magnitude of the errors caused by energy calibration and detection threshold identification can be seen in [7, 8] where the error in absorbed dose in Si measured by several Si detectors differs up to nearly 50%. That will eventually lead to large uncertainties in calculation of dosimetric quantities such as dose equivalent.
The second type of Si detector limitation is related to the different chemical composition of Si and tissue (water). This causes some of the interactions of ionizing radiation with the detection medium (Si, water) to be different. This is especially important for indirectly ionizing radiation such as photons and neutrons. In [92] it

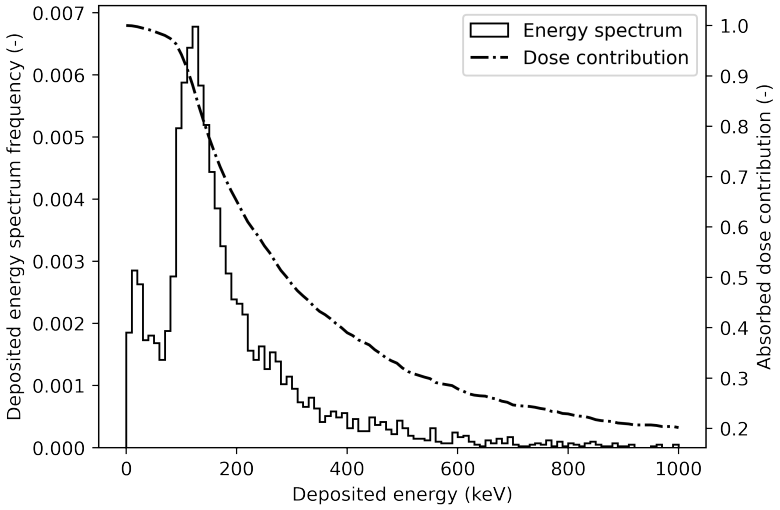

Figure 3.2: Deposited energy spectrum measured by Timepix onboard REFLECT flight [8]. The absorbed dose contribution curve shows the contribution to total deposited energy for energy deposits above the given detection threshold.

was shown that the absorbed dose from photons is overestimated by a factor of 2 and that the absorbed dose from neutrons is underestimated by a factor of 2.5 when measured in a Si as compared to a water detector. These systematic errors do not produce a significant error in total absorbed dose since photons and neutrons are not the main contributors to absorbed dose in the atmosphere (approximately up to 5% as was shown in [92]). Moreover, the recoil ions produced by elastic scattering of neutrons are different in each material and so is their LET [92].
The ionization rate in Si and tissue (water) is also different due to the different chemical composition which causes challenges in conversion of the energy losses between different materials. The rate of ionization in the material can be calculated by the Bethe-Bloch equation. It depends on the electron density of the material, the mean excitation energy of the material and the energy of the ionizing particle. Because silicon has a different electron density and mean excitation energy compared to water, the deposited energy in Si must be corrected using an appropriate conversion factor or conversion function. The most common approach is to use the constant conversion coefficient of 1.23 [68, 93, 94, 95, 60, 96, 79, 7, 59]. In [74] a conversion factor of 1.17 was used and 1.2 was used in [97]. The use of a conversion function was proposed in [92]. The proposed method is suitable for measurements which provide information about LET_{Si} such as measurement with Si telescopes [68] and partially measurement with Si pixel detectors [74]. The LET_{Si} is converted to LET_W by empirically obtained function by [98] and then the absorbed dose conversion coefficient can be approximated by equation:

$$k \approx \frac{LET_W}{LET_{Si}} * \frac{\rho_{Si}}{\rho_W} \tag{3.1}$$

where ρ_{Si} is the density of Si and ρ_W is the density of water. Use of this approach results not only in a more accurate conversion of LET from Si to water, but also in improvements in the dose equivalent calculation. High LET particles have a higher

absorbed dose conversion coefficient than particles of lower LET. This results in applying the quality factor to a larger absorbed dose. If the mean absorbed dose conversion coefficient is used, the dose equivalent might be underestimated as shown in [92].

3.2.2 Energy calibration methods of silicon based detectors

The following text lists various energy calibration methods of Si detectors. The precision of energy calibration is crucial for correct assessment of radiation risks. Nevertheless, the recent results showing large discrepancies (up to 50%) in absorbed dose in Si among different Si detectors suggest an extensive problem in this area [7, 8]. A partial solution to this problem was introduced in [8] namely by proposing a new simple energy calibration method using a pixel detectors Timepix. This method does not require a particle accelerator and can be easily performed.

Heavy ions

The standard method of energy calibration of Si diode detectors has been to use high-energy heavy ion beams of known LET produced in particle accelerators. Heavy ions with known LET travel through the Si diode of known thickness. This allows a precise calculation of the total deposited energy in the Si detector. The total deposited energy is linked to the response of the Si detector. This method was used in [90, 86]. Although this method is relatively simple, it requires access to a charged particle accelerator which is often difficult to obtain. This is the main reason why one set of calibration coefficients obtained for a particular individual instrument is used with other instruments of the same detector model. Another disadvantage is that heavy ions tend to deposit large amounts of energy (hundreds of keV within the Si detector) hence it is more challenging to sample the beginning of detector range (the first channels around 100-300 keV). Therefore, the range of the first several channels is usually extrapolated, and the detection threshold is determined from the extrapolation. This method does not allow to evaluate the effect of noise which might contribute to the first channels, and it can cause false detections. To bypass this problem the first channels are usually discarded but there is no clear guidance on how many channels to discard and how to evaluate which channels and how much they are influenced by the noise.

Charge injection

The approach proposed in [86] uses injection of a known amount of charge into the CSA and analyses the output of the amplifier. The charge can be recalculated to deposited energy. The advantage of this method is that any amount of charge can be injected into the CSA, therefore, the calibration curve can be sampled in the whole range. Similarly, as heavy ion calibration, the charge injection does not allow us to evaluate the effect of noise.

X-rays per-pixel calibration

The energy calibration of polypixel detectors such as Timepix is done per-pixel by low energy gamma rays generated by characteristic fluorescent X-rays from radionuclides (Fe and In) and gamma rays from radionuclide decay (^{241}Am) [99]. Since the individual pixels have much smaller surface than Si diodes, they have much lower capacitance which results in much lower noise. Therefore, the detection threshold of such detectors is approximately several keV. That allows the detectors to be calibrated by low energy X-rays and gamma rays. Timepix detector provides information about time which voltage signal spends above a given threshold (time over threshold) for each pixel. If the X-ray of known energy is absorbed in a single pixel then the response can be linked to the exact known deposited energy. The calibration function of one pixel is shown in Figure 3.3. The calibration function can be extrapolated approximately up to 850 keV/px [99]. Above this level the corrections need to be made as was shown in [100, 101, 102, 103]. This method cannot be used for monopixel Si detectors with large surface diodes such as Liulin and AIRDOS because their detection threshold is above the energy of typically used X-rays. The use of more energetic radionuclides is not feasible because the generated electrons may escape from Si diode due to its low thickness and an unknown part of the energy may be lost.

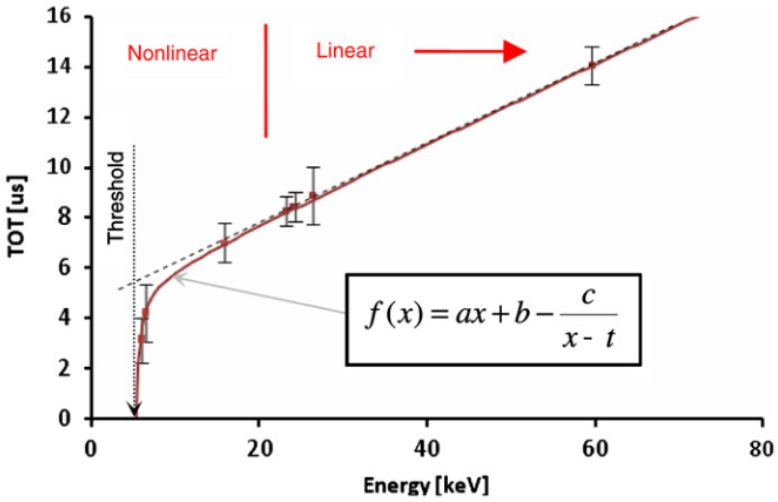

Figure 3.3: The calibration function of a Timepix detector pixel. The four parameters calibration function is used to describe the relation between time over threshold and deposited energy [99].

Comparative calibration of Si diodes

This method was developed for calibration of monopixel Si diodes such as the ones used in Liulin and AIRDOS. It is based on the comparison of deposited energies measured by Si diode and Timepix pixel detector onboard aircraft [8]. Since Timepix detectors have a much lower detection threshold and superior energy resolution to Liulin and AIRDOS, this method allows the investigation of the calibration coeffi-

cients of the Si diode in low range (up to the first 10-20 channels), which precisely determines the detection threshold of the detector and determines the contamination of the first channels by noise. Therefore, this method compliments the heavy ion calibration and charge injection methods as it gives additional information about the calibrated detector. The results of this calibration method tabulated in Table 3.2 show that the translation of calibration coefficients from one unit to another results in large errors in calibration.

Table 3.2: A comparison of calibration coefficients obtained by the original calibration methods and a newly developed comparative calibration method introduced in [8]. The calibration factors are shown in format [a, b, T] where a is a linear coefficient, b is a constant coefficient of the calibration and T is the detection threshold.

Detector	Original calibration method	Original calibration coefficients	New calibration coefficients
Liulin MDU10	Heavy ions*	[81.3, 81.3, 40.7]	[47.0, 130.9, 107.4]
Liulin MDU15	Heavy ions*	[81.3, 81.3, 40.7]	[61.0, 157.9, 127.4]
AIRDOS DD	Charge injection	[38.0, 181.0, 162.0]	[41.0, 220.7, 200.2]
AIRDOS 98	Charge injection*	[38.0, 181.0, 162.0]	[29.0, 190.1, 175.6]

3.2.3 Ambient dose equivalent calibration methods of silicon based detectors

The calculation of dose equivalent from absorbed dose in silicon, which is natively measured by Si detectors, needs a calibration coefficient or a function. As was shown in Chapter 2, roughly 30-55% of effective dose is caused by neutrons which produce recoil particles with large LET hence large quality factor. Since the Si detectors have no way to identify the energy deposits caused by neutrons it is not possible to evaluate the quality factor Q of such deposits. And even if the Si detector could identify neutrons the LET of recoil particles would be different than in water due to different interactions with Si and water. For this reason the Si detectors are insensitive to neutrons in terms of dose equivalent even though the Si detectors are sensitive to neutrons in terms of absorbed dose. That is the main reason why calibration methods for dose equivalent often use corrections for position (altitude and latitude) determined by TEPC measurements. The geomagnetic altitude and latitude are the main drivers of neutron doses as was shown in Chapter 2. Although such corrections are widely used, it requires measurements of additional information about position. The position corrections also limit the usage of such measurements. For example the short term changes in the cosmic radiation environment caused by solar CME which would cause a significant increase in dose equivalent from neutrons would likely be missed by Si detectors. Such an event would cause only a small increase in absorbed dose in silicon and would be multiplied by a dose equivalent calibration factor determined by TEPC in normal conditions (without the CME). Hence there would be very little change in overall absorbed dose and no detected changes in the quality of the radiation field. Therefore, detectors that use correction coefficients derived from geomagnetic location and altitude cannot

reflect the changes in the quality of the radiation field. In this sense, the quality does not mean only the energy spectrum of individual types of ionizing radiation, but also their absolute fluences. Higher flux of high LET particles (for example recoil ions from neutrons) changes the overall mean quality factor as well. These changes can be caused by cosmic weather, solar particle events, cloud coverage, mass of the plane, fuel reduction, etc. Therefore, Si detectors are not natively suitable for research activities apart from long term verification of the models. As the neutron component is the one that is the most variable of all ionizing radiation particles in the atmosphere, it seriously limits the potential of the Si detectors. This insensitivity to neutrons (inability to identify neutrons and determine the quality factor of recoil ions) is a very significant downside of Si detectors which is not present in TEPC. Therefore, the TEPCs are more suitable for the measurement in mixed radiation fields in the atmosphere than Si detectors. In the following text the brief description of dose equivalent calibration methods is presented. Some of the described methods attempted to identify the neutron component and bypass this downside.

Field calibration factor

Field calibration method uses an analytical computer code FDOScalc [97] that is based on the database of TEPC measurements onboard aircrafts [61]. The database consists of around 2500 data points taken in the years 1997-1999 and 2003-2006. The FDOScalc can calculate dose equivalent for a given vertical cut-off rigidity. The calibration factor for Si detector is then calculated as the ratio between dose equivalent calculated by FDOScalc and absorbed dose in Si. It uses correction for the Solar cycle based on Neutron Monitor counts at Oulu [104]. This method requires the knowledge of geomagnetic position to calculate vertical cut-off rigidity. The calibration curve for three different Si detectors as a function of vertical cut-off rigidity can be seen in Figure 3.4. The resulting calibration coefficient ties the Si detector to the FDOScalc model. This method was used in [86, 97, 105, 106].
The advantage of this method is that it is relatively simple and it is independent of energy calibration method or its precision. Even if the absorbed dose in Si is measured incorrectly, the resulting dose equivalent will not be affected. The detector does not even need to be calibrated and only raw channels can be used for the calculation. This method might be also suitable for simple detectors such as Geiger-Müller type.

Mean quality factor

This method is based on a large number of measurements with TEPC. It uses the mean quality factor of the radiation field as a conversion to dose equivalent. The mean quality factor is calculated as a dose equivalent divided by absorbed dose in water. The mean quality factor was fitted in the whole range of vertical cut-off rigidity. The function can be seen in Figure 3.5. The calibration coefficient can be applied to the absorbed dose measured in water. Since the Si detectors measure the absorbed dose in Si, it is necessary to convert it to the absorbed dose in water. The

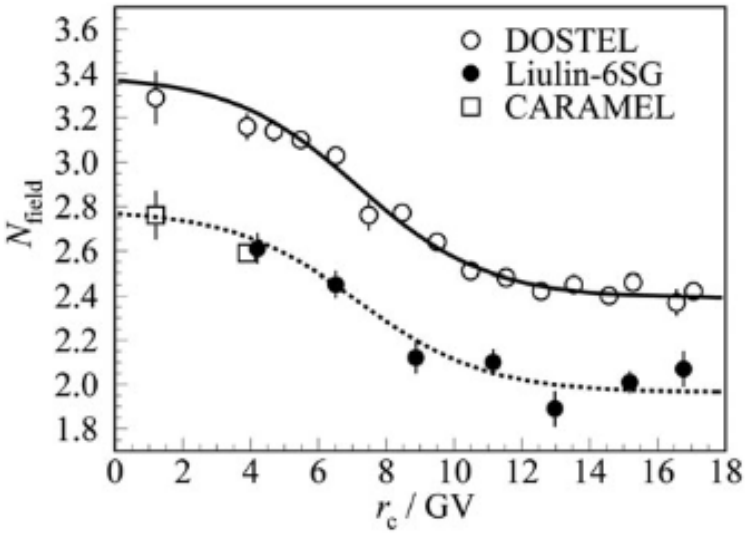

Figure 3.4: The field calibration factor plotted as a function of vertical cut-off rigidity [106].

knowledge of geomagnetic location and altitude is needed to calculate the vertical cut-off rigidity. This method was introduced in [62].

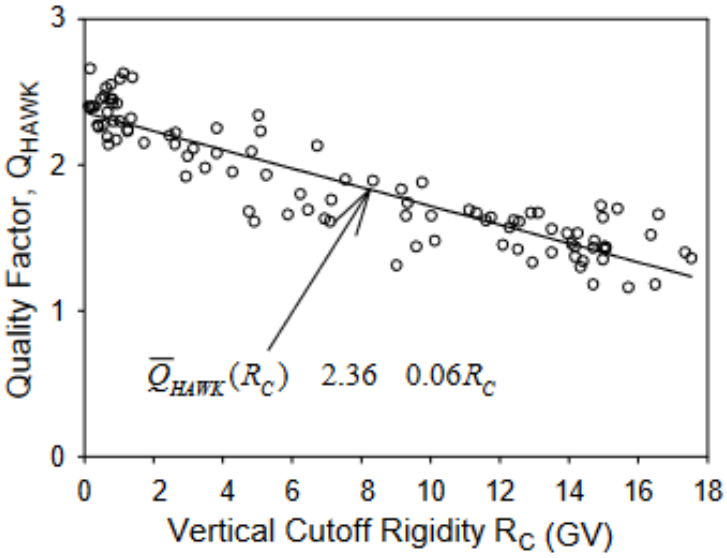

Figure 3.5: The mean quality factor determined by TEPC measurements as a function of vertical cut-off rigidity [62].

Neutron discrimination method

This method is based on discrimination of the neutron component. It is assumed that all energy deposits larger than 1 MeV are caused by neutron interactions in Si. Energy deposits lower than 1 MeV are considered to be the low LET component. The calibration factors k_{low} and k_{neu} were calculated from comparison measurements

performed at CERF [107]. The radiation in CERN provides neutron reference with similar characteristics as the radiation field at avionics altitudes. The calculation of dose equivalent is done according to the equation:

$$\overset{*}{H}(10) = k_{low}D_{low} + k_{neu}D_{neu} \tag{3.2}$$

where D_{low} is absorbed dose with deposits lower than 1 MeV and D_{neu} is absorbed dose with energy deposits larger than 1 MeV.
This method performed relatively well in polar regions [108], but it had large differences compared to algorithms for aircrew dosimetry in equatorial regions. Therefore, [109] proposed a modification of this method. The calibration coefficients k_{low} and k_{neu} were parameterized based on the ratio of D_{low} and D_{neu}. This modification led to better agreement between Liulin measurements onboard aircrafts and calculations of EPCARD software. This method relies on the ability to discriminate between neutrons and other ionizing radiation. The elastic scattering of fast neutrons of Si can be approximated by the equation described in [110]:

$$T_a = (\frac{4m_n m_a}{(m_n + m_a)^2}\cos^2\omega)T_n \tag{3.3}$$

where T_a is the energy of the recoil atom, T_n is the energy of a neutron, m_a is the weight of a_n atom, and m_n is the weight of a neutron and ω is scatter angle. This equation suggests that only neutrons with energies greater than 7.5 MeV (frontal collision) can deposit more than 1 MeV in Si diode. Since the neutron spectrum in aviation altitudes has major components in regions of 2 MeV and 100 MeV, many neutrons are misclassified as low LET components as their deposited energy is below 1 MeV. Similarly, the low LET particle can deposit energy larger than 1 MeV. It has never been clearly demonstrated what portion of particles is misclassified. The measurement performed with the Timepix detector [8] suggests that relatively large portions of energy deposits greater than 1 MeV are in fact different types of particles. The data from Timepix show that roughly 20% of absorbed dose is caused by particles with energy deposits greater than 1 MeV whereas in [92] it is shown that neutrons are responsible only for 3% of absorbed dose. Moreover, those 3% consist of neutrons with energies lower than 7.5 MeV. Therefore, the assumption that is used for discrimination of neutrons (the 1 MeV limit) does not seem justified. Another problem with this method is that it uses the CERF as a reference for calibration. The CERF facility serves as a reference only for neutron component and not all particle types that occur in aviation altitudes.

Direct calculation of dose equivalent

Dose equivalent can be also calculated directly. It has been done several times in [62, 96, 74, 68]. The direct calculation is based on the determination of LET in water which can then be recalculated into quality factor [111].
The LET in Si can be measured by single diode detectors [62]. In [62] each Liulin channel is assigned a LET value which is based on the comparison of the lineal energy spectrum measured by TEPC. Such procedure does not seem to be justified

from same reasons as the discrimination of the neutrons cannot be done by simple analysis of the deposited energy. Moreover, the neutron interactions in water and in Si produce different charged particles with different LET values. Another possibility is to use a Si pixel detector [74, 96] that can analyze the clusters of deposited energies and determine the incident angle of the particle which improves the estimation of track length [112, 113]. This allows to determine LET of particles that traverse the thin Si slab. Another example that used the direct calculation of dose equivalent is Si telescope [68]. The Si telescopes use two or more layers of Si diodes in coincidence mode. They can estimate the track length due to the geometry of the individual Si layers.
The [68] reported the mean quality factor of 1.37 whereas the mean quality factor measured by TEPC is approximately in the range of 1.28-2.36 (in the range of vertical cut-off rigidity up to 18 GV) reported in [62]. Hence, the quality factor measured by the Si telescope is underestimated compared to the TEPC measurements. This difference is mainly attributed to fast neutrons. Since the recoil Si atoms that are produced during elastic scattering of neutrons have a range of several micrometers in Si, they will not travel through several layers of Si diodes The theoretical calculation performed in [92] shows a mean quality factor of 1.06 in a single Si layer compared to 1.37 measured in [68]. This difference might be due to the selective effect of the Si telescope. The detections that trigger 2 or more Si layers might favor the high LET particles. Electrons, positrons and other low LET particles can be scattered by the first encountered Si layer and never enter the second layer. That would cause overestimation of the mean quality factor. The presented results show that although using a Si telescope can be used to evaluate the mean quality factor, its results are significantly underestimated due to the large contribution of fast neutrons to dose equivalent.

3.3 Phoswich-type detector

Phoswich-type detector for measurement of photon and neutron components is composed of a large liquid scintillator EJ-309 with pulse shape discrimination (PSD) and with a plastic scintillator EJ-299-13 surrounding the liquid scintillator which has much longer decay time than EJ-309. The phoswich-type detector is able to discriminate between neutral particles and charged particles based on the pulse shape. If the particle deposit energy in a plastic scintillator, it will appear as a pulse with long tail since the EJ-299-13 has a decay time of 285 ns whereas EJ-309 has a decay time of 3.2 ns. Moreover, the neutral particles that deposit energy only in liquid scintillator (without a long tail) are discriminated due to PSD. The PSD technique allows to analyze the features of pulse shape and to calculate the PSD parameter. Based on the value of the PSD parameter, the neutron and photon components can be discriminated. Hence it is possible to discriminate neutrons from photons. This concept allows to measure deposited energy spectra of neutrons and photons and perform convolution to determine the primary energy spectra of photons and neutrons. Downside of this detector is its large size, large power consumption and a need for skilled operators. This detector and its application in aviation dosimetry was introduced in [76].

3.4 Remarks

The aviation dosimetry is typically performed by TEPC which can provide precise dose equivalent data. Unfortunately, their mass deployment onboard aircrafts is limited by their size, limited battery operational time and their cost. For these reasons a large number of measurements are performed by cheaper and more compact Si detectors which have a series of their own downsides that were described in this chapter. Therefore, there is a need for a detector for aviation dosimetry that will combine the strengths of TEPC and Si detectors - tissue equivalent detector, no need for additional position measurement, small size, and not expensive. The concept of such a detector inspired by the phoswich-type detector will be introduced in the Chapter 4.

Chapter 4

Plastic scintillator based detector of cosmic rays

The main idea of the proposed detector is to use the scintillator which composition is close to tissue equivalent and can discriminate ionizing radiation particles based on LET. The scintillators are manufactured in order to contain large amount of unbound π-electrons that can be easily excited by the ionizing radiation. Such electrons can be excited in one of many excitation states (S_1, S_2, etc.). These states emit photons during their deexcitation (fluorescence). This process is very fast and the deexcitation happens within a few nanoseconds after the excitation [114]. The competitive process that can happen with S states is that it undergoes a spin reversal into triplet state T. That can lead to emission of photons with longer wavelengths than the deexcitation of S states. The triplet states can also be transformed back to S state by gaining enough thermal energy or by interaction with another triplet state. This interaction leads to one electron in ground state S_0 and the other one in S_1 state. The subsequent deexcitation of S_1 state leads to delayed fluorescence. The density of triplets is influenced mainly by the ionization rate of the incident particle. Hence, the particles with large LET produce more delayed fluorescence than particles with low LET [115]. Therefore, the resulting pulses have different shapes. Some of the commercially available scintillators are synthesized to enhance the production of triplet states to exploit this property. The example of difference between pulse shapes is illustrated in Figure 4.1. Typically, the PSD is used to discriminate between photons and neutrons. The PSD algorithms that analyze the pulse shapes perform better for larger pulses hence discrimination typically works for neutrons depositing energy of approximately 1 MeV.

Since most of the high LET component in flight altitudes is caused by neutrons the proposed detector should be suitable for aviation dosimetry. The concept of the proposed detector should distinguish between neutrons and low LET component, calculate the deposited energy of both components and assign a corresponding quality factor to them. The specifics of these steps will be discussed later in this chapter.

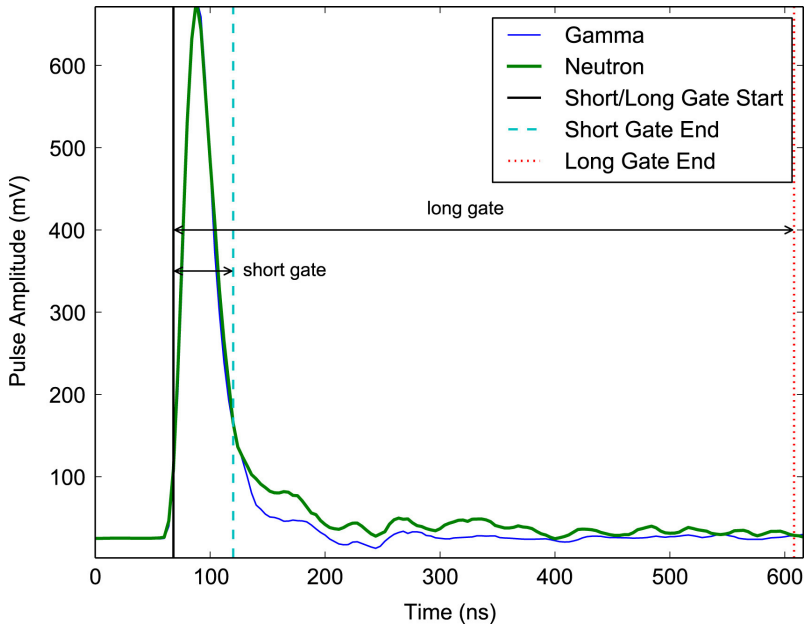

Figure 4.1: The illustration of photon and neutron pulse measured on plastic scintillator EJ-299-33 [116].

4.1 Hardware design

The design of the detector is based on the plastic scintillator EJ-276 [117] that supports PSD technique. The major features of the EJ-276 scintillator are tabulated in Table 4.1. The visible light produced in the EJ-276 by ionizing radiation is collected by four silicon multipliers (SiPM) MicroFC-60035 [118]. The SiPMs were chosen instead of more traditional photomultiplier (PMT) tubes to achieve small size and low weight of the detector. Moreover, PMTs need a high voltage power supply of several hundreds of volts whereas SiPMs can be operated with a bias voltage of several tens of volts. The summary of the main features of MicroFC-60035 SiPM is in Table 4.2. The design of the detector utilizes four SiPM units that are connected in parallel and their output is summed up together. The photographs of the plastic scintillator, SiPMs and the assembly of the plastic scintillator coupled with SiPMs can be seen in Figure 4.2, Figure 4.3, Figure 4.4, respectively. The pulses which are generated by SiPMs are amplified in amplification circuitry and processed in digital circuitry, namely field programmable gate array (FPGA). The detector can be powered through the FPGA printed circuit board (PCB) via universal serial bus (USB) or by any stable +5 V power supply with sufficient current. The prototypes of the detector use real time clock (RTC) to keep track of the time and it can also accept messages from global positioning system (GPS) via universal asynchronous receiver-transmitter (UART) communication.

4.1.1 Silicon photomultiplier

SiPM is a semiconductor device consisting of an array of single-photon avalanche diodes (microcells) biased over the breakdown voltage. The electron avalanche pro-

Table 4.1: The tabulated properties of EJ-276 plastic scintillator.

Parameter	EJ-276
Size (mm x mm)	25.4 x 25.4
Density (g/mm^3)	1.096
Scintillation efficiency (ph/MeVee)	8600
Wavelength of maximum emission (nm)	425

Table 4.2: The tabulated properties of MicroFC-60035 SiPM.

Parameter	MicroFC-60035
Breakdown voltage (V)	25.45
Capacitance (pF)	3400
Number of microcells (-)	18980
Wavelength of maximum absorption (nm)	420

Figure 4.2: Photograph of the EJ-276 scintillator.

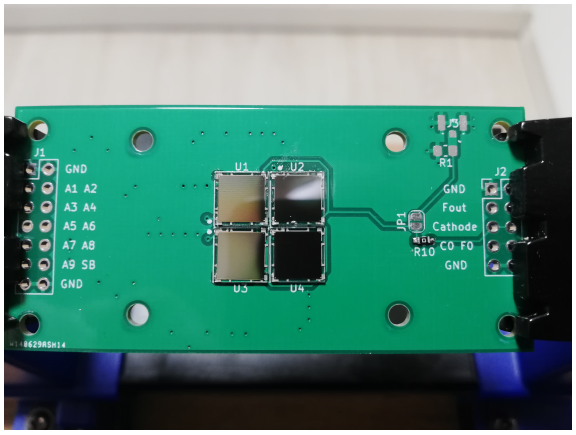

Figure 4.3: Photograph of four MicroFC-60035 SiPMs soldered on a PCB.

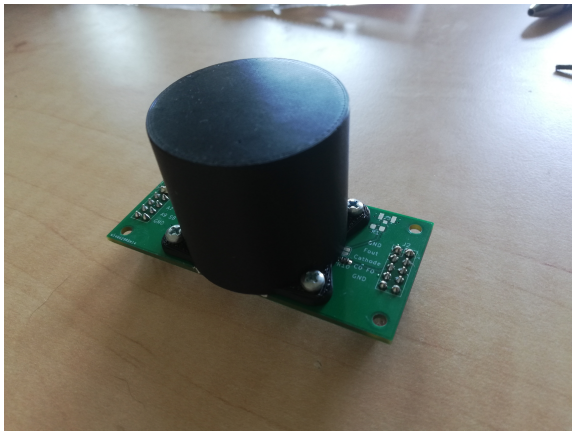

Figure 4.4: Photograph of EJ-276 coupled with SiPMs. The plastic scintillator is encapsulated in a 3D printed holder.

duced during microcell ignition is quenched by in-series passive resistance. Due to high gain of the avalanche, the output current signal is sufficient for the detection of single photons. The SiPMs offer several advantages over PMTs, typical for the silicon devices – they are small, compact, insensitive to magnetic fields, and do not require a high voltage power supply. On the other hand, large surface SiPMs have large capacitance, and this might pose a challenge when designing front-end electronics. The large capacitance of SiPMs in parallel with a load resistor works as a low-pass filter that influences the output pulse waveform. The bandwidth can be calculated according to the following equation:

$$f_{3dB} = \frac{1}{2\pi RC} \tag{4.1}$$

Where R is load resistance and C is the capacitance of the SiPM. The front-end electronics design is usually based on a load resistor, a transimpedance amplifier, or a bootstrapped transimpedance amplifier [119, 120]. The designs based on transimpedance operational amplifiers can increase the bandwidth while maintaining the same amplification. The disadvantage of designs based on operational amplifiers is that they introduce additional noise to the signal. Another complication for signal processing, when a SiPM is used, might be the recovery time of microcells, which affects the fall time of the signal (up to hundreds of nanoseconds) compared to PMTs, where the fall time of the pulse is in the order of nanoseconds. The recovery time constant is affected by the internal parameters of the semiconductor device, primarily the value of quenching resistance R_q, parallel stray capacitance C_q, junction capacitance of inner depletion region C_d, number of microcells N and load resistor R_l as described in the equation derived in [121]:

$$\tau \approx R_q(C_d + C_q) + NR_l(C_d||C_q) \tag{4.2}$$

Some SiPMs exhibit a fast component of the pulse as was shown in [122]. The fast component is related to the parallel stray capacitance C_q of the quenching resistor and load resistor R_l. The presence of a fast component significantly changes the shape of the pulse. Although there are several groups utilizing PSD techniques with

SiPMs and also several papers which examine the internal electrical properties of SiPMs and their influence on output pulse shape, there has been very little focus on understanding the effect of variables such as bandwidth of the front-end electronics and internal parameters of SiPMs on the performance of PSD algorithms. Since these properties significantly influence the pulse shape, it can be assumed that the PSD performance will depend on them. The optimization of PSD algorithms and selection of the optimal PSD algorithm for given parameters of bandwidth and SiPM parameters was investigated in [123] using a Monte Carlo model of scintillator/SiPM system called MC-SiPM. MC-SiPM allows to calculate and analyze the response of a scintillator/SiPM system to various types of ionizing radiation. The detector described in this chapter was not optimized for the best PSD performance mainly due to the frequent changes in its parameters during the development phase of the detector. This prevented the long term stabilization of the design and fixation of the analog circuitry and parameters needed for the optimization. These changes were done to meet the demands in the aviation radiation field such as to cover most of the deposited energy spectrum without saturation of the detector and linearity of the response.

4.1.2 Analog circuit design

The schematics of analog circuitry can be seen in Figure 4.5. The summed current pulse coming from MicroFC-60035 SiPMs is converted to voltage pulses and amplified in an inverting transimpedance amplifier (TIA). TIA uses an operational amplifier (OA) OPA656 [124] with bandwidth of 500 MHz which is sufficient for transfer of the main frequency component of the signal. Due to the addition of capacity of four SiPMs, the pulses have much longer rising edges. Therefore, there is not such high demand on the frequency bandwidth of the OA as if only one SiPM was used. Since the amplification circuit was designed for a single SiPM it is possible to use OA with lower frequency bandwidth (lower power consumption). The output voltage signal is then separated into two branches. Both branches are amplified by a non inverting voltage amplifier that uses AD8039 OA [125] and their impedance is adjusted so it matches the following circuitry. One branch is amplified with amplification of 2 (OUT1) and the second one with amplification of 11 (OUT2). In Figure 4.6 and Figure 4.7, the pulses from TIA and voltage amplifiers OUT1, OUT2 can be seen. The amplification added by voltage amplifiers decreases the frequency bandwidth of the system which explains why the OUT2 pulses last longer and have milder rising edges. This will negatively influence the PSD algorithm. On the other hand, a very fast rising edge of the pulses from TIA would require a digitizer with a very fast sampling frequency >250 MHz.

4.1.3 Bias voltage circuit design

A very important part of the detector is a circuitry that generates bias voltage for SiPMs. The output of SiPM is very sensitive to slight changes in the bias voltage therefore the aim is to have bias voltage as stable as possible without any ripple. The bias voltage circuitry is shown in Figure 4.8. The voltage of -30 V is generated

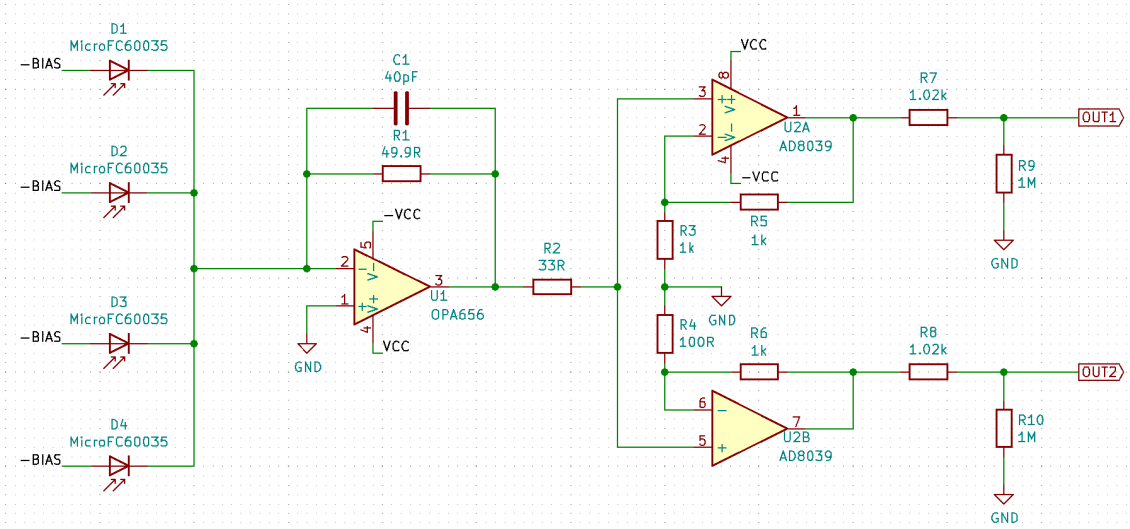

Figure 4.5: The schematics of analog circuitry - SiPMs, transimpedance amplifier and two voltage amplifiers.

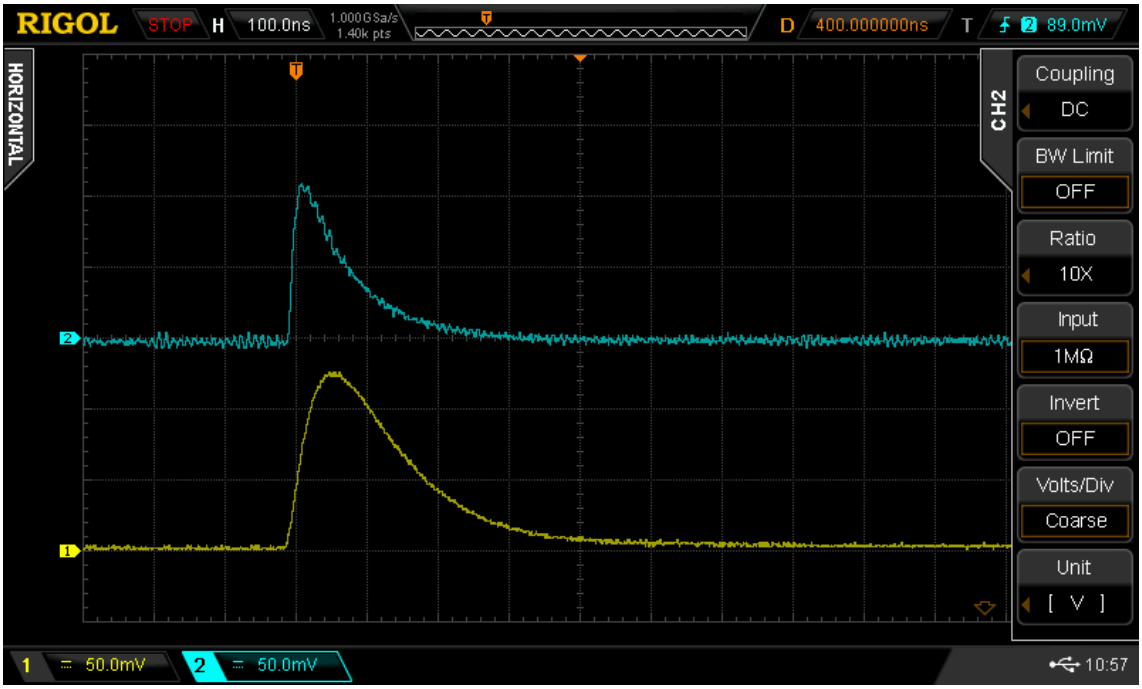

Figure 4.6: The blue signal shows pulse from TIA and yellow signal shows amplified pulse OUT1.

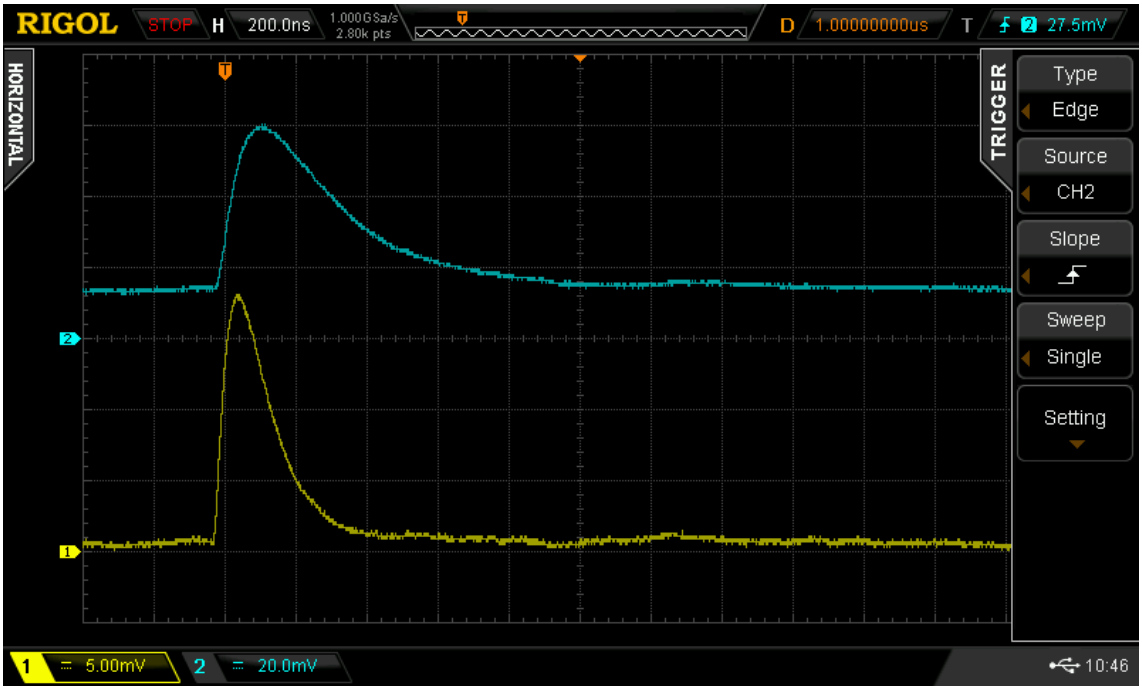

Figure 4.7: The yellow signal shows amplified pulse OUT1 and blue signal shows pulse from OUT2.

in the standard switching power supply module RB-3.315D [126] which has a high efficiency (80-90%) but its downside are the ripples with a fixed frequency on the output voltage (100 kHz). To filter the ripples, a linear low voltage dropout regulator (LDO) TPS7A3001 is used [127]. The used LDO is able to pass only a fraction of the ripples and makes the bias voltage stable. Each SiPM also uses passive RC filters. The voltage divider on feedback of LDO was set so it outputs -27 V which corresponds to overvoltage of approximately 2.45 V. The exact breakdown voltage is individual to each SiPM and is within the range of 24.2 V up to 24.7 V. The value of breakdown voltage depends on the temperature of the SiPM. The response of regulated bias voltage to a pulse is shown in Figure 4.9. It can be seen that the bias voltage in response to a sudden draw of current lowers the overvoltage by approximately 10 mV and it takes about 10 μs to fully recover from the drop. Such behavior is expected and mitigated by the use of large reservoir capacitors.

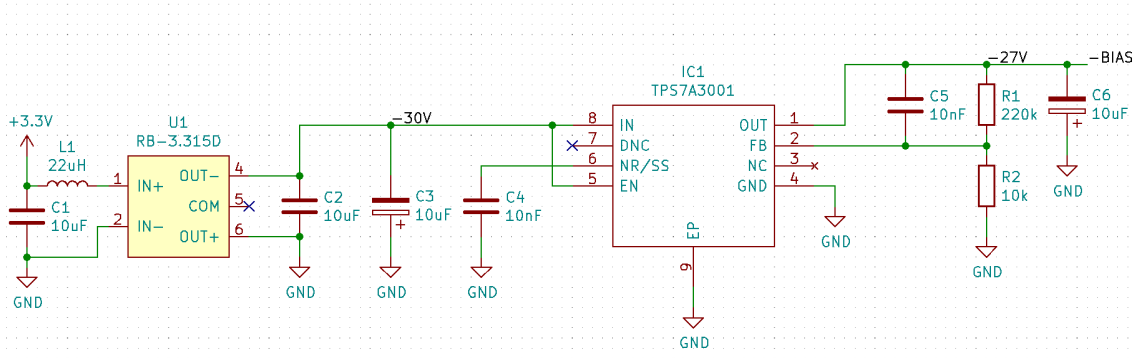

Figure 4.8: The bias voltage regulator circuit.

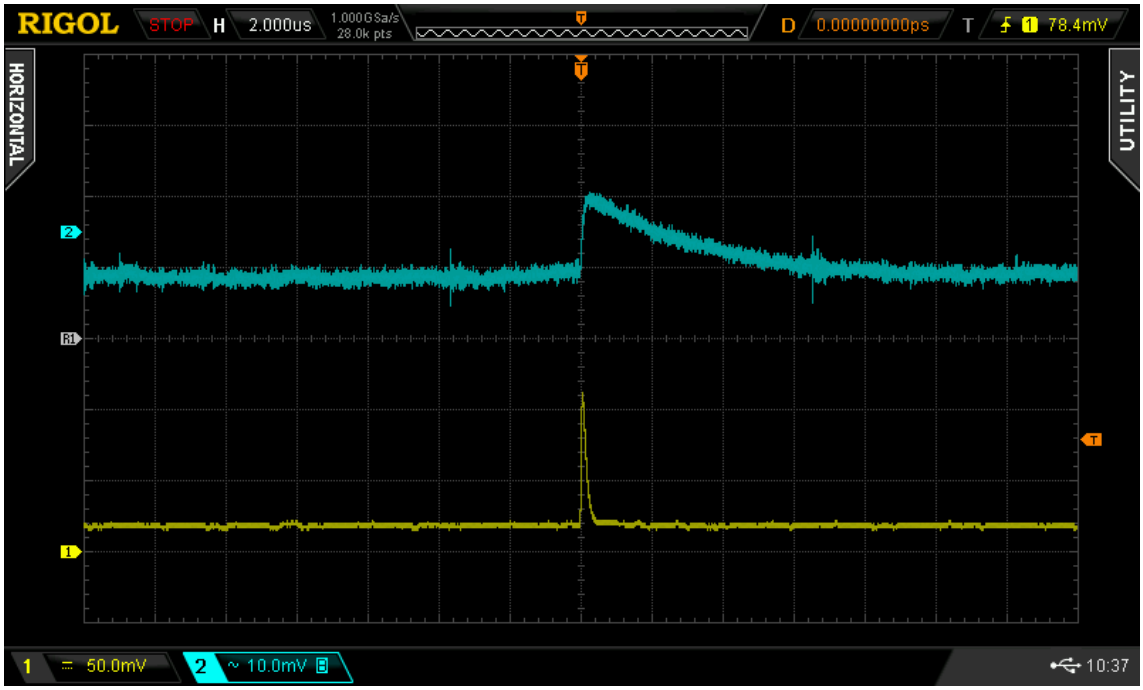

Figure 4.9: The response of regulated bias voltage to impuls produced by SiPMs. The yellow signal is the output voltage from analog channel OUT1 and the blue signal is AC coupled signal of bias voltage.

4.1.4 Digital circuit design

The data are processed by commercially available field programmable gate array (FPGA) platform Red Pitaya STEMlab 125-10 [128]. The Red Pitaya platform is shown in Figure 4.10. The Red Pitaya contains two analog to digital converters (ADC) with sampling frequency of 125 MHz and 10 bit resolution and 50 MHz analog bandwidth. Both channels can be adjusted to a voltage range of ± 20 V or ± 1 V. The settings of ± 1 V are used on both channels. One of the channels (CH1) digitizes analog pulses with amplification of 2 (OUT1) and the second channel (CH2) digitizes analog signals with amplification of 11 (OUT2). The ADCs output is processed by the FPGA. It uses Linux as an operating system. The hardware of the Red Pitaya platform such as ADCs, UART, I2C, etc. can be controlled by default commands that can be programmed in several programming languages. The system is loaded to the Red Pitaya via a micro secure digital card (SD card). The software that controls the function of the Red Pitaya was written in C programming language and was implemented in Linux operating system. The data taken by the detector are saved to the external USB disk. Signal processing that is done in FPGA is relatively simple. The output of CH2 is checked for triggers. The pulses are triggered if the value of signal exceeds 16 mV. If the pulse is triggered the buffers on both channels (CH1 and CH2) are filled and then saved to the file in human readable form to external USB disk. The buffers are filled in a way that 96 samples before the trigger are saved and each buffer has a size of 512 ADC samples. The analysis of raw pulses is done in post processing. The description of signal processing is summarized in Figure 4.11.

Together with the sampling of the ADCs additional data are saved to the USB

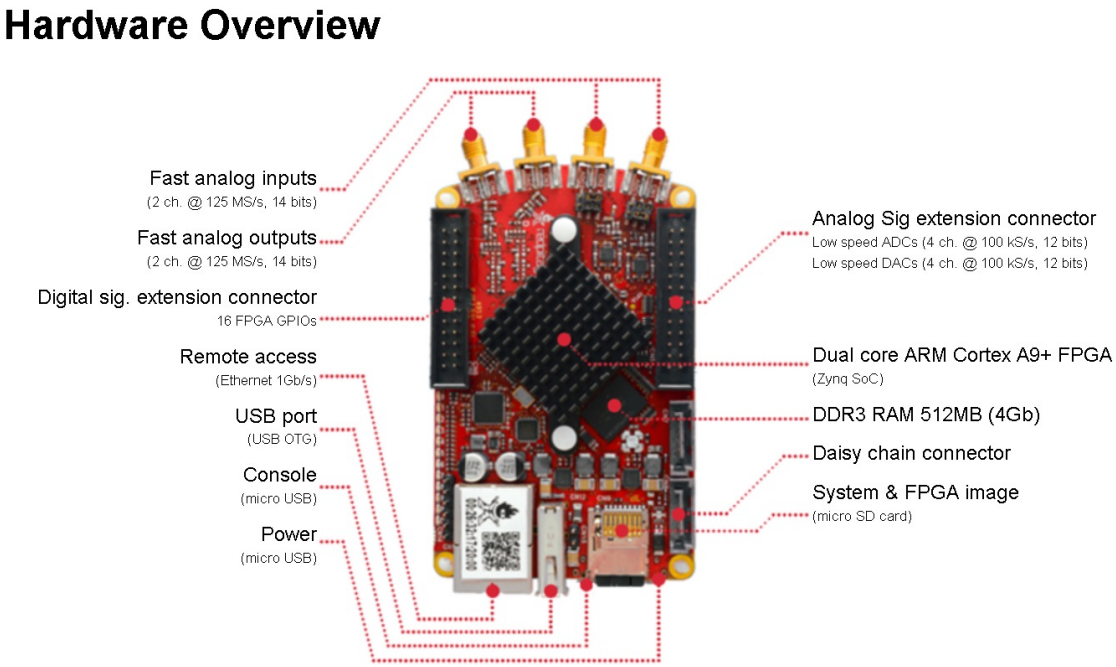

Figure 4.10: The photograph of the Red Pitaya platform.

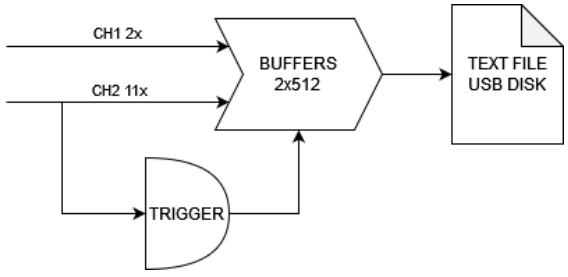

Figure 4.11: Schematic representation of data processing in Red Pitaya.

disk - temperature of the processing chip, GPS messages via UART if connected, time and date from RTC via I2C communication, and temperature of RTC chip via I2C. The RTC is located in close proximity to SiPMs. Therefore, the temperature of the RTC chip is used to evaluate the temperature of SiPMs.

4.2 Monte Carlo simulations in the aviation altitude

In order to simulate the response of a plastic scintillator in a neutron radiation field in aviation altitudes and to estimate the correction coefficients, the Monte Carlo calculation was performed. The simulation was performed similarly to the description in [92]. The plastic scintillator with size 1x1" was placed in a spherical neutron radiation source surrounding the scintillator. The radiation field was generated by the PARMA model [51, 52]. The simulation itself was carried out using the general purpose 3D MC particle transport simulation tool MCNP6 [129] which includes reaction models and cross-section data for simulation of reactions and transport of 37 different particle types. The primary neutron spectrum used in the MCNP6 simulation and generated by the PARMA model is shown in Figure 4.12. This spectrum corresponds to the environment with an altitude of 11.87 km, latitude of 50.42°, longitude of 15.8°, and date 29/11/2017 (the parameters of REFLECT flight described in [7]).

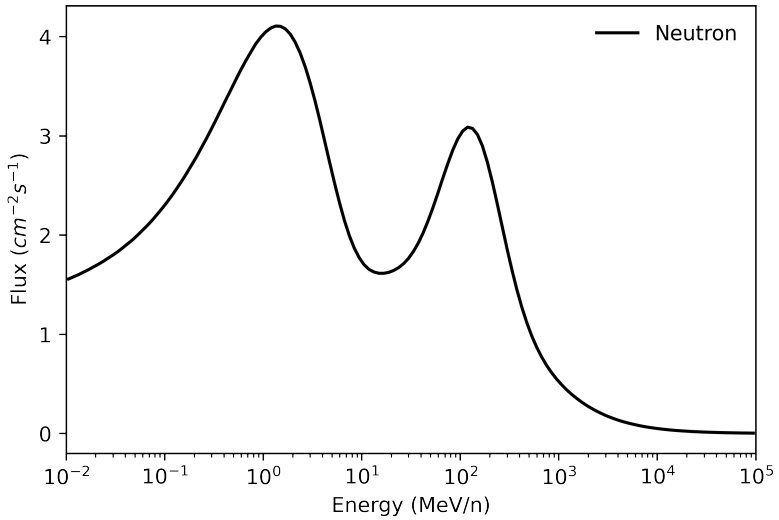

Figure 4.12: Primary neutron energy spectrum calculated by PARMA model.

The MCNP6 simulation used a tally to score deposited energy which was then recalculated to absorbed dose rate in given material. The contribution of individual energies to absorbed dose can be seen in Figure 4.13. The total absorbed dose rate from neutrons was calculated to 0.157 µSv/h. In order to calculate the fraction of absorbed dose that is not registered by the plastic scintillator based detector it is assumed that all of the absorbed dose is due to elastic scattering and the neutrons scatter uniformly. Therefore, each neutron can deposit energy from zero up to its maximum energy with the same probability. Figure 4.13 also shows the amount

of unregistered absorbed dose in the case that the detection threshold is 1.3 MeV for neutrons. In that case there is approximately 21% of absorbed dose that would not be registered. The corresponding correction factor $c_{thres.}$ that would adjust the measurements to 100% would be 1.266.

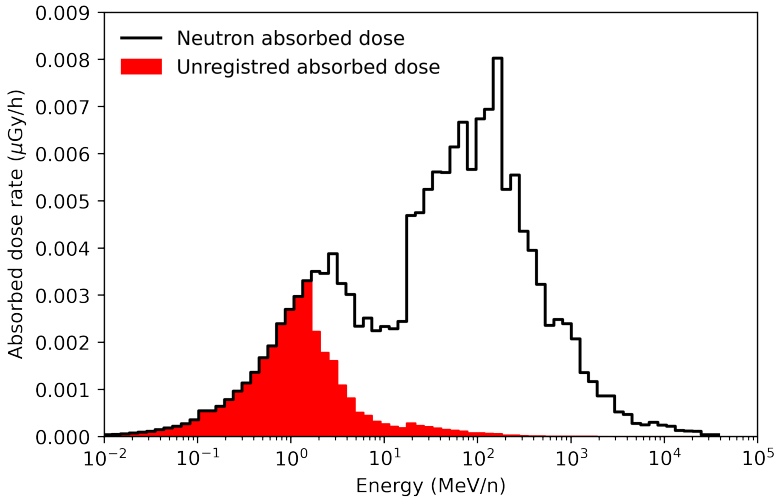

Figure 4.13: Result of Monte Carlo simulation showing absorbed dose rate as a function of neutron energy. The simulation was performed in a place and time of altitude 11.87 km, latitude 50.42°, longitude 15.8°, time 29/11/2017. The plot also shows an unregistered absorbed dose caused by a neutron detection threshold of 1.3 MeV.

In order to estimate the mean quality factor Q for neutrons, the results from publication [92] are used. It is shown that the absorbed dose rate in water is 0.23 µGy/h and the corresponding dose equivalent is 3.168 µSv/h. That results in a mean quality factor Q of 13.8. This factor is later used for conversion of absorbed dose to dose equivalent of plastic scintillator measurements. The calculations in [92] were performed in a thin slab of water with thickness of 0.3 mm and the recoil ions (mainly protons) were tracked by a fine mesh defined within the active volume and their LET was scored. The LET values were used to determine the quality factor of individual particles. This simulation was done for one specific place in the Earth's atmosphere therefore for general usage of this mean quality factor the neutron spectrum should not change as a function of the environment. In Figure 4.14, the normalized neutron energy spectra are shown. It can be seen that the normalized neutron energy spectra are very similar and nearly independent of influences such as altitude and latitude.

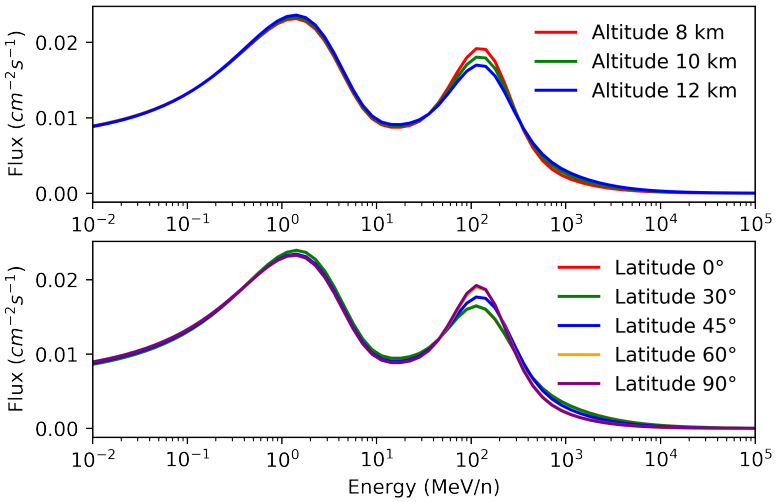

Figure 4.14: The comparison of normalized neutron spectra for different environments. The top plot shows a change of the neutron spectra for several altitudes and the bottom plot shows the change of neutron spectra for several latitudes.

4.3 Data processing, energy calibration and calculation of dose equivalent

4.3.1 Processing of the pulses

The raw analog pulses that are saved to the external USB disk are analyzed after the measurement in post processing. Such an approach allows to change and adjust the processing algorithms and troubleshoot the errors. The disadvantage is that saving the whole signal waveforms takes more time hence increases the dead time of the detector and it puts high demand on the size of the external USB disk as such a detector is able to produce a large volume of data within a short period of time. The schematic procedure of pulse processing is shown in Figure 4.15. The pulse processing is done as follows:

- Features of pulse are calculated namely the maximum value of ADC sample and wear-off which is calculated as the average of the last three ADC samples. These parameters are used for identification of pulses that lasted for so long that they are not fully digitized or for the identification of pile up pulses.
- The pulses are separated into two groups based on the amplification - low (OUT1) and high (OUT2) amplification. That is necessary because each amplification needs different parameters for its processing.
- The trigger position is determined from the settings of Red Pitaya software which allows to set the number of pretrigger samples which are saved before the trigger. Typically, the pretrigger is set to 64 samples.
- The trigger point is used to calculate the beginning of the pulse via a parameter of gate offset which determines how many samples or nanoseconds before

trigger point the pulse starts. The background is then removed by subtracting a baseline from the pulse. The baseline is calculated as an average of ADC samples before the beginning of the pulse. The number of samples used for baseline calculation can be controlled.

- The end of the pulse is calculated as a point where the decay of the signal reaches the value of baseline (zero after the subtraction of baseline from the pulse).
- Then the PSD parameter of the pulse is calculated based on the features of the pulse.
- At the end the integral of the pulse is calculated. It is used to determine the absorbed energy.

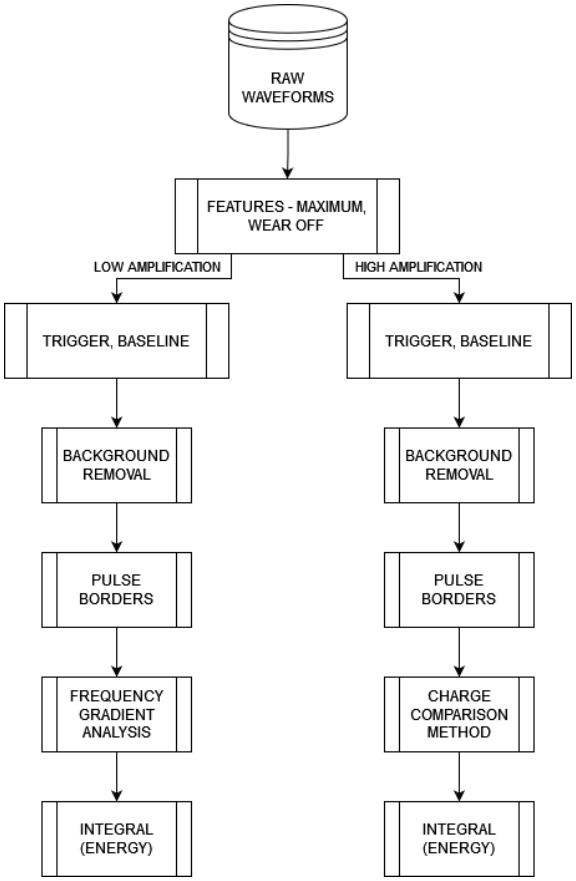

Figure 4.15: Pulse processing schematics.

4.3.2 Discrimination of low and high LET component

For the discrimination of low and high LET component several methods can be used. The methods are based on analysis of the pulse shapes and calculating a parameter that can be used to discriminate the individual components. As was explained and shown in the previous text the pulse shape is strongly influenced by the

frequency bandwidth of the system hence pulses from low gain analog signal path are different from pulses produced in high gain analog signal path. Therefore, two different methods are used. For low amplification the Frequency gradient analysis (FGA) is used and for high amplification the Charge comparison method (CCM) is used.
The CCM method is based on integration of two parts of the pulse - short gate and long gate. Typically, the short gate integrates only part of the pulse and the long gate integrates the whole pulse. The ratio between short gate and long gate integrations is used as a discrimination PSD parameter. The length of the short gate can be changed and optimized for the best performance.
The FGA method is based on comparison of different frequencies within the pulse. The pulse is transformed to frequency domain by Fourier transform and the ratio between two different amplitudes from the spectrum is used as PSD discrimination parameter. Typically, the amplitudes of the first element of Fast Fourier Transformation (FFT) and amplitude of the n-th element of FFT are used. The method can be optimized by selecting the n-th element. This method was introduced in [130]. The FFT spectrum of photon and neutron pulses are shown in Figure 4.16.

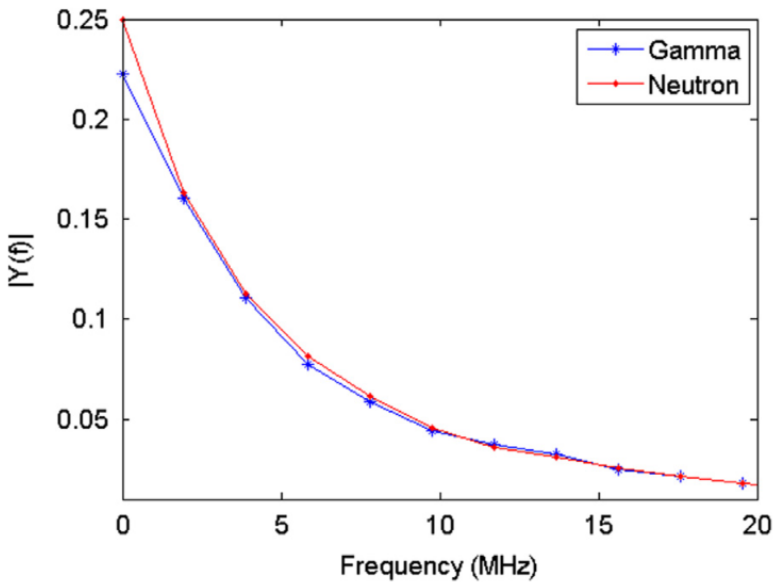

Figure 4.16: The FFT spectrum of photon and neutron pulses [130].

Usually, the discrimination of neutron and photon components is done for AmBe source but it produces neutrons with maximum energy of approximately 12 MeV. Since the contribution of neutrons exceeding 12 MeV at flight altitudes is significant, the discrimination algorithms must be tested for higher energies. Therefore, the testing of PSD methods was performed on data obtained from an experiment at Heavy Ion Medical Accelerator in Chiba (HIMAC) where a thin beam of carbon ions with energy of 430 MeV/n collided with a plastic target. The detector was placed at a degree of 45° from the target. The interactions of silicon ions with molecules of the target creates among other high energy neutrons that can be detected. The setup of the experiment can be seen in Figure 4.17.

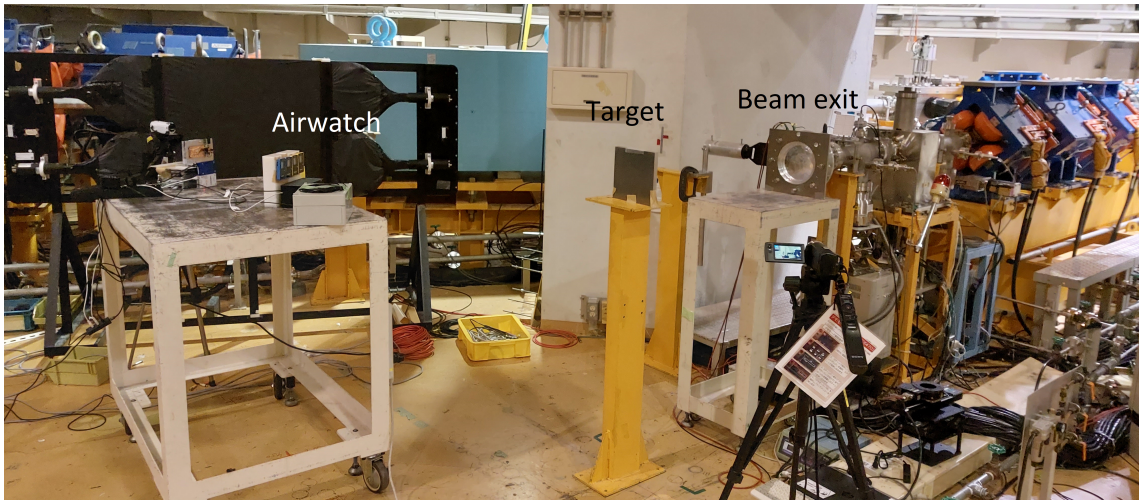

Figure 4.17: A photograph of the C 430 MeV/n setup experiment at HIMAC.

The PSD is performed on uncalibrated data using arbitrary units (corresponds to the integrals of the pulses). The 2D histogram of PSD parameters as a function of energy for both amplifications can be seen in Figure 4.18.

The 2D histogram was sliced into a series of 1D histograms for different energies. The 1D histograms were fitted by Gaussian Mixture Model (GMM) described by equation:

$$f(x) = A_1 * exp(-(x-\mu_1)^2/(2\sigma_1^2)) + A_2 * exp(-(x-\mu_2)^2/(2\sigma_2^2)) \tag{4.3}$$

Where A is the amplitude of Gaussian function, μ is the location of the maximum and σ is the standard deviation of the Gaussian function. The separation point was calculated as the intersection of both Gaussian curves. The example of the GMM fitting is shown in Figure 4.19. The separation line was calculated as a linear interpolation of the individual separation points. The separation line for both amplifications is shown in Figure 4.20. The optimization parameter of CCM (length of the short gate) was chosen to 25 samples and optimization parameter of FGA (frequency) was chosen to 1.22 MHz. Due to the low number of detected neutrons during the experiment the fitting of GMM suffered large errors and inconsistency. Therefore the optimization of the parameters was not possible. The parameter values of PSD algorithms were determined only by trial and error method.

4.3.3 Low LET component energy calibration and temperature correction

The energy calibration of the photon component is straightforward and was described in [131]. The proposed method uses gamma ray Compton edges of common radionuclides such as ^{22}Na, ^{60}Co, and ^{137}Cs. The exact location of the Compton edge is determined by a differential method described in [132]. The method uses the differential of histogram. The theoretical position of Compton edge can be calculated by equation:

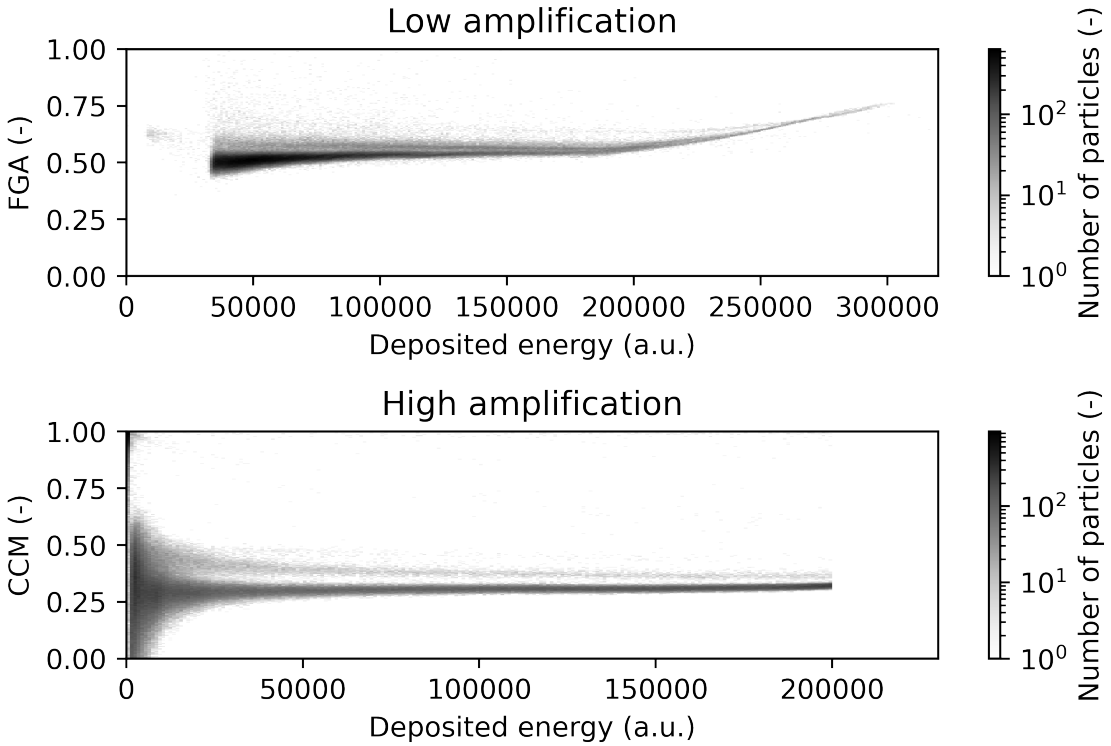

Figure 4.18: The top and bottom plots show 2D histogram of PSD parameters as a function of energy for both amplifications. The data were obtained from an experiment at HIMAC experiment with a C ion beam with energy of 430 MeV/n.

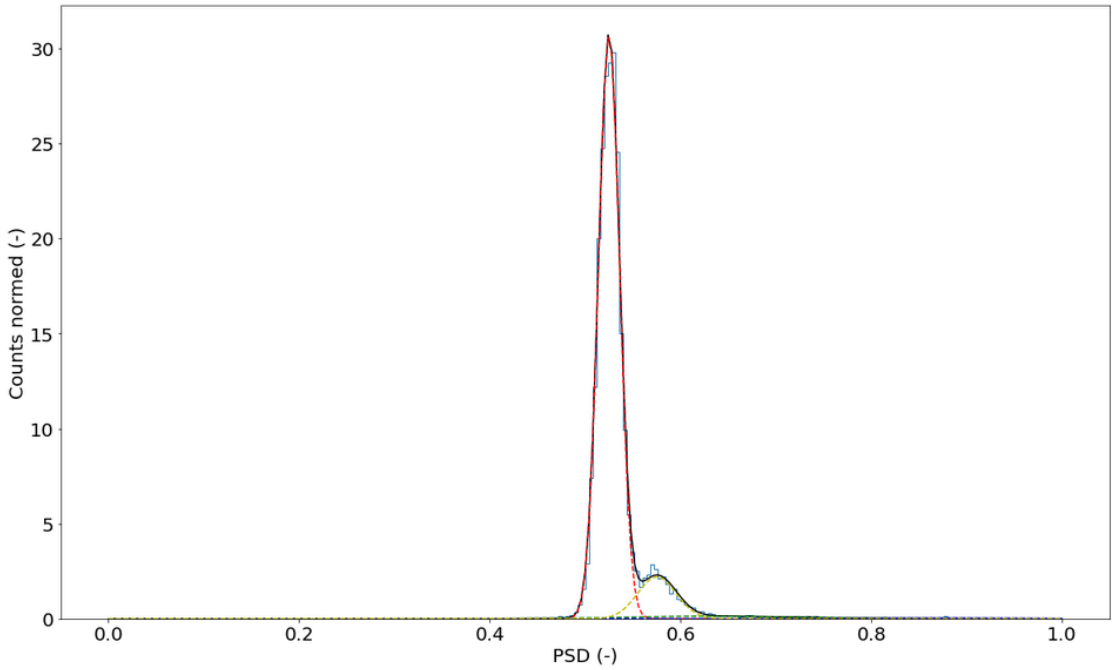

Figure 4.19: The example of Gaussian mixture model fitting.

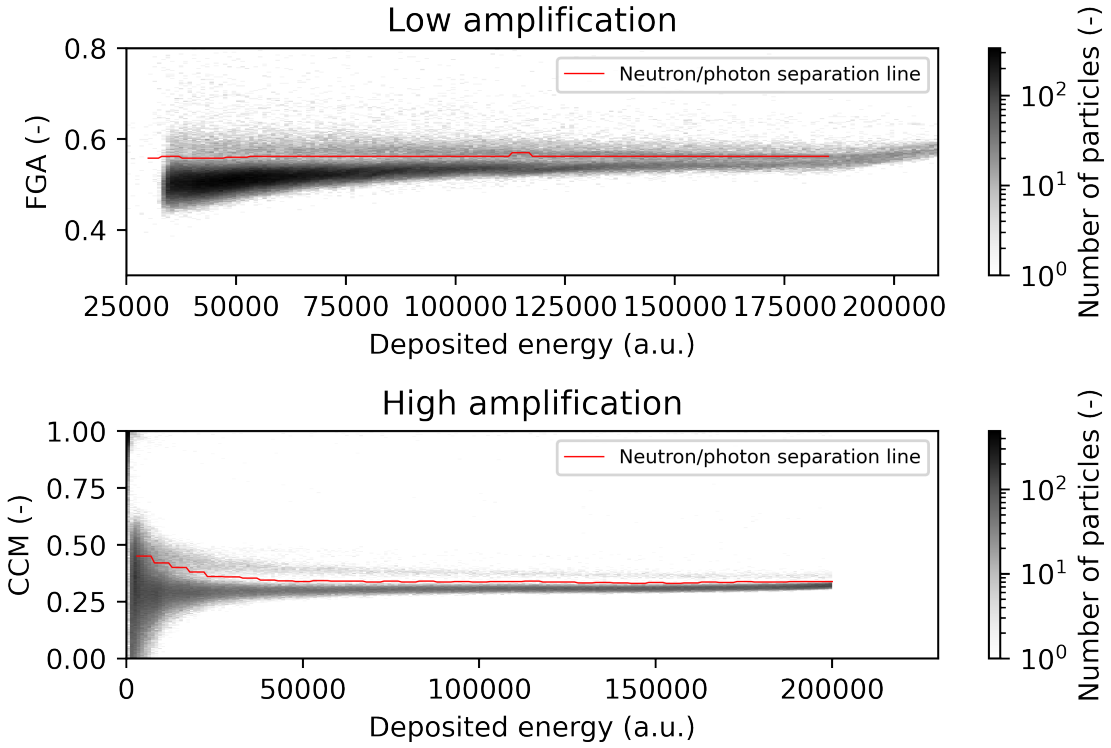

Figure 4.20: The top and bottom plots show 2D histogram of PSD parameters as a function of energy for both amplifications from carbon beam 430 MeV/n. The separation lines which were constructed based on the GMM fitting are shown.

$$E_{Compton} = \frac{2E^2}{m_e c^2 + 2E} \tag{4.4}$$

Where E is photon energy and $m_e c^2$ is electron mass energy of 511 keV. The photon energy of used radionuclides and their Compton edges is tabulated in Table 4.3.

Table 4.3: The list of common gamma ray sources, their energy and corresponding Compton edges.

Gamma ray source	Energy (keV)	Compton edge (keV)
^{22}Na	511	339
^{22}Na	1275	1061
^{137}Cs	662	447
^{60}Co	1253	1040

The used calibration model is described by equation:

$$y = ax \tag{4.5}$$

Where x is the channel, y is the deposited energy and a is the fitted model coefficient. Both amplification channels were calibrated individually. The calibration curves can be seen in Figure 4.21.

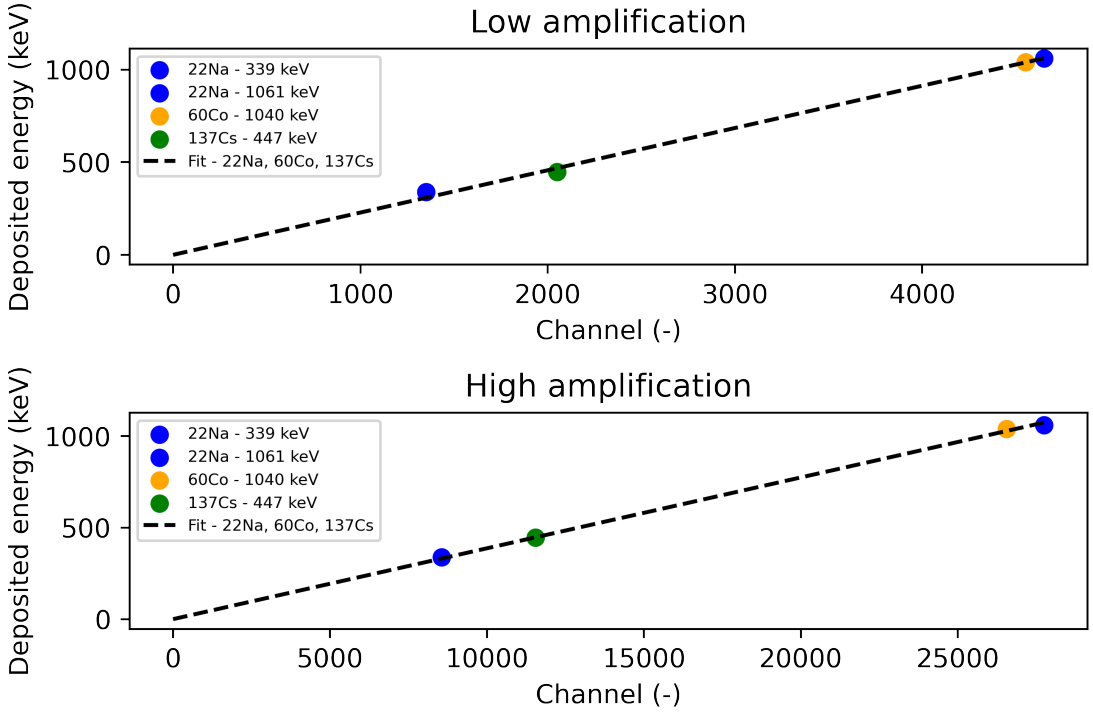

Figure 4.21: The illustration of calibration curves for both amplification channels performed on radionuclide ^{137}Cs, ^{22}Na and ^{60}Co.

Due to the use of fixed bias voltage and temperature dependence of SiPM breakdown voltage the response of the detector changes significantly with temperature. This change can be seen by comparing the response shown in Figure 4.22.

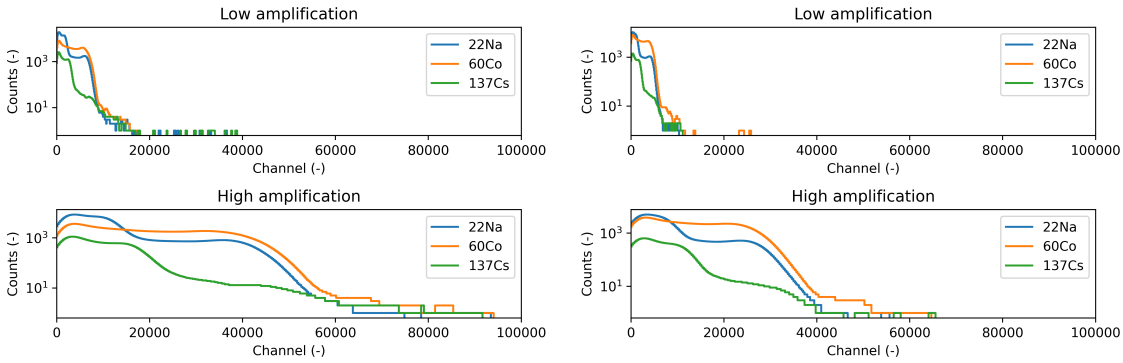

Figure 4.22: The response of the detector to various gamma sources at different temperatures. The first row shows a low amplification channel and the second row shows a high amplification channel. The first column is a response for a temperature of approximately 4°C (irradiation performed in the fridge) and the second column shows response for a room temperature of 25°C.

In order to compensate for the change in the response of the detector due to changing temperatures the calibration coefficient a described in Equation (4.2) is adjusted according to the following equation:

$$a = \alpha T + \beta \tag{4.6}$$

Where α and β are fit coefficients and T is temperature. The coefficients α and β were determined by linear regression of data for two temperatures (4°C and 25°C). The temperature near SiPMs is measured every 10 seconds.

4.3.4 High LET component energy calibration

The energy calibration that is used for the photon component cannot be used for the neutron component due to the effect of energy quenching. The energy quenching causes lower light yield of particles with higher LET. It has been described in organic and inorganic scintillators as well [133, 134, 135, 136]. The mathematical model that allows recalculation of the photon energy calibration into neutron energy calibration was described in [137]. The mathematical model is described by equation:

$$y = ax - (b * (1 - exp(-cx))) \tag{4.7}$$

Where x is recoil proton energy, y is electron energy, and a, b, c are fitting parameters. This method was used for example in [138, 139]. The fitting parameters a, b, c in [139] were calculated for 2x2" scintillator EJ-276. The same parameters were used for 1x1" scintillator EJ-276 used in the detector. The used parameters are shown in Table 4.4. The translation of fitting parameters was verified by irradiation at the

D+T generator which produces neutrons with energy of 14.1 MeV. The experiment at the D+T generator was performed at Technical University of Ostrava.

Table 4.4: The neutron calibration parameters used for 1x1" EJ-276 scintillators.

Fitting parameter	EJ-276 1x1"
a	0.75
b	3.2
c	0.22

The use of fitting parameters should result in maximum measured neutron energy of 14.1 MeV. In Figure 4.23, the neutron edges are shown at 14.8 MeV. This is a 5% difference compared to the energy of 14.1 MeV. Although the translation of fitting parameters worsens the neutron energy resolution and precision it is sufficient for the application. The parameters could be improved if the detector was irradiated at a D+D generator which produces neutrons with energy of 2.45 MeV. Then the parameters could be refitted to agree with the two neutron edges.

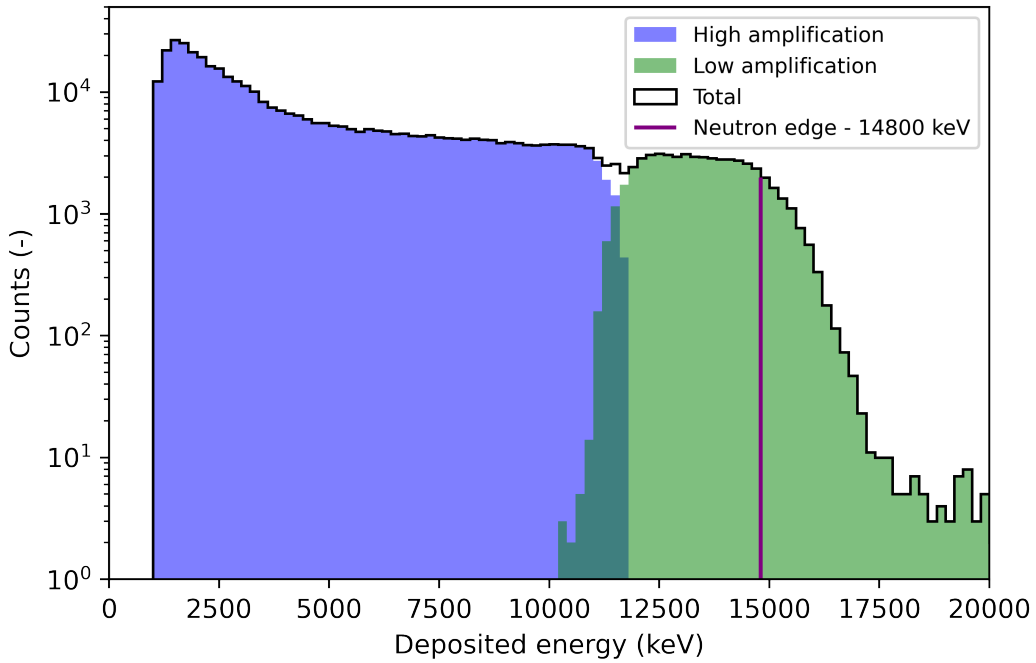

Figure 4.23: The localization of 14.1 MeV neutron edge for EJ-276 scintillator on D+T neutron generator.

4.4 Results onboard aircraft

After the characterization of the detector, it was deployed on the testing flights onboard aircraft. The detector was implemented in a box with two other detectors

namely semiconductor based detector AIRDOS and detector with NaI(Tl) scintillator. The whole assembly is called Airwatch and it can be seen in Figure 4.24. Airwatch is powered from the electrical socket.

Figure 4.24: A photograph of the Airwatch system that is used for the measurements onboard aircraft. The Airwatch contains a detector based on plastic scintillator, Si based detector AIRDOS and NaI(Tl) scintillator.

Results from two flights will be introduced. The first flight was from Narita airport (NRT) in Tokyo to Istanbul airport (IST) in Istanbul and the second flight was from Istanbul airport (IST) to Vaclav Havel airport (PRG) in Prague. The route of both flights can be seen in Figure 4.25 and Figure 4.26.

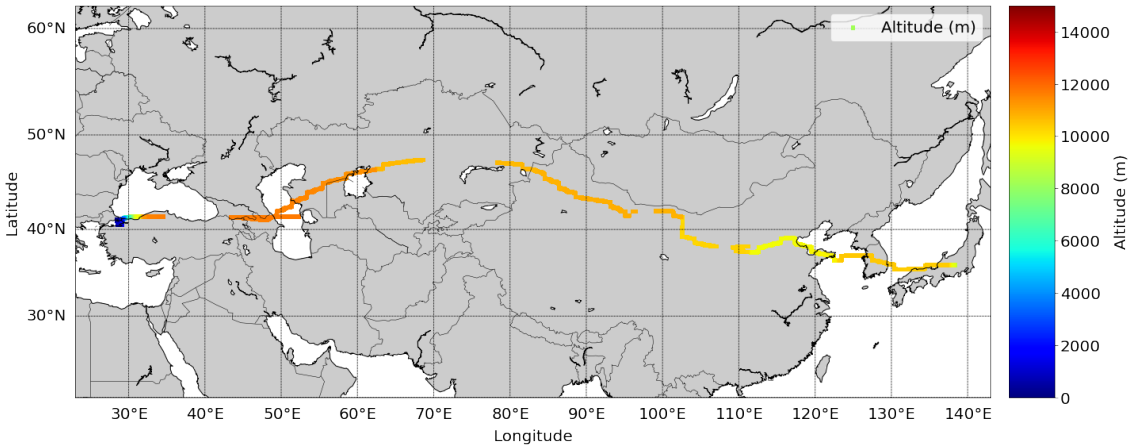

Figure 4.25: The route of the airplane from Narita Airport to Istanbul International Airport.

The detector was deployed on regular airlines and was plugged into the electrical socket provided for each passenger onboard. The detector measured continuously except for a couple of short interruptions. The flight profile of cosmic ionizing radiation in terms of absorbed dose is shown in Figure 4.27 for NRT-IST flight and in Figure 4.28 for IST-PRG flight. The absorbed dose is shown for low and high LET components (distinguished by photon/neutron separation line). The low LET component is plotted alongside the output of CARI-7 software which shows the ambient dose

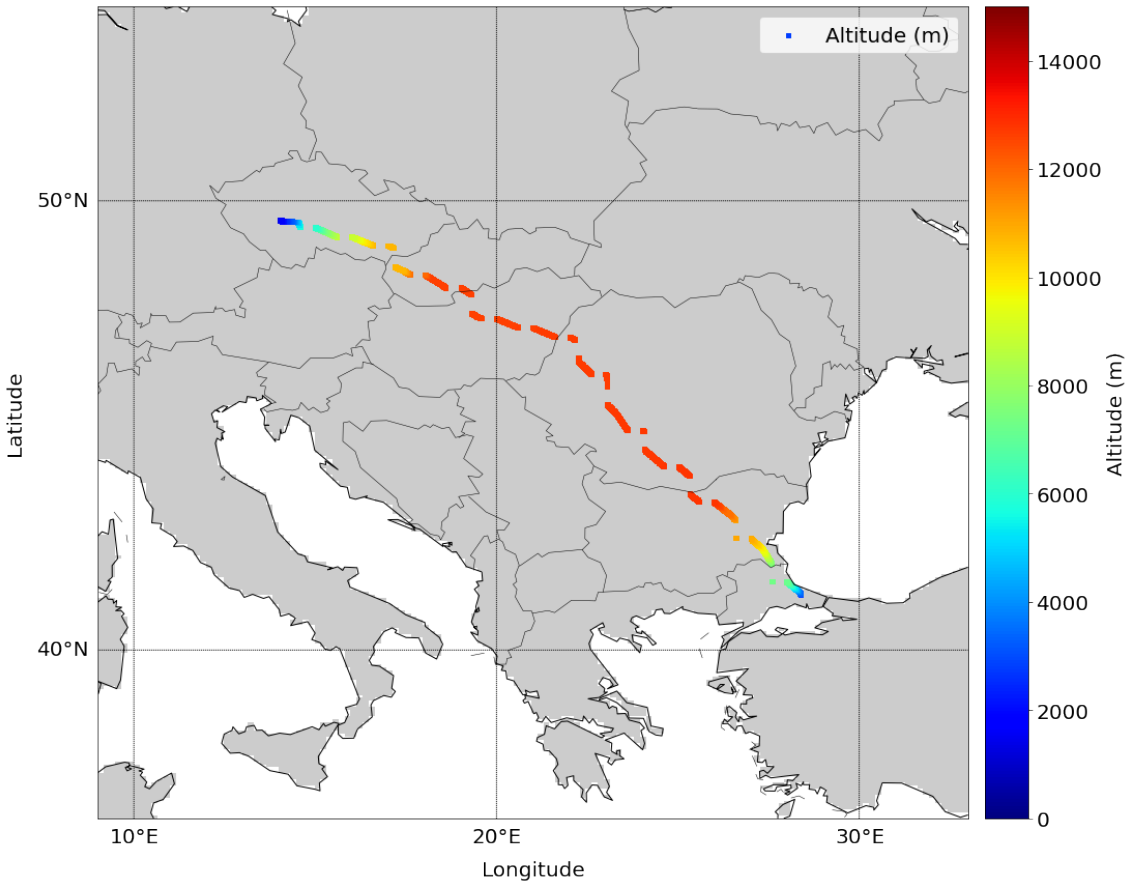

Figure 4.26: The route of the airplane from Istanbul airport to Vaclav Havel airport.

equivalent. It can be seen that the measurement of absorbed dose of low LET component reflects the changes in ambient dose equivalent calculated by CARI-7. This is especially visible in the results from NRT-IST flight. The small sudden changes are caused mainly by changes in flight levels whereas continuous changes are caused particularly by transition in latitude. Although there is a high correlation between measured low LET absorbed dose and calculated ambient dose equivalent the rate at which they change is different. Hence, both lines do not overlay perfectly. That is presumably caused by the increasing contribution of neutrons in such a region. It can be seen in particular at IST-PRG flight where the lines widened as the aircraft traveled to the higher latitude. On the other hand this widening is reflected in the high LET component (mostly neutrons) - slow increase of high LET absorbed dose in higher latitudes. Due to the low cross section of neutron interaction with plastic scintillator the number of detected neutrons is much lower than low LET particles therefore the neutron component has higher variability. This partially confirms that the basic concept of the plastic based detector works and that it can be used to a certain extent for aviation dosimetry without the need for correction factors that are based on the location of the aircraft.

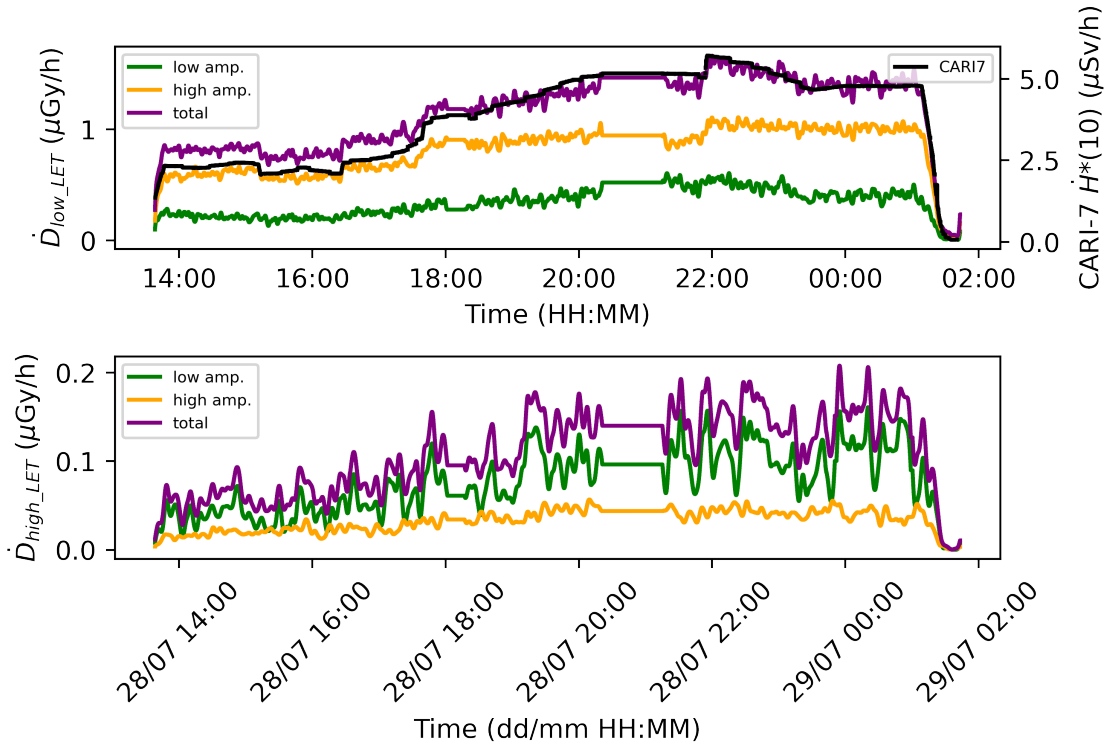

Figure 4.27: The flight profile of NRT - IST flight. The top plot shows the absorbed dose rate of low LET component including individual amplifications and its comparison with the CARI-7 results. The bottom plot shows the absorbed dose rate of high LET component including individual amplifications.

The calculation of dose equivalent was done according to the following equation:

$$H = D_{lowLET} + D_{highLET} * \overline{Q} * c_{thres.} \tag{4.8}$$

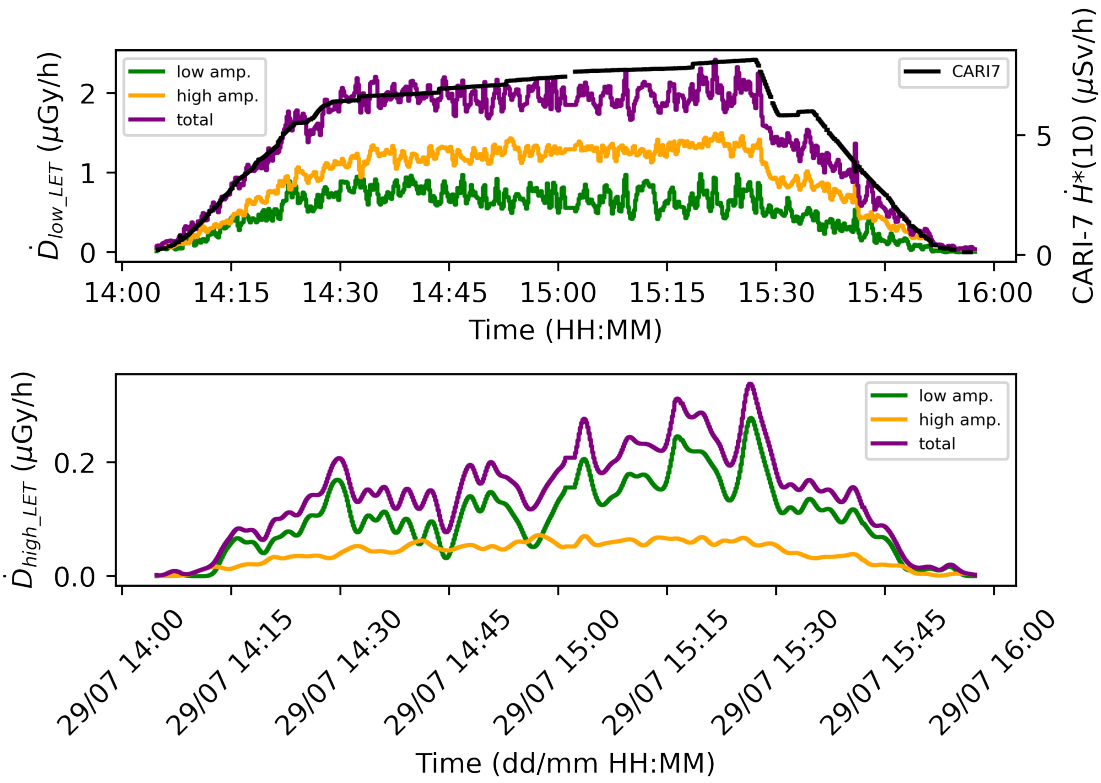

Figure 4.28: The flight profile of IST - PRG flight. The top plot shows the absorbed dose rate of low LET component including individual amplifications and its comparison with the CARI-7 results. The bottom plot shows the absorbed dose rate of high LET component including individual amplifications.

Where coefficient Q is coefficient of the mean quality factor of the neutrons and $c_{thres.}$ is a coefficient that corrects for neutrons that were not detected due to the detection threshold. The calculation of those coefficients were discussed in section 4.2. The comparison of dose equivalent with ambient dose equivalent calculated by CARI-7 software is shown in Figure 4.29 for NRT-IST flight and Figure 4.30 for IST-PRG flight. Since CARI-7 can also calculate contributions of individual particle types, the neutron contribution is compared to measurements of the high LET component. It can be seen that the total dose equivalent is underestimated compared to the CARI-7 results and the high LET dose equivalent is in agreement with the neutron ambient dose equivalent determined by CARI-7. This would suggest that the main error comes from the underestimation of low LET component. In order to verify this assumption the low LET component is compared with data from Si detector AIRDOS. This comparison of NRT-IST flight is shown in Figure 4.31. The native data measured in Si were recalculated to absorbed dose in water. It can be clearly seen that the absorbed dose rate in water measured by Si detector shows much higher values than plastic based detector. It is possible that this error is caused by energy quenching. Whereas the neutron deposited energy is adjusted for this effect by using an exponential model described in Equation (4.7) the low LET component is assumed to behave the same as photons (without any quenching). This assumption might not be fulfilled because in the complex mixed radiation field in the aviation altitudes the scintillator is irradiated by many different types of particles which might undergo energy quenching and still be considered as low LET such as muons, electrons, positrons, etc. In order to overcome this problem the absorbed dose measured by Si detector can be used to evaluate the low LET component. The absorbed dose measured by Si diode was shown to have a quality factor Q of 1.06 in [92] hence it can be used to evaluate the dose equivalent of low LET component. The summation of dose equivalent measured by Si detector and high LET component measured by plastic based detector is shown and compared with CARI-7 in Figure 4.32. It can be seen that there is a good agreement between the measured data and software calculated results. The total dose equivalent received during the NRT-IST flight was calculated to 45.00 µSv by CARI-7 and 46.26 µSv by combined measurement of Si detector and detector based on plastic scintillator. The relative error between those two values is nearly 3% which is an excellent agreement. Moreover this result was achieved without using any coefficients that would be based on the location of the airplane hence inherently suggesting the quality of the radiation field.

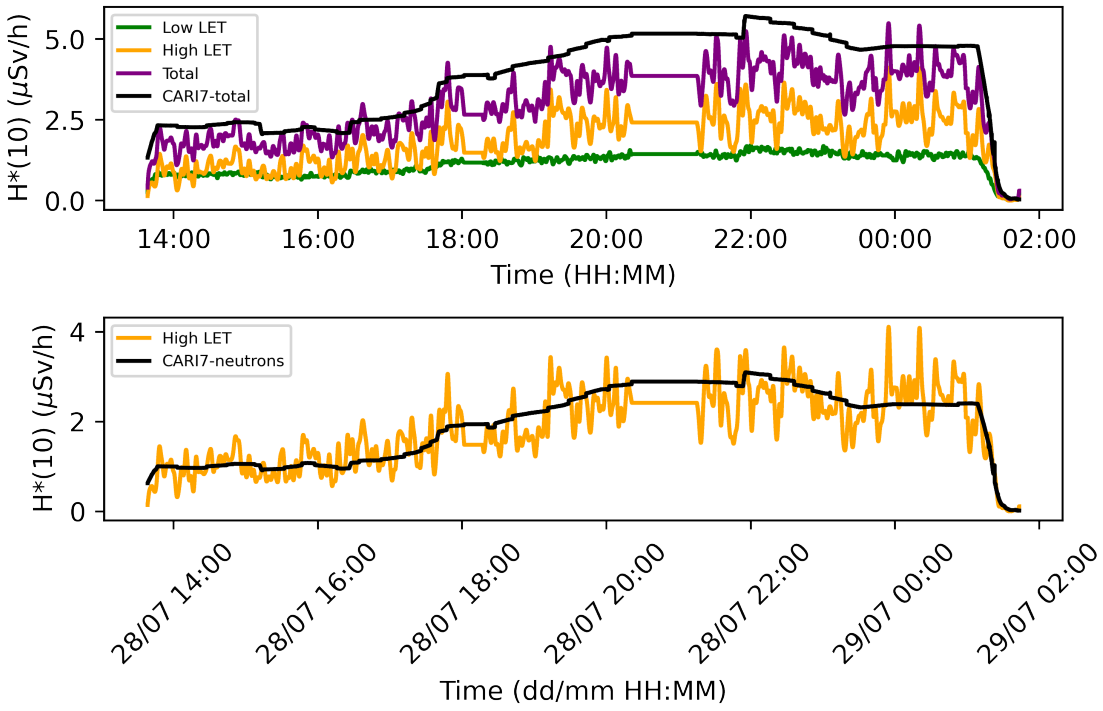

Figure 4.29: The flight profile of NRT - IST flight. The top plot shows the dose equivalent rate of low LET component including individual amplifications and its comparison with the CARI-7 results. The bottom plot shows the dose equivalent rate of high LET component and its comparison with the neutron ambient dose equivalent rate calculated by CARI-7.

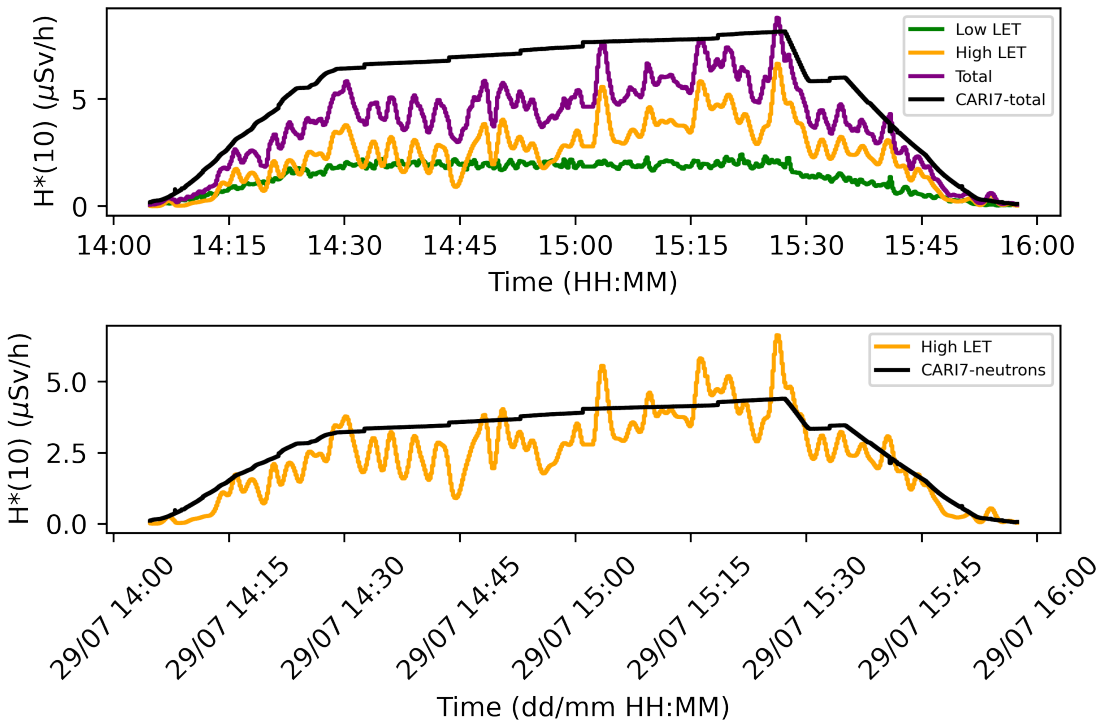

Figure 4.30: The flight profile of IST - PRG flight. The top plot shows the dose equivalent rate of low LET component including individual amplifications and its comparison with the CARI-7 results. The bottom plot shows the dose equivalent rate of high LET component and its comparison with the neutron ambient dose equivalent rate calculated by CARI-7.

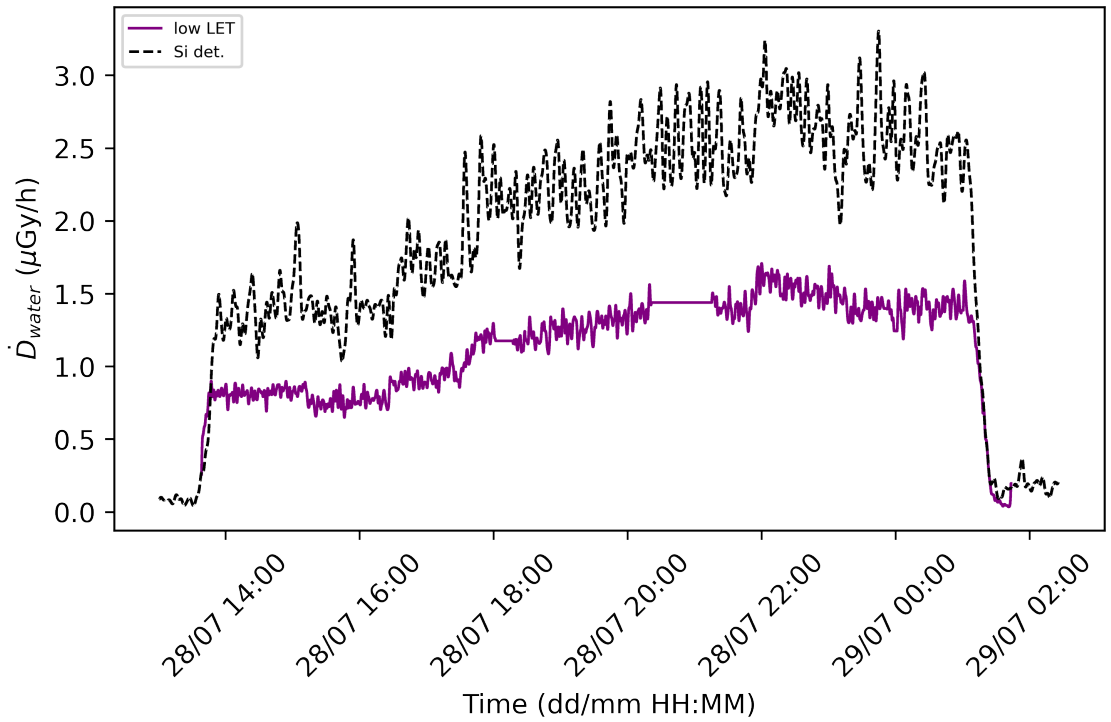

Figure 4.31: The comparison of absorbed dose rate in water measured by detector based on plastic scintillator and Si based detector AIRDOS.

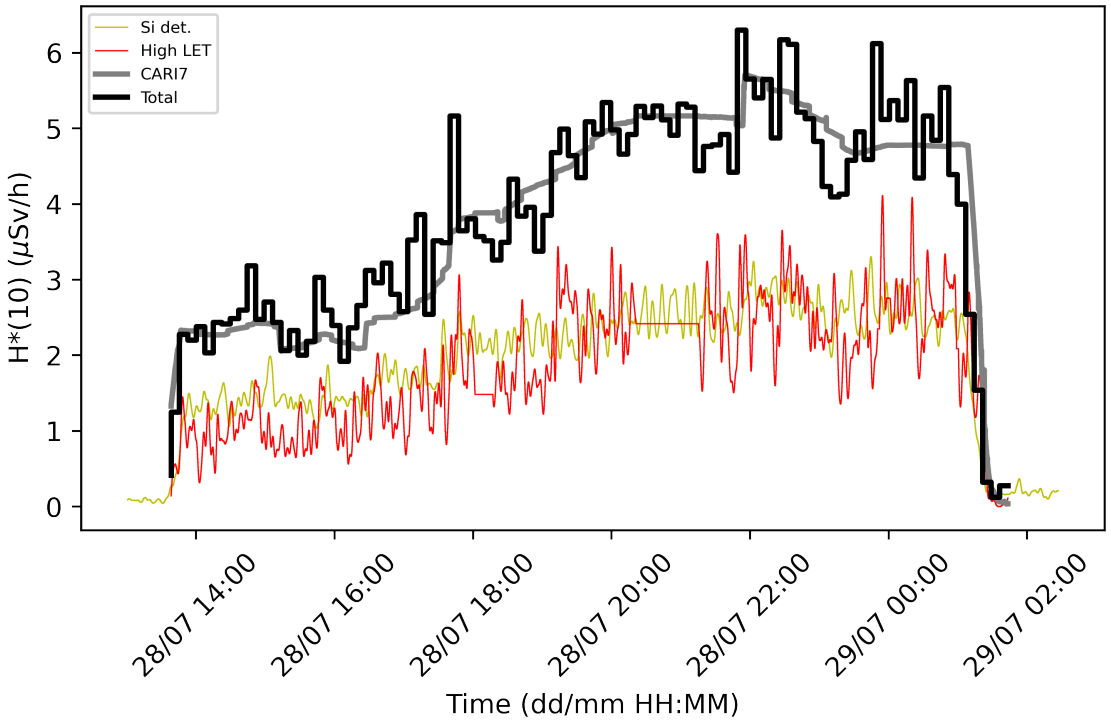

Figure 4.32: The flight profile of NRT - IST flight. The plot shows the dose equivalent rate calculated by a method combining results from a detector based on plastic scintillator and Si based detector AIRDOS and ambient dose equivalent calculated by CARI-7.

4.5 Remarks

A new detector based on a plastic scintillator was designed. Its main purpose is to measure the radiation doses onboard aircraft with the purpose to verify the algorithms used for calculation of radiation doses to aircrews, and to monitor the space weather and its manifestation to the radiation field in Earth's atmosphere. For space weather monitoring, complex detectors that can measure different particle types are more suitable because the changes in the radiation field in the atmosphere might be significant only in increase of neutrons for example. Therefore, frequently used Si detectors might not be ideal for such research as they are not sensitive to all particle types and they need to be corrected for the quality of the radiation field.
After extensive characterization and calibration of the new detector, it was tested onboard aircraft. The data show very good agreement in terms of dose equivalent of the high LET component with CARI-7 but significant underestimation of dose equivalent of the low LET component. Therefore, a method combining data from two detectors was proposed. The data from Si detector are used to evaluate dose equivalent of the low LET component whereas the detector based on plastic scintillator is used to evaluate the high LET component. The combined data show an excellent agreement with CARI-7. The relative error between the CARI-7 and measurement is lower than 30% as recommended by [6]. Hence, it can be assumed that the introduced method and detector can be successfully used in the aviation dosimetry. Further research and development is needed to verify the accuracy and to make the system more reliable and more deployable. In the future, more flights will be analyzed and evaluated to generate a robust set of data that can be used for statistical analysis of the system accuracy and precision. The future development will involve improvements in detector design mainly to decrease power consumption. The final goal is to design the whole detection system (plastic scintillator and Si diode) in a way that it can be powered by USB with maximum power consumption of 2.5 W. Then it could be powered by onboard USB chargers which are very common in civil aircrafts so the detection system would be easily deployable by passengers. One way to achieve this goal is to optimize the internal digital circuit design of FPGA and optimization of the analog circuitry. Another possibility of improving the design of the detector is by using stilbene instead of EJ-276 scintillator. The advantages of the stilbene are better PSD capability and lower threshold for discrimination of neutrons (appx. 500 keV of deposited energy by neutrons). Regarding the improvements in the characterization of the detector there is a series of things that could be improved. The first one is the photon calibration of the plastic scintillator. It was shown that the calibration was done on Compton edge which has a maximum energy of 1061 keV but the particles measured in the aircraft frequently deposit energies in the range of several MeVs. The calibration is therefore heavily extrapolated. In the high energy region many effects can become important such as the parasitic effects of SiPM (afterpulsing, crosstalk), and operational amplifiers could modify their response as their slew rate (maximum voltage change per time of an amplifier) is not infinite etc. The improvement could be done by experiment at AmBe source which produces photons with energy of 4.438 MeV with Compton edge of 4.198 MeV. The second improvement can be done by optimizing the parameters of PSD preferably by neutrons with a large range of energies (up to tens of MeV) such as the neutron

radiation field created by irradiation at HIMAC. Unfortunately, longer irradiation was needed to collect enough data for the optimization. The PSD can be also optimized by tuning the bandwidth of the system as was shown in [123] and it would need to be verified by a series of measurements at a neutron radiation beam such as AmBe.

Although there are many improvements that can be done the concept of the detection system was proven and the obtained results are promising. The detectors based on tissue-equivalent scintillators could become a complement to the already existing network of semiconductor based detectors which are commonly used for the verification of the aviation dosimetry algorithms. The advantage of such systems is that it can be constructed cheaply and it is relatively small compared to standard TEPC detectors.

Chapter 5

High-energy atmospheric phenomena in thunderstorms

The high-energy phenomena occurring in thunderstorms are a relatively new scientific field. However, the idea of high-energy particle production due to the thunderstorm electricity was firstly proposed in [140] in 1925. Since then this idea was extended and updated based on new scientific evidence. Today, it is generally accepted that thunderstorms can work as a large particle accelerator that is created between two oppositely charged layers. The main driving process of the ionizing radiation production is the relativistic runaway electron avalanche (RREA) [141, 142, 143, 144, 145] and modification of electron energy spectra (MOS) [146]. The seed electron for the RREA is produced by cosmic radiation or radioactive decay [143]. If the seed electron has sufficient energy to overcome the energy losses due to ionization it can be accelerated by the electric field within the thunderstorm while creating new electrons which undergo a similar cycle, hence avalanche effect. It is assumed that the RREA can occur with positive feedback caused by scattered photons and positrons. The photons can be scattered into the location of the beginning of the avalanche and positrons can move backward in the avalanche and create new seed electrons at the beginning of the avalanche. The electrons in the avalanche can be accelerated up to several tens of MeV. The MOS process is caused by acceleration of high-energy electrons produced in the air by cosmic rays when the electric field inside the thundercloud is not strong enough to cause the RREA.
The accelerated electrons undergo ionization losses in the air but can be slowed down while producing bremsstrahlung - high-energy gamma rays. The bremsstrahlung has a much higher range in the air than electrons and is often detected at high-mountain observatories or at the coast of Japan sea where the thunderstorms have cloud bases near the sea level. This phenomenon is often called Terrestrial Gamma Ray Enhancement (TGE) or prolong burst [14, 147, 148, 149, 150, 151, 152, 15, 153]. The TGE events last from seconds up to tens of minutes. It is often accompanied by increase in radon progenies as the rain washes the radon product down from the air. The increases in detection of gamma rays, X-rays, electrons and neutrons have been reported during TGE. In recent years, two TGE events measured in the Czech Republic were reported [154, 155].
Although the research of TGE is very extensive and many papers have been pub-

lished on this topic, it will not be covered in this work since the detector proposed in Chapter 6 is intended only for measurement of neutrons generated by Terrestrial Gamma Ray Flashes (TGFs). Therefore, the following text will focus only on TGF.

5.1 Terrestrial Gamma Ray Flashes

The TGF is a rare phenomenon associated with lightning during which extremely intensive bursts of radiation are emitted within milliseconds [156, 157, 158]. Up to today thousands of TGFs by satellites, airplanes, and on ground (so called downward TGF) have been detected.

5.1.1 Measurement of TGF from low Earth orbit

The first TGF was reported in [9] by a satellite that was intended to measure gamma ray bursts from distant galaxies. Surprisingly, they observed gamma rays from Earth. The detected events were correlated with regions with strong lightning activity. Since then thousands of TGFs have been measured by satellites. Mostly by Reuven Ramaty High Energy Solar Spectroscopic Imager (RHESSI) [10], Astro-rivelatore Gamma a Immagini Leggero (AGILE) [159, 160, 161], Gamma-ray Burst Monitor (GBM) [162, 163], and Atmosphere-Space Interactions Monitor (ASIM) [164]. The energy spectrum of gamma rays spreads up to tens of MeVs and the estimated brightness of a typical TGF is approximately 10^{18} accelerated electrons. It was shown that a portion of the events measured in space were in fact the electrons that reached the satellite detectors and not only the bremsstrahlung photons [165]. The catalogs of TGFs show no relationship between location, season and energy, time duration of TGFs. Nevertheless, there is a strong dependence of TGF occurrence on latitude. Majority of satellite TGF measurements are within a 20 degree region from the equator. It was proposed in [166] that this dependence is caused mainly by the atmospheric absorption of gamma rays due to elevated tropopause in the equatorial regions.

5.1.2 Measurement of TGF in airplanes

Altogether two TGFs were detected onboard aircraft. The first measurement was published in [11]. A complex detection system, called Airborne Detector for Energetic Lightning Emission (ADELE), was used. The ADELE system was specifically designed to measure in wide dynamic range and large fluxes. The observation of TGF was performed in Florida, USA. The TGF was observed 11 ms after the positive intra cloud lighting that occurred in the active thunderstorm approximately 12 km away from the plane. The second measurement was performed by an improved ADELE system in the eye of hurricane Patricia [167]. Interestingly, the authors assumed that the increased count rate on ADELE was caused by positrons that are inherently accelerated in opposite directions as electrons in the RREA. The flux of positrons is expected to be fainter. The TGF was associated with positive intra cloud lightning.

Although the TGF has never been detected onboard a commercial aircraft, there are concerns about the radiation safety of passengers and aircrews. The radiation doses for various cases were calculated in [16, 17]. It was shown that in the worst case scenario the radiation doses can reach significant values up to 1 Sv. Fortunately, this scenario assumes that the aircraft is hit by the accelerated electrons and bremsstrahlung. The radius of the accelerated electron beam is relatively small compared to the gamma rays. Therefore, it is much more likely that the plane is hit only by a portion of the gamma rays. That would increase the radiation doses as well but the radiation risks would be much lower.

5.1.3 Measurement of TGF on ground

The first reported ground measurement of TGF is in [12]. The measurement reported on 227 individual gamma rays arriving within a 300 μs period and associated with lightning. The observed photons reached very high energies (approximately 10 MeV). The measurement was done at the International Center for Lightning Research and Testing in Florida (ICLRT), USA. Another two TGF observations from Florida, USA were published in [168, 169]. Both publications observed high energy photons exceeding 10 MeV within a short period of time associated with lightning. A very complex measurement of TGF from Florida was published in [170]. The TGF associated with lightning was measured by high-speed cameras, a lightning mapping array and a network of gamma ray detectors. Data suggest that the TGF occurred during positive upward lightning and was caused by RREA. A research published in [171] shows one registered TGF in Japan that paralyzed the gamma ray detectors. This work discusses the origin of TGFs and the type of lightning which is responsible for creation of TGF. It was proposed that at least a subset of TGFs is generated by initial breakdown pulses (IBP) of negative lightning. Three TGF observations were published in [172]. They were measured by Telescope Array Surface Detector (TASD) in Utah, USA. The TGFs were composed of 2-5 individual bursts of gamma rays each with time duration $<$10 µs and separated by a few hundred microseconds. Similar observation was done in [13] who observed a TGF that consisted of 4 individual bursts with time duration of $<$1 ms and were separated by 0.7-1.5 ms. It was stated that it was a downward heading TGF with similar brightness as the regular upward TGFs measured by satellites. Interesting observation was brought by [13] who reported TGE above the Japan coast that was abruptly ended. The finish of TGE coincided with TGF. The authors stated that it cannot be decided what took place first if it was TGE termination or TGF because both events were overlapping. Another insight into TGF origin was brought by [173] who reported TGF at TASD site during the initial breakdown pulses of negative cloud to ground lightning and intra cloud lightning. The authors suggest that the IBP consists of a type of discharge called fast negative breakdown [174]. These breakdowns enhance the electric field up to 50% which causes production of electron avalanche within the discharge. These electrons then undergo RREA and produce TGF bursts. This suggests no need for relativistic feedback in generation of TGFs (or at least subset of TGFs) proposed in [143]. The latest publication focusing on measurement of TGF is [175]. It shows supporting evidence for the generation of TGF bursts from IBP. This

measurement also shows the first high-speed camera observation of TGF illustrating a rapid increase in luminosity during IBP (peak current up to 150 kA).
Although all previously mentioned observations of TGF measured the gamma ray, another way to study the presence of TGFs was shown in [176, 177, 178]. The publications proved the relationship between the TGF measured by satellite and energetic in-cloud pulses (EIPs) which are energetic IBP [173]. The EIP emits a radio signal which can be observed on ground.

5.2 Detection of neutrons from thunderstorms

5.2.1 Historical measurements

The first observation of neutrons correlated with thunderstorms, namely lightning was done in [179] in 1985. 11200 electromagnetic pulses (EMPs) were analyzed and correlated with the number of detected neutrons in BF_3 proportional counters. For 11068 EMPs only one or two neutrons within 320 μs after the EMP trigger was observed. Such cases were associated with cosmic radiation. When 3 or more neutrons were detected it was associated with EMP since there was very low probability that cosmic radiation would produce 3 neutrons within 320 μs. There were 124 events of EMP when counters detected 3 or more neutrons. It was suggested that the neutrons are generated by nuclear fusion of ^{2}H(^{2}H,n)^{3}He reaction which generates neutrons with energy of 2.45 MeV. Similar results with the same method were published in [180].
The short term measurement of neutrons correlated to the thunderstorm was published in [181] in 2010. It was measured in Brazil at 610 meters above sea level by a 70 cm^3 ^{3}He proportional counter. The event took less than 2 minutes and a strong flux of neutrons was observed (690 counts per minute). The neutron enhancement was attributed to the lightning and it can be seen in Figure 5.1.

5.2.2 Origin of thunderstorm neutrons

Later the neutron observations from the high-mountain observatory at Aragats were reported in [14, 182]. The strongest event was reported in [14] where strong enhancement on ArNM (neutron monitor 18 m^2) of 5.1 sigma was shown. The event took several minutes. The enhancement was also seen on ASNT (neutron telescope 4 m^2) [183] and SEVAN (0.25 m^2) [184, 185] with 63 sigma and 23 sigma. The reported results are shown in Figure 5.2. The neutron production was attributed to the photonuclear reaction of gamma rays with the air molecules.

The results presented in [14] were soon contradicted in [186] with proof that neutron enhancement detected by neutron monitors could have been caused by the photonuclear reactions of high energy gamma rays with lead shielding. This effect could artificially increase the background and lead to misidentification of thunderstorm neutrons. This suggestion was confirmed in [187] based on the Monte Carlo simulations. It was mentioned that smaller enhancement on ArNM could have not been influenced by lead shielding due to insufficient flux of high energy gamma

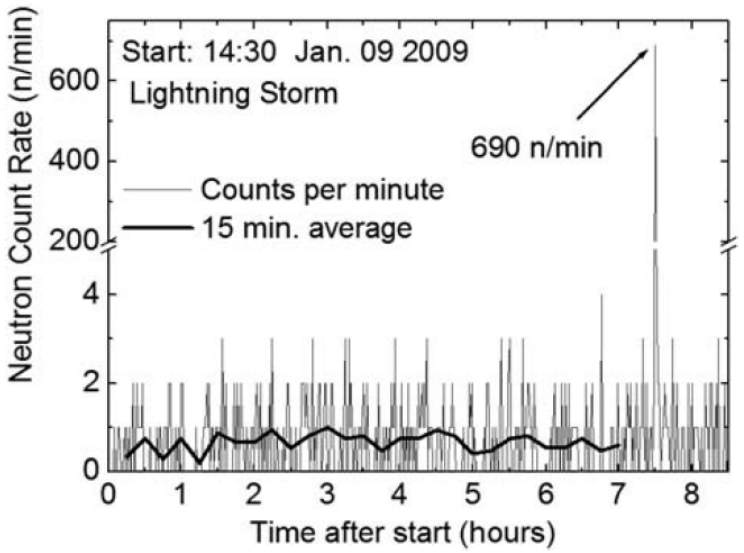

Figure 5.1: The neutron enhancement measured in [181] by ^{3}He proportional counter. The enhancement exceeded the natural background by several hundred times and took approximately 2 minutes (data were taken per minute).

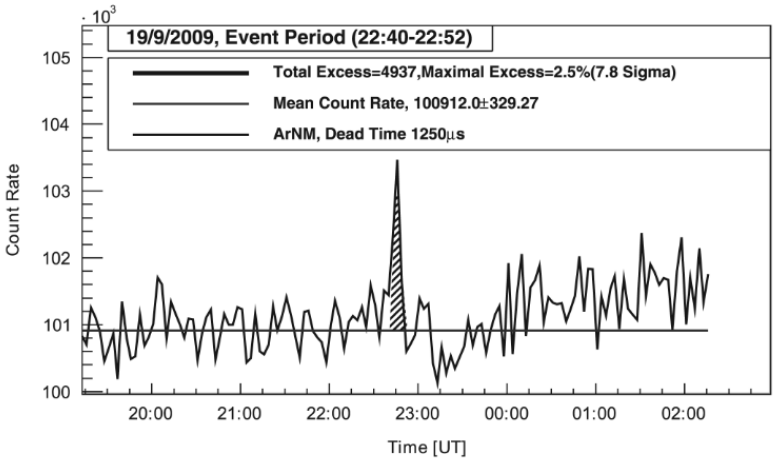

Figure 5.2: The neutron enhancement measured in [14] by ArNM. The increase was about 2.5% above the natural background and took approximately 12 minutes.

rays. It was theorized that the neutron enhancement can be seen on ArNM in cases where the thunderstorm is not directly above ArNM but rather off the zenith several hundred meters. One of the results of the simulations was that lateral spread of neutrons is larger (around 400 m) than lateral spread of gamma rays which are generated by bremsstrahlung in cones. Hence the gamma rays cannot contribute to ArNM enhancement only neutrons can. Other measurements done by NM were reported in [188]. The neutrons were observed near the sea level 1-3 km below the thunderstorm with NM. Measured flux was $4 * 10^{-3}$ neutrons per cm^2 per second which is approximately 40 times higher than flux reported in [14].
Other observations come from Kazakhstan from a high-mountain observatory at altitude 3340 meters above sea level [189, 190, 191]. In [189] extraordinary high fluence of low-energy neutrons are shown to be correlated with lightning discharges. Neutrons were detected by NM and ^{3}He counters which are sensitive to neutrons with energy up to 1 eV. Measurements were done with several counters under the roof, outside and in the underfloor. There are two conclusions being drawn from this paper. The first one is that neutrons are generated in the soil below detectors based on the ratios of different counters. The second one is that extraordinarily high flux cannot be explained only by photonuclear reactions itself. There must be some additional mechanism for production of neutrons. Reported flux was $3 - 5 * 10^{-2}$ neutrons per cm^2 per second.
The measurements of [189] were improved in paper [190]. Data from both detectors were available every 160 μs so a very fine time distribution of neutrons could have been measured. The results show that thermal neutrons and fast neutrons arrive approximately 0.4 ms and 0.08 ms after EMP, respectively. It can be clearly seen that neutron flux correlates with lightning discharge and neutrons arrive in short bursts with duration of 200-400 μs.
In [191] the measurements were improved by a 5 inches NaI(Tl) detector for measuring the gamma radiation ionizing detector and several Gaiger-Müller tubes that measured charged particles with very little sensitivity to neutral particles. It was reported that nearly each lighting corresponded to the increase in ionizing radiation detection. The data from all used detectors can be seen in Figure 5.3. These extraordinary results were soon questioned in [150]. It was shown that the electromagnetic interference (EMI) coming from lightning affects the electronics of the detectors and causes false pulses. The EMI pulses generated by lightning were bipolar whereas the typical pulses caused by ionizing radiation are unipolar. This effect was demonstrated on NM, plastic scintillator detector, and NaI(Tl) detector. Therefore, it can be assumed that most of the previously mentioned observations of neutrons were in fact measurements of EMI. Later the report of short neutron increase was reported in [153]. The increase was measured on NM and SEVAN detectors at the same second. It was stated that the signal was likely caused by EMI but it was speculated that it could be photonuclear reactions from TGF.

5.2.3 Thunderstorm neutrons from photonuclear reactions

Another measurement that is likely not affected by EMI was reported in [192]. The authors used a PANDA detector [193] based on plastic scintillators with gadolinium

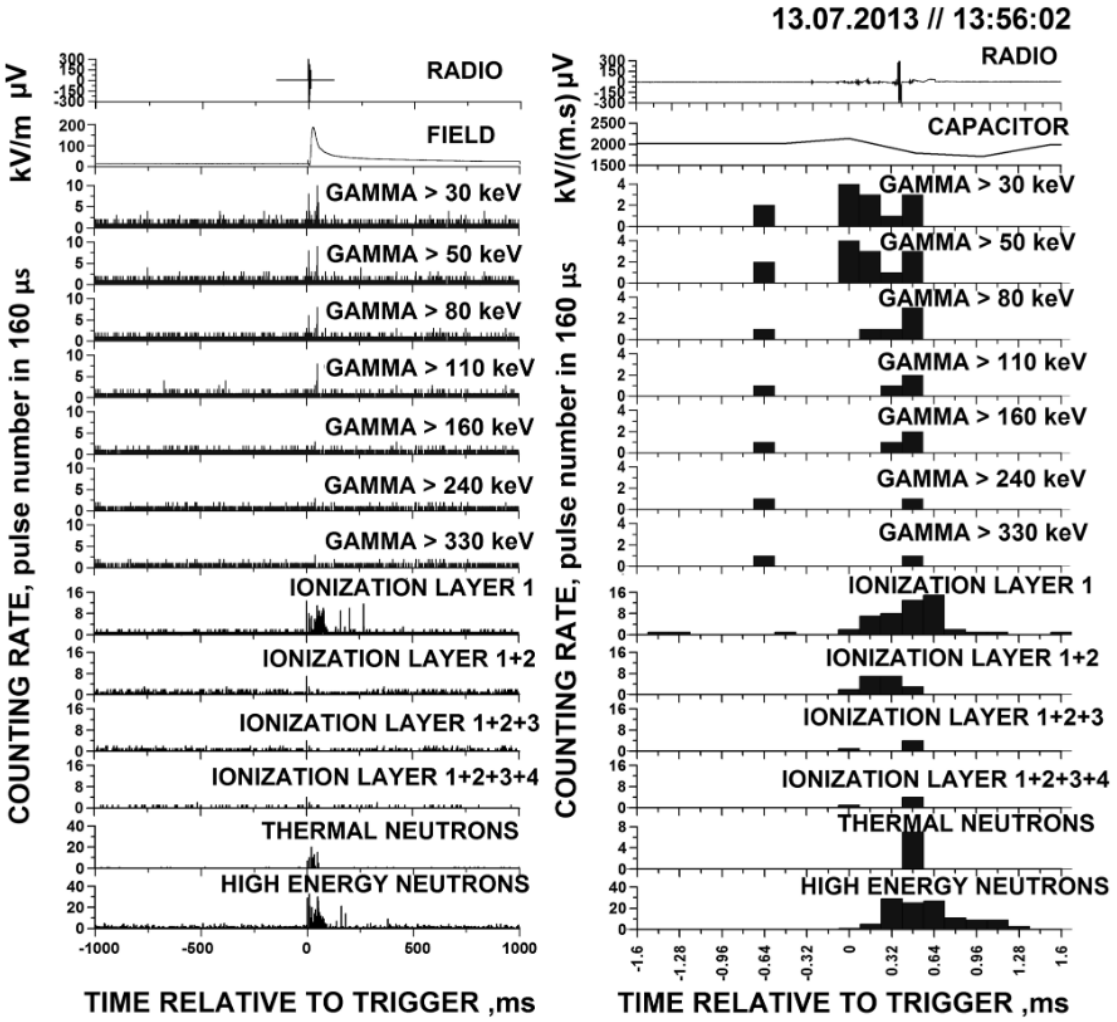

Figure 5.3: A complex measurement of ionizing radiation after lightning hit published in [191]. The results suggest that a large variety of ionizing radiation is generated by lightning as nearly all detector types registered an increase.

coated mylar film. The neutron detection is based on characteristic gamma radiation energy (8.5 MeV) which is generated from reaction of thermal neutrons with gadolinium. Such gamma rays are delayed by several tens of μs after the neutron loses most of its energy due to elastic scattering in the plastic scintillators. PANDA observed 3 gamma ray bursts in winter thunderstorms in Japan. Due to the angular distribution of Compton scattering there is an estimation of direction from which the radiation entered the detector. All events were at the zenith (right above the detector). All 3 events took tens of seconds and caused high enhancement in count rate. The increase in neutron detection took place during the last TGE event. Due to the nature of the neutron detection it is unlikely that this neutron enhancement was caused by a strong electromagnetic field caused by lightning.

There are a couple of papers from recent years that observed neutrons correlated with TGF which was always accompanied by lightning. One such measurement was reported in [194]. The authors used a combination of 2 plastic scintillators (BC-408, 1 inch and 5 inches) and NaI(Tl) (5 inches) called GODOT (The Gamma ray Observations During Overhead Thunderstorms) to observe neutron burst produced by TGF. The TGF happened when lightning hit the wind turbine located approximately 200 meters from detectors. After the plastic detectors recovered from the initial burst of neutrons and photons they measured a clear Compton edge of 2.223 MeV gamma rays which is produced by ^{1}H(n,γ)^{1}H reaction. This measurement was compared with simulations confirming that the radiation source was located approximately 1 km away from the detector. The data from NaI(Tl) scintillator were not shown due to technical issues (calibration issues in intense fields). The estimated flux of neutrons during this event was 10^3 neutrons per cm^2 per second and the burst lasted for approximately 100 ms. The results suggest that it was caused by downward propagated TGF with typical brightness as measured by satellites. The readings of both plastic scintillators and simulation results can be seen in Figure 5.4.

Another detection of neutrons was reported in [195]. Neutrons were detected by gadolinium scintillators used in nuclear power plant after a lightning that was accompanied by TGF. The emission of neutrons lasted for approximately 100 ms. The height of TGF was estimated to be 2.5 km. The related measurement was published in [196]. Although in [196] the neutrons were not directly measured it showed a strong proof of photonuclear reactions taking place after a strong TGF. A strong afterglow was observed after the TGF. The afterglow corresponded to an emission of 511 keV photons emitted by beta plus decay radionuclides ^{13}N and ^{15}O with half life of 10 min and 122 s respectively. It is theorized that ^{13}N and ^{15}O radionuclides were generated by photonuclear reactions of high-energy bremsstrahlung with molecules of the air. The afterglow can be seen in Figure 5.5.

The results published in [196] are considered as important by [197] because it proves that neutrons are not produced by nuclear fusion since there would be no radioactive isotopes if there were only neutrons with energy of 2.45 MeV. Moreover, it describes a new way of forming radioisotopes in the atmosphere which could be potentially important for carbon dating.

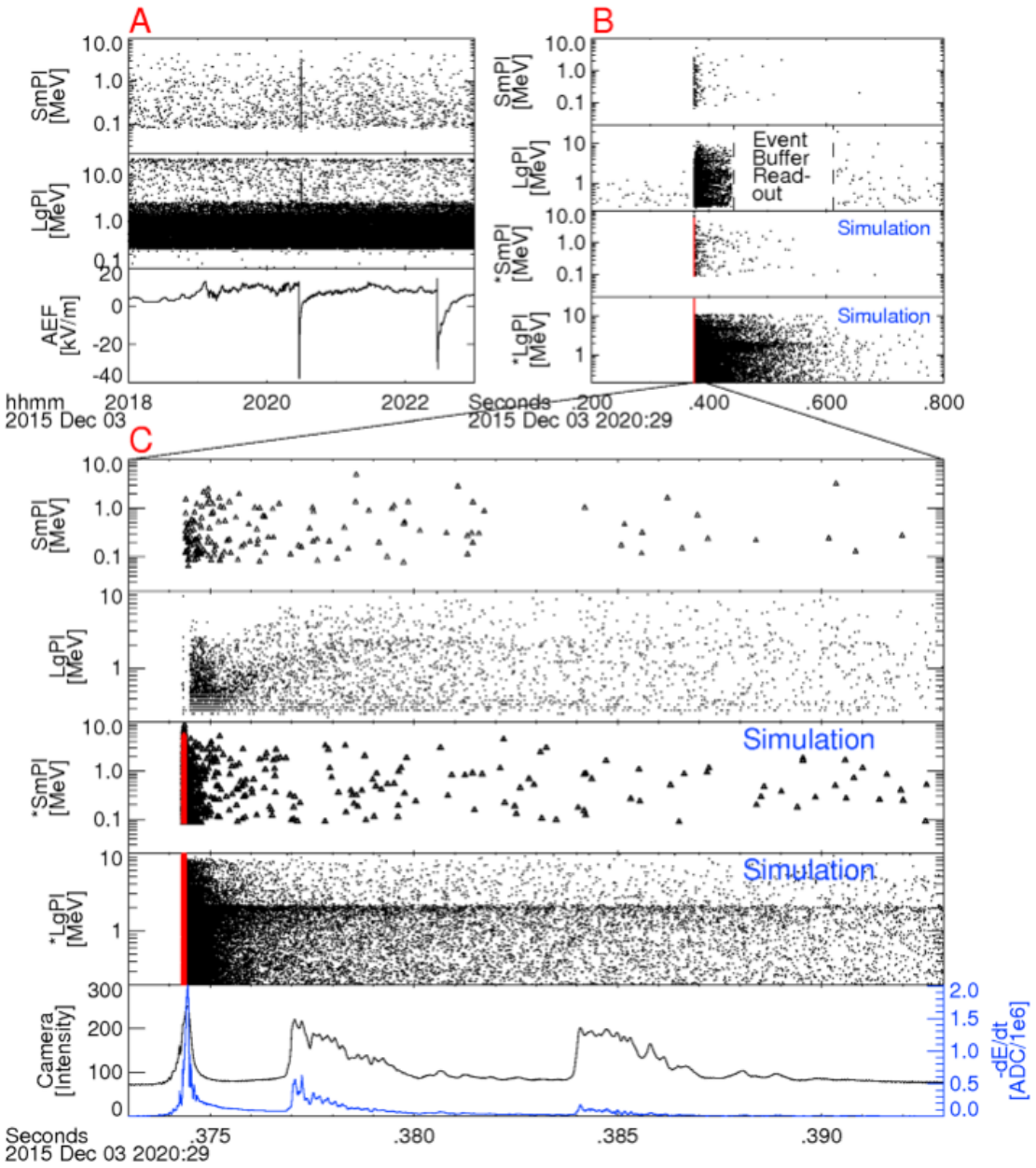

Figure 5.4: The comparison of two organic scintillators to strong TGF that occurred in close proximity with Monte Carlo simulations published in [194]. The visible peak at around 2 MeV from a large scintillator proves the interactions of thermal neutrons with hydrogen atoms in the scintillators.

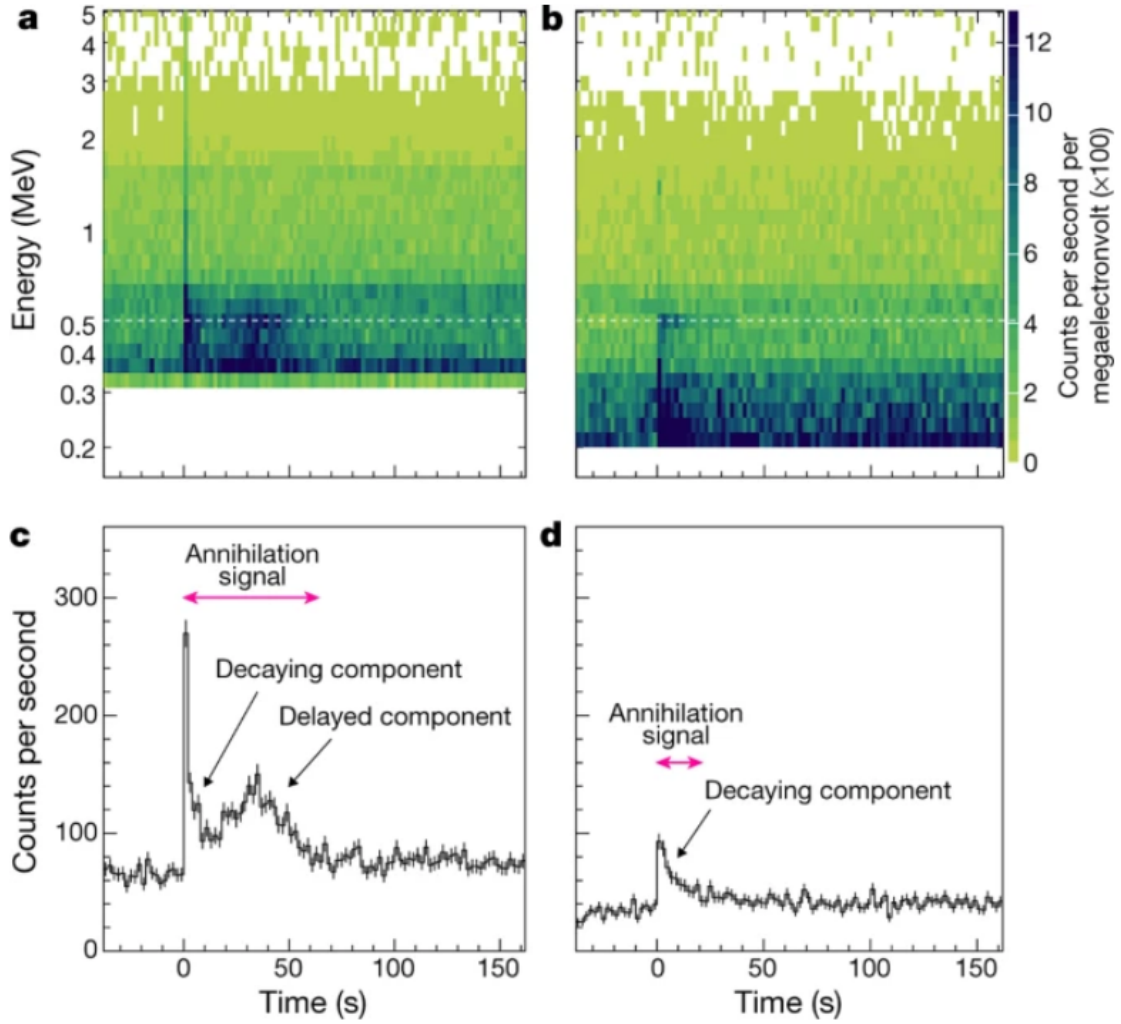

Figure 5.5: The annihilation signal measured in [196]. The annihilation components were measured by two different detectors and prove the generation of radionuclides in the atmosphere by photonuclear reactions from TGF.

5.2.4 Monte Carlo simulations of photoneutrons from TGF

The Monte Carlo simulations of neutron generation from TGF were covered in [198, 199, 200]. The neutron energy spectrum generated by photonuclear reactions can be seen in Figure 5.6. It shows that most of the neutrons are created by interactions with nitrogen and the minority is due to argon and oxygen. The energy of neutrons is relatively high and it can reach up to tens of MeV. The spatial distribution of photoneutrons can be seen in Figure 5.7. Interestingly, the neutrons can be detected even when the TGF is approximately 3.5 km above the detectors and lateral spread of neutrons can be up to 0.5 km. The time signature calculated by Monte Carlo simulation is shown in Figure 5.8. It can be clearly seen that during the first millisecond mainly fast neutrons arrive at the detector. These neutrons start to thermalize in the soil. After the first millisecond the majority of arriving neutrons have energy lower than 1 eV.

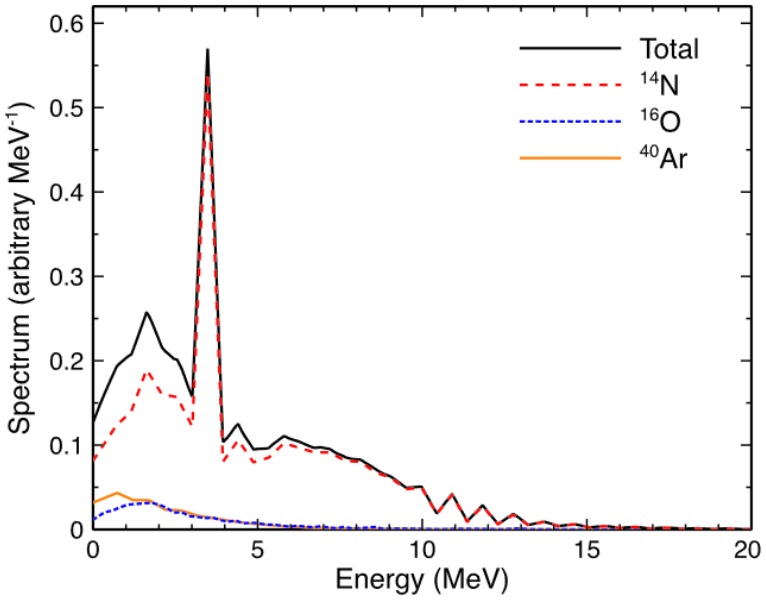

Figure 5.6: The neutron energy spectrum generated by photonuclear reactions. The final energy spectrum is defined mainly by nitrogen in the air and maximum energy reaches up to tens of MeV with a significant peak at energy of 3.5 MeV. The figure was taken from [199].

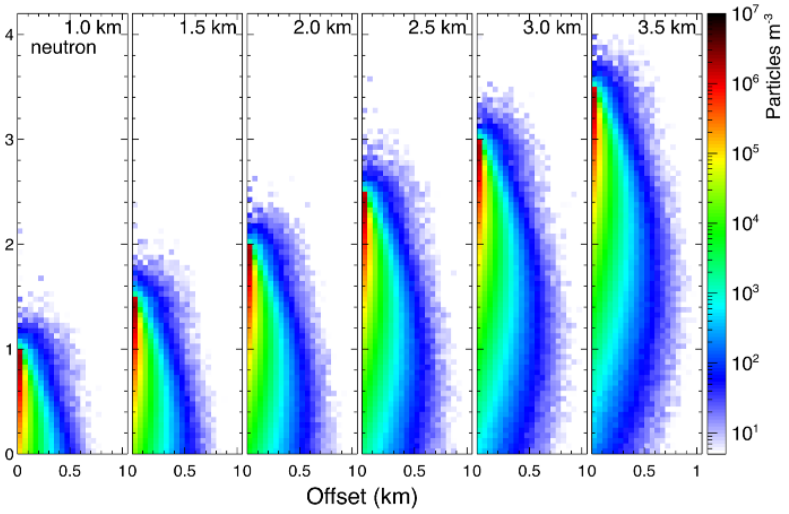

Figure 5.7: Spatial distribution of photoneutrons generated by TGF. The spatial distributions were calculated for six different altitudes of TGF. The most intense beam of neutrons is right below the place of origin but they spread up to 0.5 km laterally. The figure was taken from [199].

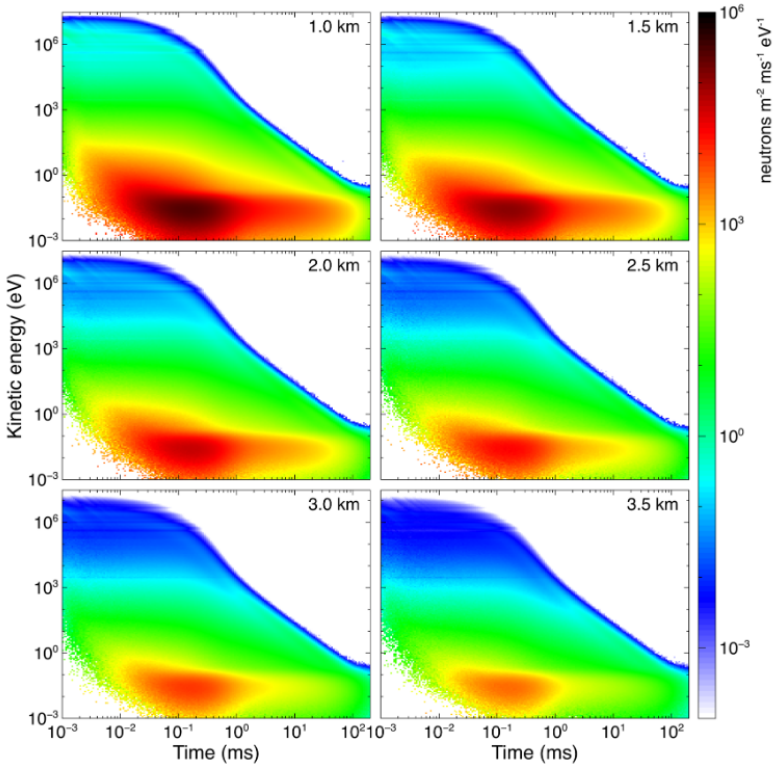

Figure 5.8: The time signature of photoneutrons from TGF taken from [199]. The time signatures were calculated for six different altitudes of TGF. Most of the fast neutrons arrive within the first millisecond and flux of thermalized neutrons can last up to hundreds of milliseconds.

5.3 Remarks

The lack of TGF ionizing radiation data from ground measurements shows how rare the TGFs are and how difficult it is to measure them. Interestingly, the measurement of TGF has never been reported at high-mountain observatories on Aragats and Lomnický štít which have frequently reported on TGEs and radiation from thunderstorms. Since the physics behind formation of downward and upward TGF is not yet fully understood, it is possible that there are not necessary conditions for TGF formation. As it was explained in this chapter, it is believed that the lack of TGF measurements done by satellites from high latitude places is caused mainly by the higher altitude of tropopause. It is possible that ionizing radiation coming toward ground and generated by an upward or downward TGF faces a similar fate as it is stopped by the atmosphere before it can be detected. In order to increase the probability of TGF detection the focus was aimed at detection of neutrons which have higher lateral spread and projected range in the air compared to photons and electrons which are usually detected. Although the high-mountain observatories on Aragats and Lomnický štít are equipped with various neutron detectors such as NM and SEVAN, they have not reported on measurement of downward TGF. There is one suspected measurement by NM and SEVAN with time resolution of 1 s published in [153]. The measurements of [201] with NM show that the sudden neutron count increases lasting for several milliseconds can be explained by physics of extended cosmic ray showers. Similar results were obtained in [202] stating that extensive cosmic rays showers can produce neutron bursts that last in order of milliseconds (Monte Carlo simulations show that neutrons from TGF can be expected to arrive up to 100 millisecond). So there is a significant discrepancy in measurements done at high-mountain observatories (lack of TGF and neutron measurements) and measurements from the USA (many TGFs detected) and Japan (TGFs with photonuclear reactions). Another reason why the focus was taken on detection of neutrons from TGF is that there are only two direct measurements of neutrons. Although both measurements give a lot of information about TGFs, there is still a wealth of information that has not been obtained. That is why the proposed detector focuses on event by event data processing, precise timestamping of the events and on discrimination of neutrons. The proposed neutron detector will be described and shown in Chapter 6. The plan is to do a series of measurements at the high-mountain observatory at Lomnický štít and the coast of Japan sea.

Chapter 6

Neutron detector for measurement of neutrons from Terrestrial Gamma Ray Flashes

Based on the experiences and measurements described in Chapter 5, the requirements and parameters of the neutron detector for measurement of photoneutrons from TGF were defined. The greatest shortcoming of most of the previously used detectors was their susceptibility to EMI, their sensitivity to high-energy gamma rays, and not having a possibility to discriminate between neutrons and photons. The proposed design attempts to solve these problems.
Based on the theoretical knowledge about photoneutrons from TGF, it can be expected that during the TGF a strong influx of photons will saturate the detector for several microseconds. This will be followed by a mixture of fast and thermal neutrons lasting up a millisecond. Thermalized neutrons are likely to arrive into the active volume of the detector after one millisecond only. Similar behavior was partially observed in [194] and was calculated by Monte Carlo simulations in [199, 200]. From that the parameters of the neutron detector can be derived. The requirements put on the neutron detector are summarized in Table 6.1.

Table 6.1: Summary of requirements on neutron detector for measurement of photonuclear neutrons generated from TGF.

Requirement	Reason
Dynamic range up to 20 MeV	Maximum energy of photoneutrons is appx. 20 MeV
Thermal neutron sensitivity	Large number of thermal neutrons expected - afterglow
Fast neutron sensitivity	Large number of fast neutrons expected within 1 ms after TGF
Excellent timing resolution	Precise calculation of the particles arival time
Fast signal pulses	Large particle flux
Discrimination between particles	Need to discriminate between neutrons and photons

6.1 Design of neutron detector

The design of neutron detector for measurement of photoneutrons from TGF is based on two liquid scintillators EJ-309B2.5 with PSD capabilities [203]. The detector is called a Stationary Neutron detector (SND). The PSD allows to discriminate between fast neutrons and photons. The liquid scintillators are loaded with 2.5% of natural boron which makes it possible to detect thermal neutrons via nuclear reaction of thermal neutrons with isotope B_5^{10}, as described in the following equation:

$$B_5^{10} + B_0^1 \rightarrow Li_3^7 + He_2^4 + \gamma(0.48MeV)(94\%) \tag{6.1}$$

The SND utilizes 2 different sizes of cylindrical scintillators - 5x5" and 2x2". This should ensure that the detector is not saturated by a large number of photons/neutrons as the smaller scintillator has lower probability of photon/neutron detection. The information about scintillators is summarized in Table 6.2. In order to utilize the full potential of the scintillators the output pulses need to be sampled by high frequency and with high resolution. Therefore, the pulses are digitized by an 8 channel CAEN digitizer DT5730 [204]. Data from the digitizer are sent to the computer via USB2.0. The PMTs are biased by a custom made high-voltage power supply.

Table 6.2: The summary of main components of scintillators and used high voltage.

Scintillator	Scint. size	PMT	High voltage (V)
EJ-309B2.5	5x5"	5" 9390B	-1030
EJ-309B2.5	2x2"	2" 9214B	-1230
Dummy - no scint.	-	2" 9216B	+1000

The digitizer is also fed by a signal from a dummy PMT which is there to register the effect of EMI on the electronics and the PMT. The dummy PMT is a biased PMT without any coupled scintillator. Another signal passing to the digitizer is a 1 second signal from GPS. This signal ensures the precision of the timestamping. The time resolution of the CAEN digitizer is sub nanosecond. The signals from PMTs are sampled by frequency of 500 MHz and with resolution of 14 bits. The CAEN digitizer allows to record raw data of each pulse or processed data. The data processing is done in an FPGA inside of the digitizer. The firmware DPP-PSD in DT5730 allows to determine the integral of the pulses and pulse shape discrimination parameter. The digital data processing is described in detail in the following text.
The schematic connection of individual components can be seen in Figure 6.1 and the photographs of large 5x5" scintillator, small 2x2" scintillator and CAEN digitizer can be seen in Figure 6.2, Figure 6.3, and Figure 6.4, respectively. The photograph of the whole SND can be seen in Figure 6.5.

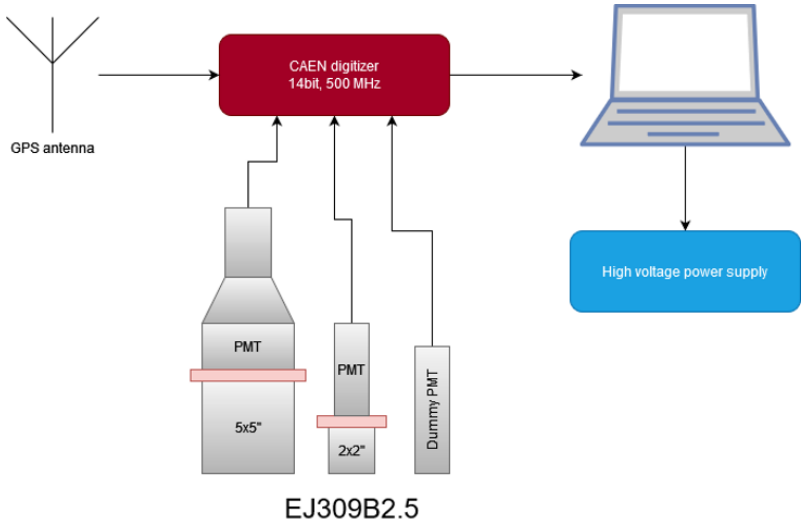

Figure 6.1: The schematic connection of SND components.

Figure 6.2: The large 5x5” scintillator EJ-309B2.5 coupled with photomultiplier tube 9390B.

Figure 6.3: The small 2x2” scintillator EJ-309B2.5 coupled with photomultiplier tube 9214B.

Figure 6.4: CAEN digitizer DT5730 with firmware version DPP-PSD.

Figure 6.5: Individual components of the SND.

6.2 Digital signal processing

The pulses from PMTs can be digitized and saved to the computer in raw version or they can be digitally processed by the FPGA in CAEN digitizer. The raw pulses were used for optimization of the PSD algorithm (determination of optimal short gate) and energy calibration, discrimination of thermal neutrons was done with already processed pulses. The processing of the signals is illustrated in Figure 6.6. The analysis of the pulse starts with calculating the baseline as an average of the samples before the pulse. If the baseline exceeds the set up threshold the pulse is recorded and analyzed.

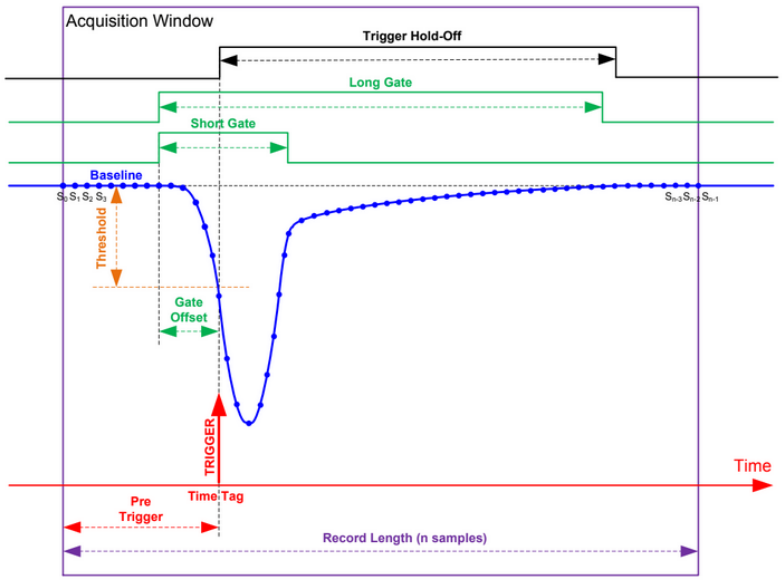

Figure 6.6: The illustration of signal processing in the CAEN digitizer.

The next important step is to calculate the trigger point by Constant Fraction Discrimination (CFD) method. It is a method based on branching the pulse into an inverted, delayed, and reduced pulse. The summation of both branches returns the pulse that has a zero crossing point which determines a trigger. The illustration of

the CFD trigger can be seen in Figure 6.7. The trigger point is used to calculate the start of the pulse by a gate offset. The integral of the pulse is defined as a summation of samples from the start of the pulse up to the end which is defined by a long gate parameter. The baseline value is deducted from the summed samples. A short gate is defined as a summation of baseline free samples from the start of the pulse up to a given length. The short gate integrates only a part of the pulse. The ratio between the short gate and the long gate is defined as a PSD parameter. This particular PSD algorithm is called a charge comparison method. Another important parameter is the trigger hold-off which determines when the trigger can be rearmed. There can be no other detection of a particle within the trigger hold-off time.

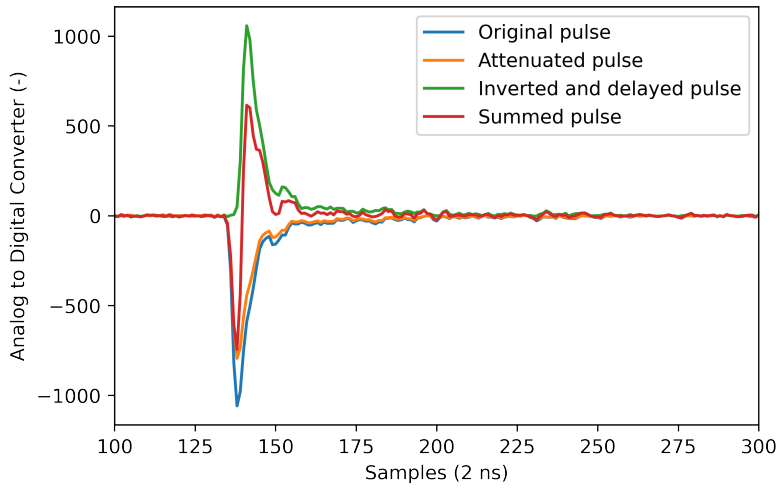

Figure 6.7: The illustration of CFD trigger algorithm.

The final tabulated parameters important for digital processing of the pulses are in Table 6.3. The example of a processed pulse from 2x2" EJ-309B2.5 scintillator with several highlighted attributes is shown in Figure 6.8.

Table 6.3: Tabulated optimal parameters for signal processing in CAEN digitizer.

Scintillator	2x2" EJ-309B2.5	5x5" EJ-309B2.5
Baseline samples (-)	32	32
CFS delay (ns)	6	6
CFS fraction (-)	75%	75%
Threshold (lsb)	20	20
Gate offset (ns)	14	22
Short gate (ns)	28	82
Long gate (ns)	120	200
Trigger hold-off (ns)	80	176

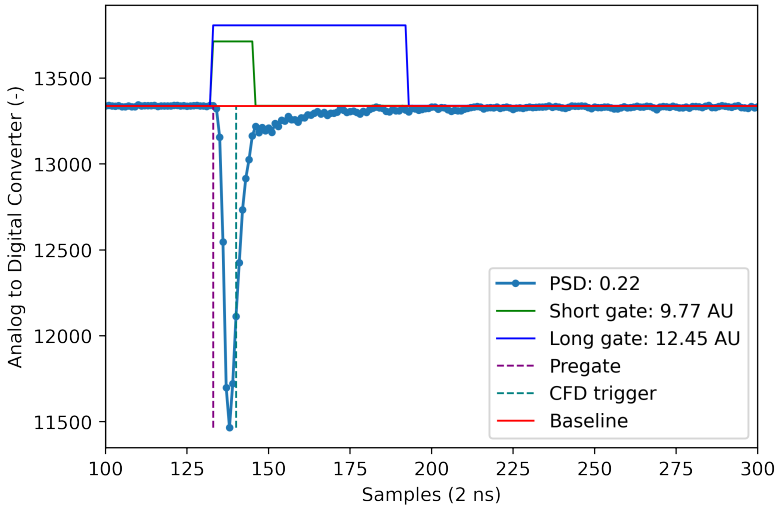

Figure 6.8: The example of processed pulse from 2x2" EJ-309B2.5.

6.3 Laboratory experiments

The SND underwent a series of experiments and tests in laboratory conditions. The goal was to optimize the parameter of short gate for the best possible photon/neutron discrimination, energy calibration, and finding the best parameters for thermal neutrons discrimination. The list of experiments and radiation sources that were used during the experiments is tabulated in Table 6.4.

Table 6.4: The list of experiments and radiation fields used for characterization of SND.

Place	Radiation source	Date
Technical University of Ostrava	14.1 MeV neutrons from ^{2}H+^{3}H generator	October 15th, 2021
Czech Metrological Institute	Neutrons from AmBe, ^{252}Cf and thermal neutrons	March 11th, June 3th, 2022
Nuclear Physics Institute	Gamma radiation from ^{22}Na, ^{60}Co, ^{137}Cs	March 15th, June 1st, 2022

6.3.1 Pulse shape discrimination optimization

The experiment at AmBe source was used for the optimization of pulse shape discrimination capabilities of both scintillators. The photograph of the irradiation setup can be seen in Figure 6.9. The distance between the source and the detector was 50 cm and 100 cm for 2x2" and 5x5" scintillator respectively. The AmBe source was shielded with a 2 mm lead cover. That helped to mitigate the 59.5 keV photons which are produced by ^{241}Am.

Raw pulses were saved and processed in Python scripting language as described in the previous text. The optimization parameter was only the short gate. The

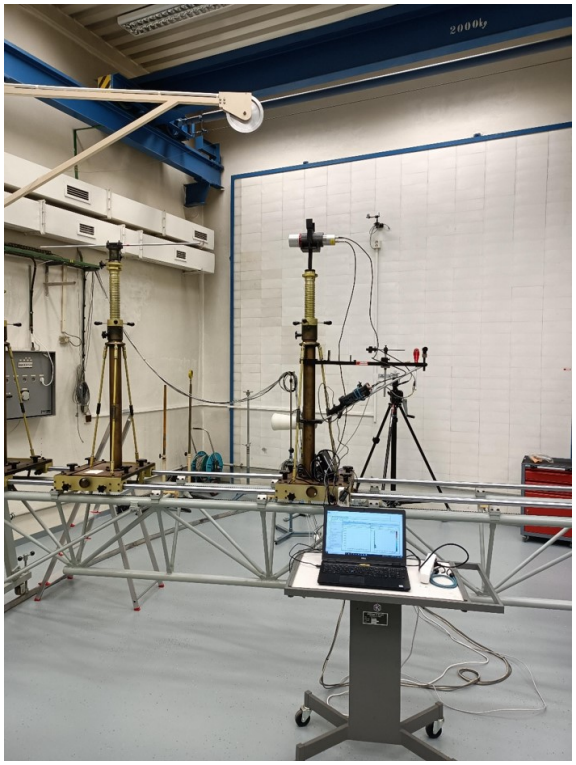

Figure 6.9: The irradiation setup of AmBe irradiation at Czech Metrological Institute in Prague.

processing was repeated for different values of the short gate parameter. The example of 2D histogram from AmBe measurement can be seen in Figure 6.10. The x axis represents deposited energy in arbitrary units and the y axis represents the charge comparison method parameter that is used to discriminate particles.

In order to quantify the quality of discrimination the 2D histogram was cut in several 1D histograms. Each cut represents detection in a narrow range of deposited energies of 4 arbitrary units. These 1D histograms were fitted with Gaussian Mixture Module (GMM) described by Equation (4.3). The figure of merit was calculated from the parameters of Gaussian curves. FOM is traditionally used to evaluate the quality of discrimination. The larger the FOM, the better the discrimination. The FOM points for different cuts create FOM function that is used to evaluate the optimal short gate settings. The FOM is calculated according to equation:

$$FOM = \frac{|\mu_1 - \mu_2|}{FWHM_1 + FWHM_2} \tag{6.2}$$

where μ is position of Gaussian curve maximum and FWHM is the full width of half maximum calculated from standard deviation according to equation:

$$FWHM = 2.35482 * \sigma \tag{6.3}$$

where σ is standard deviation of Gaussian curve. The GMM is also used to calculate the separation point which is defined as a point of the minimum between the two Gaussian maxima. The example of GMM fit is shown in Figure 6.11. The

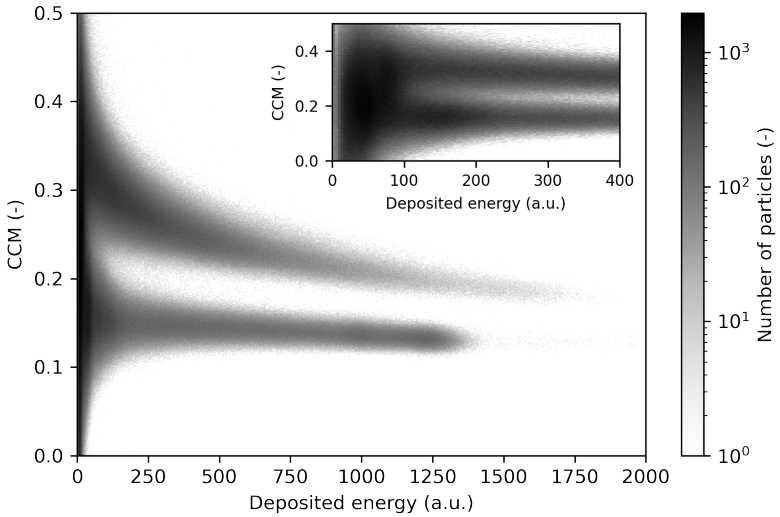

Figure 6.10: The 2D histogram of deposited energy and CCM parameter. Scintillator 2x2" is irradiated by AmBe beam. Two distinct regions are formed. The region with higher CCM parameter is the neutron component and the region with lower CCM parameter is made mostly of photons.

individual separation points are used to construct a separation function which defines a border between neutron and photon components. A spline interpolation is used to smooth the separation curve in higher energies. Small deviations are caused mainly due to the low counts in high-energy regions. The extrapolation of the separation curve is done in a way that the separation function remains constant. The example of the separation function and its corresponding FOM function is illustrated in Figure 6.12.

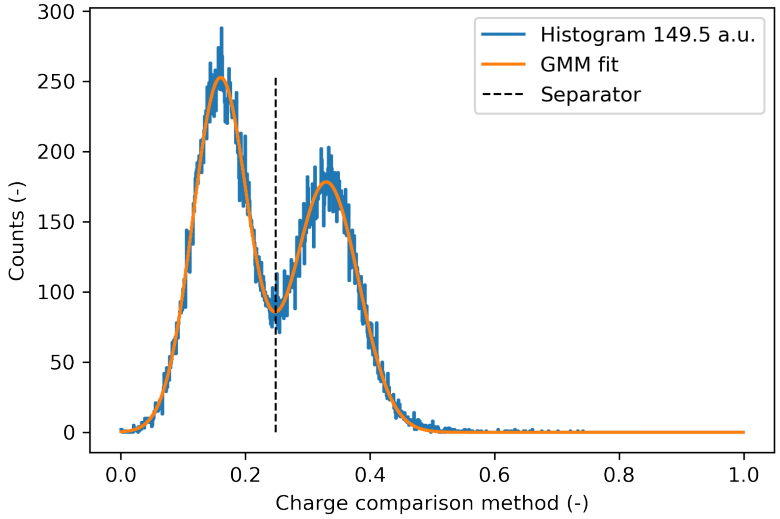

Figure 6.11: The example of 1D histogram cut. The histogram is fitted by GMM and a separation point is illustrated.

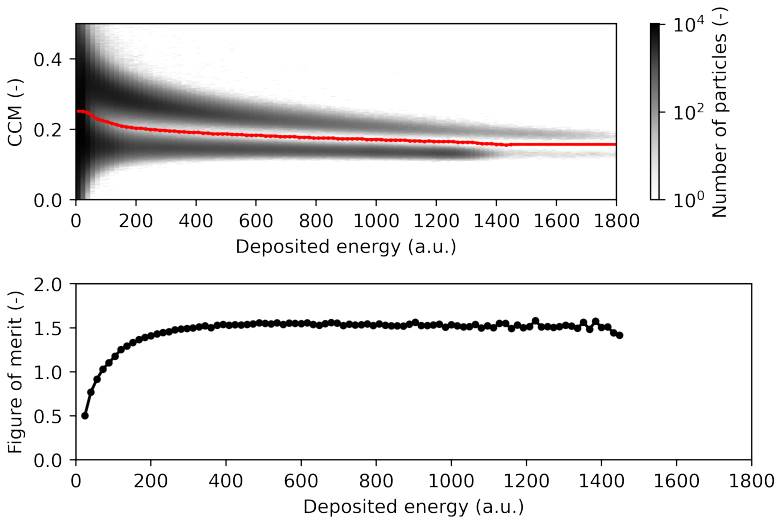

Figure 6.12: The example of a separation function (top plot) and FOM function (bottom plot).

The FOM functions for 11 different values of short gate parameters are compared in Figure 6.13. It is shown that the optimum values of short gate are 28 ns and 82 ns for 2x2" scintillator and 5x5" scintillator respectively.

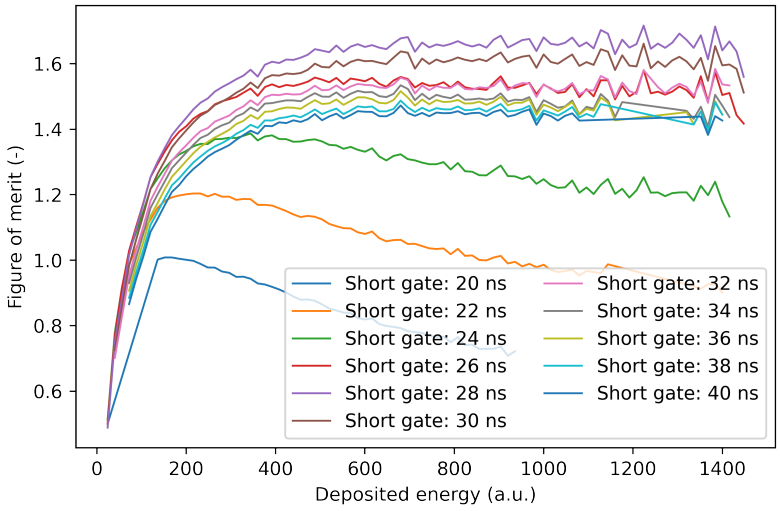

Figure 6.13: The optimization of the short gate parameter of 2x2" scintillator. It can be seen that the highest FOM values are achieved with a short gate of 28 ns.

6.3.2 Photon energy calibration

The energy calibration of the photon component is straightforward and was described in [131]. The proposed method uses gamma ray Compton edges of common radionuclides such as ^{22}Na, ^{60}Co, and ^{137}Cs and for high energy it uses photon components from AmBe source. The exact location of the Compton edge is determined

by a differential method described in [132]. The method uses a differential of histogram. The theoretical position of Compton edge can be calculated by Equation (4.4). The photon energy of used radionuclides and their Compton edges is tabulated in Table 6.5.

Table 6.5: The list of common gamma ray sources, their energy and corresponding Compton edges.

Gamma ray source	Energy (keV)	Compton edge (keV)
^{22}Na	511	339
^{22}Na	1275	1061
^{137}Cs	662	447
^{60}Co	1173	964
^{60}Co	1333	1117
AmBe	4438	4198

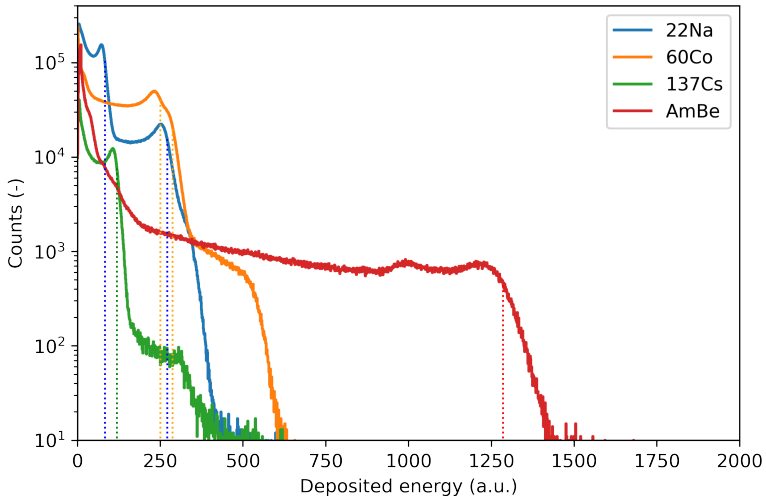

Figure 6.14: The deposited energy histograms of ^{22}Na, ^{60}Co, ^{137}Cs, and AmBe source measured with 2x2" scintillator. The corresponding Compton edges are highlighted by vertical dashed lines.

The histograms of ^{22}Na, ^{60}Co, ^{137}Cs, and AmBe source can be seen in Figure 6.14. The locations of Compton edges were fitted by equation described in [131]:

$$N = A * log(B * E + 1) + C * E \tag{6.4}$$

where A, B, C are fitting parameters, E is the deposited energy (in MeV) and N is the measured channel. The calibration curves of both scintillators are shown in Figure 6.15.

6.3.3 Neutron energy calibration

The energy calibration that is used for the photon component cannot be used for the neutron component due to the effect of energy quenching. The energy quench-

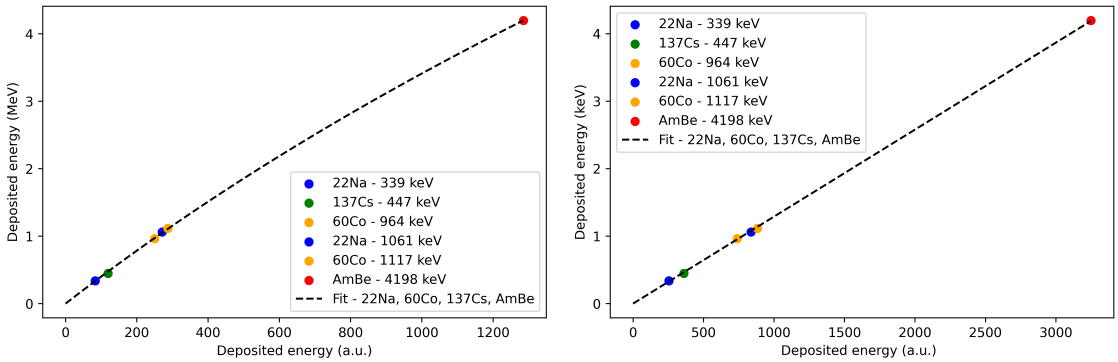

Figure 6.15: The calibration curve of the photon component of the 2x2" scintillator is on the left and the analogy for the 5x5" scintillator is on the right.

ing causes lower light yield of particles with higher LET. It has been described in organic and inorganic scintillators as well [133, 134, 135, 136]. The mathematical model is described by Equation (4.7). This method was used in [138]. The fitting parameters a, b, c were calculated for scintillator EJ-309 of 5x5" and EJ-309 3x3". The same parameters were used for scintillators EJ-309B2.5 5x5" and EJ-309B2.5 2x2" respectively. The used parameters are shown in Table 6.6. The translation of fitting parameters was verified by irradiation at a D+T generator which produces neutrons with energy of 14.1 MeV.

Table 6.6: The neutron calibration parameters used for 2x2" and 5x5" scintillators.

Fitting parameter	2x2" EJ-309B2.5	5x5" EJ-309B2.5
a (-)	0.817	0.748
b (MeV)	2.629	2.410
c (1/MeV)	0.297	0.298

The use of fitting parameters should result in maximum measured neutron energy of 14.1 MeV. In Figure 6.16 and Figure 6.17 the neutron edges are shown at 13.8 MeV for 2x2" scintillator and 13.2 MeV for 5x5" scintillator respectively. This is a 2% and 7% difference compared to the energy of 14.1 MeV. Although the translation of fitting parameters worsens the neutron energy resolution, it is sufficient for the application. The parameters could be improved if the detector was irradiated at a D+D generator which produces neutrons with energy of 2.45 MeV. Then the parameters could be refitted to agree with the two neutron edges.

6.3.4 Discrimination of thermal neutrons

The identification of thermal neutrons is based on the reaction described in Equation (6.1). The reaction results in alpha particles and lithium ions with large LET. Due to the energy quenching, the final light output is significantly lower than it would be if the same energy was deposited by a low LET particle. According to the datasheet [203] the resulting observed energy should be about 80 keVee (kiloelectron volt electron equivalent).

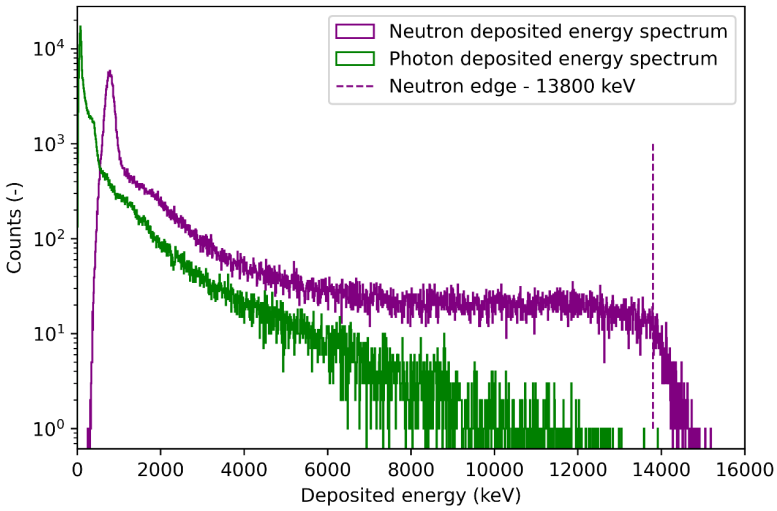

Figure 6.16: The localization of 14.1 MeV neutron edge for 2x2" scintillator.

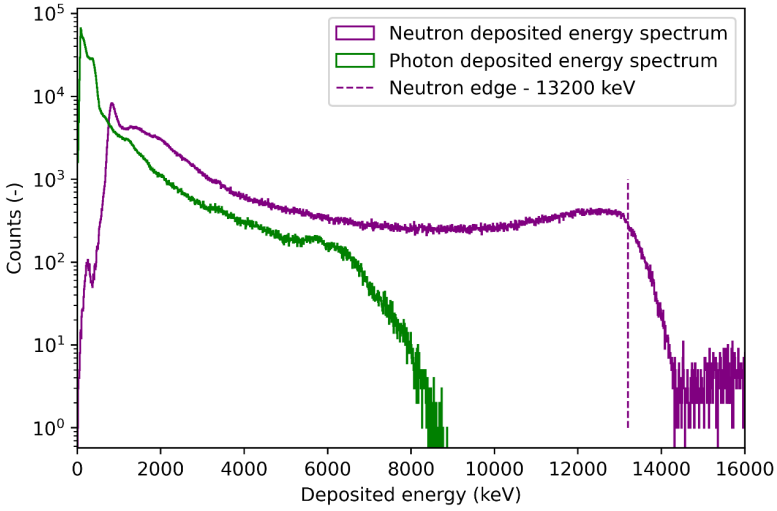

Figure 6.17: The localization of 14.1 MeV neutron edge for 5x5" scintillator.

To define the thermal neutron regions, the SND was irradiated at a carbon prism that thermalizes fast neutrons from AmBe sources and hence generates a thermal neutron beam. The irradiation experiment at prism can be seen in Figure 6.18.

Figure 6.18: A photograph of irradiation of 2x2" scintillator at a prism made of carbon at Czech Metrological Institute. Six AmBe neutron sources are inserted inside the prism.

The identification of thermal neutrons was done via thresholding of 2D histograms. The resulting channels defining the thermal neutrons can be seen in Figure 6.19 and Figure 6.17 (2x2" and 5x5" respectively). It is shown that the main cluster of neutrons is located in the region around 80 keVee and spreads in PSD of both photon and neutron domains.

Since the reactiondexcribed in Equation (6.1) has a large probability of creating a photon with energy of 478 keV it is possible that this photon is detected by a detector along with the thermal neutron [205]. This causes an increase in the probability of detecting Compton scatter of such photons hence there is another region which is related to the enhancement in thermal neutrons. This region is also thresholded and taken into consideration. The effect is more visible in the 5x5" scintillator as it is more likely to absorb the 478 keV photon. The borders that shows discrimination regions in both detectors are plotted in Figure 6.21. It can be seen that there is an overlap between individual regions, therefore, they can be contaminated by other types of different radiation. That might cause a problem when evaluating the data from thunderstorms hence the data analyses must be done with caution. Nevertheless, the improvement in quality of data compared to, for example, the GODOT detection system should be significant.

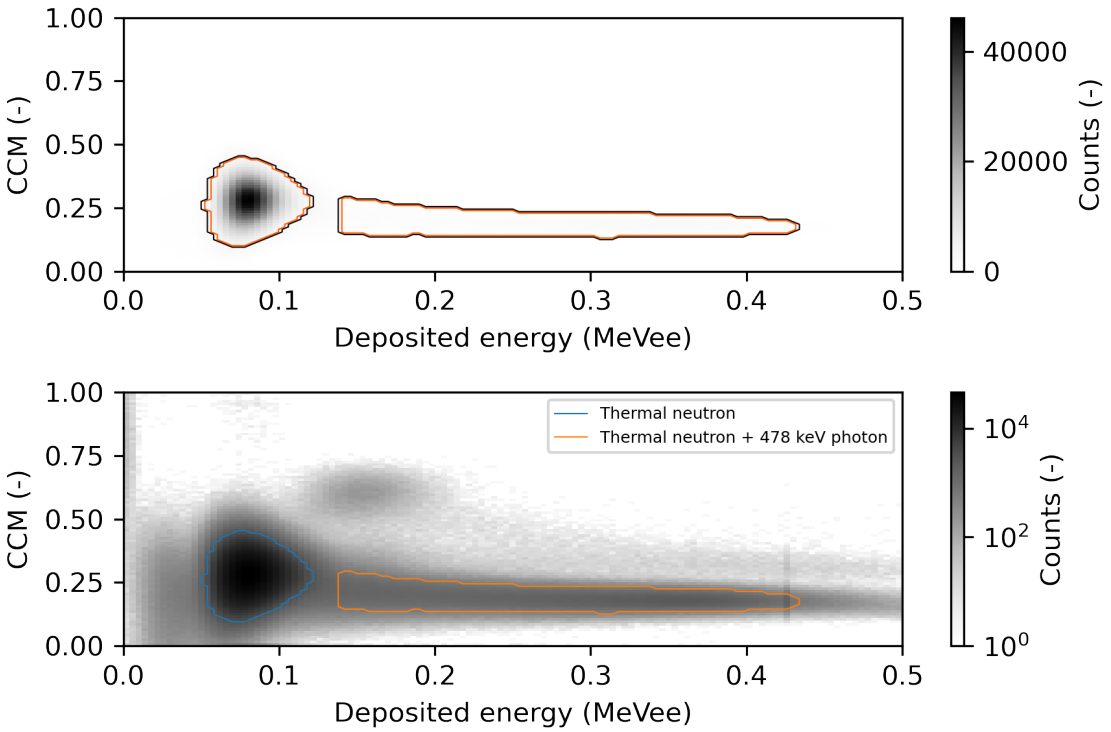

Figure 6.19: The thermal neutron regions defined for the 2x2" scintillator. The top plot shows the 2D histogram in linear scale and the bottom plot shows the same 2D histogram in logarithmic plot.

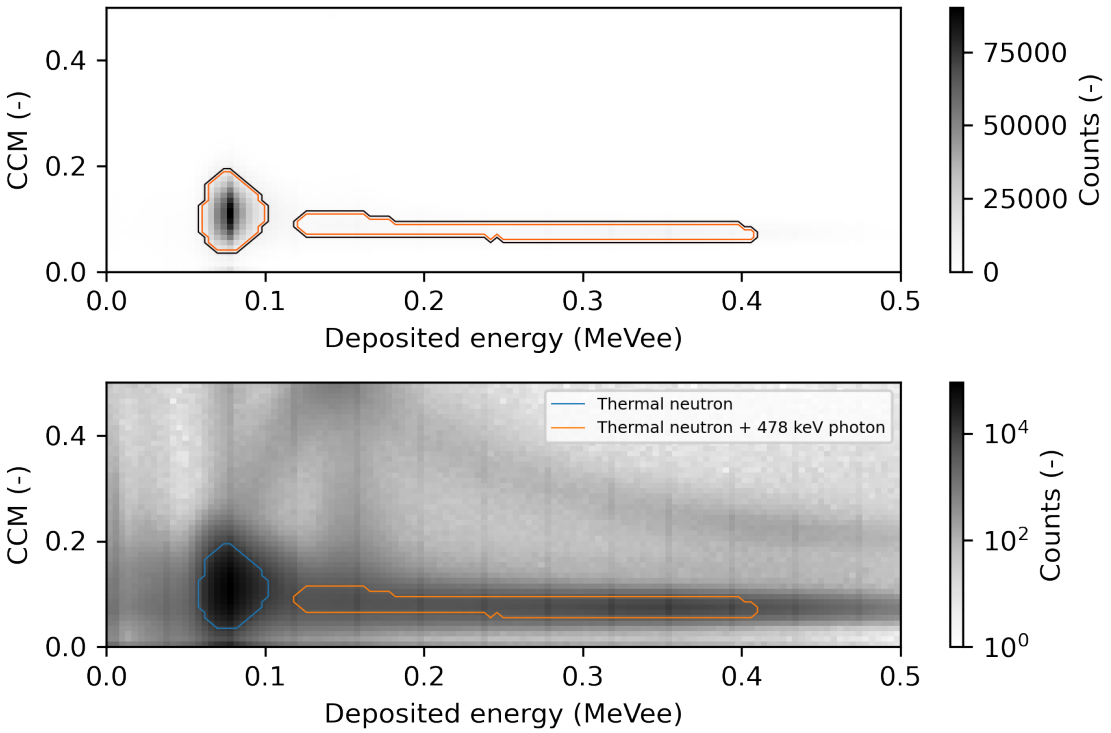

Figure 6.20: The thermal neutron regions defined for the 5x5" scintillator. The top plot shows the 2D histogram in linear scale and the bottom plot shows the same 2D histogram in logarithmic plot.

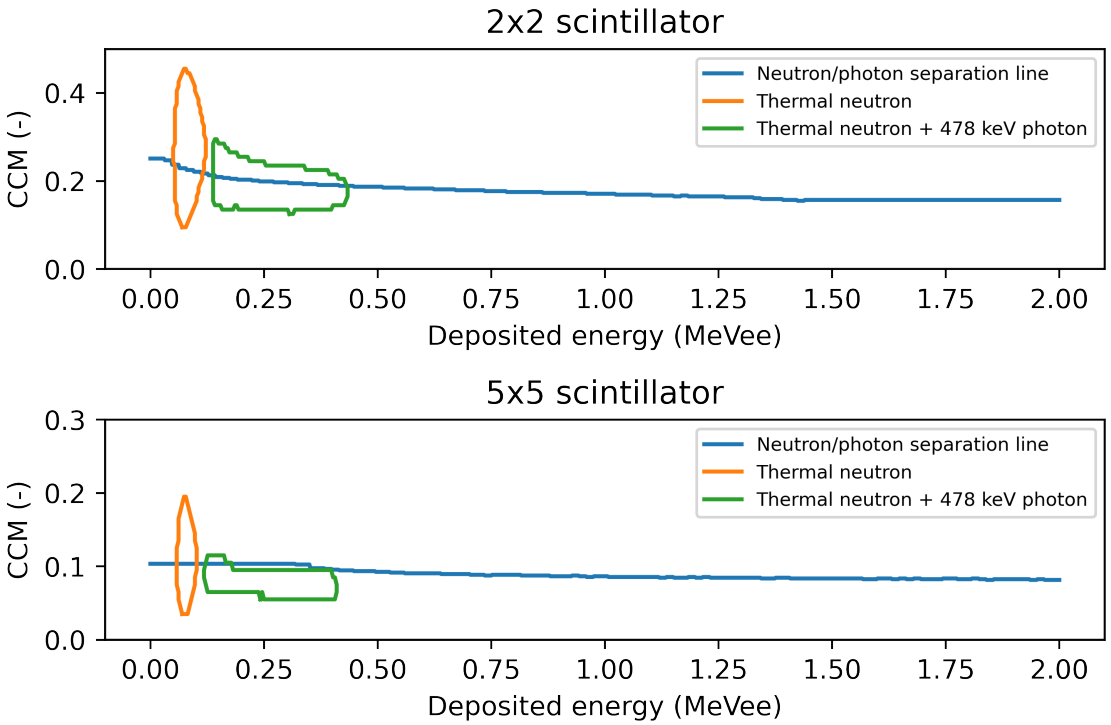

Figure 6.21: The top plot shows separation regions of 2x2" scintillator and the bottom plot shows separation regions of 5x5" scintillator.

6.4 Results

6.4.1 Thunderstorm measurements

After the SND was optimized, tested and calibrated it was placed at high-mountain observatory on Lomnický štít on June 28th 2022. The setup of the SND is shown in Figure 6.22. The measurement has suffered several interruptions due to the controlling software instability. The SND was active during several thunderstorms. The increased count rates caused by radon washout can be seen in Figure 6.23. The figure shows five defined channels - neutrons, fast neutrons (>2 MeV), photons, thermal neutrons, and thermal neutrons + 478 keV photons. Theoretically, the number of neutrons should be independent of radon washout because the gamma rays associated with radon progenies do not have sufficient energy to produce neutrons by photoreactions nor any other way to produce fast or thermal neutrons. We can see that the channels with neutrons, thermal neutrons and thermal neutrons with 478 keV photons follow the increases of gamma rays caused by radon. That is caused solely by contamination of these channels by gamma rays. Low energy photons especially can be assigned to neutrons since the PSD technique is less reliable for low energies and thermal region spreads over photon and neutron domain. The contamination of the thermal neutron + 478 keV region is not surprising since it is almost entirely located in the photon domain. On the other hand, fast neutrons with energies >2 MeV do not follow radon increases and are very stable over time.

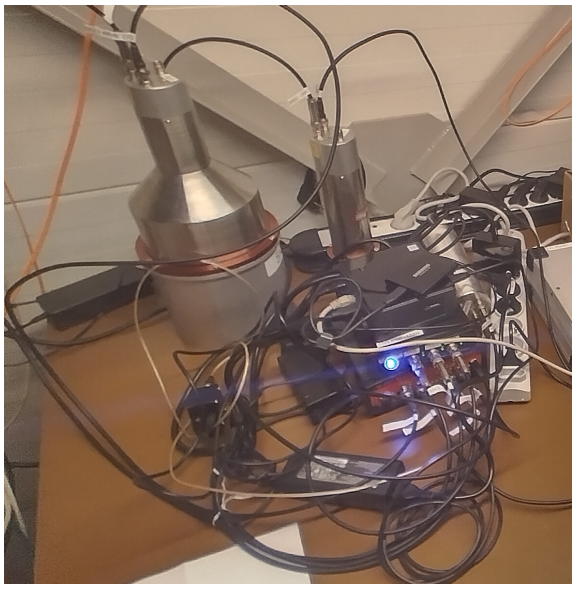

Figure 6.22: The SND is located in a shelter at high-mountain observatory at Lomnický štít.

6.4.2 TGF searching algorithm

The amount of data from the SND is relatively large (hundreds of MB per day) and it is not feasible to go through the data manually and search for the subsecond

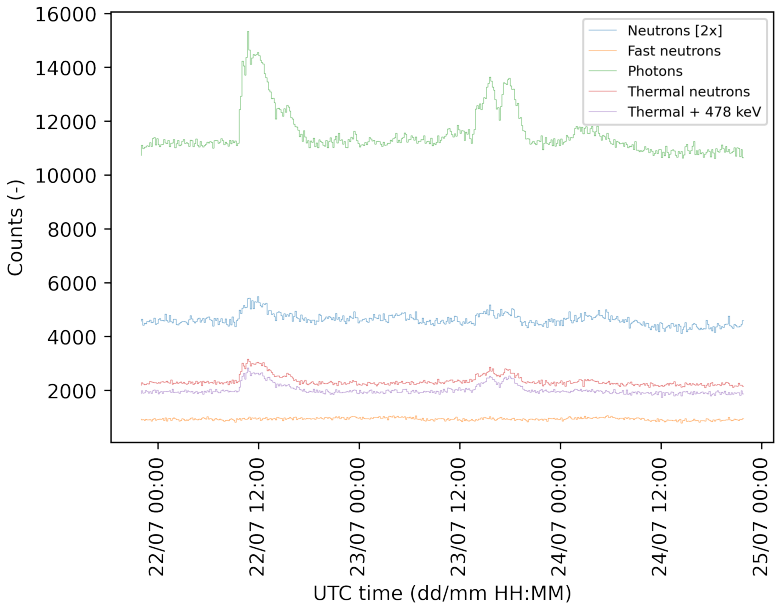

Figure 6.23: Time series data from 2x2" scintillator showing increases in count rates in several components during thunderstorms on Lomnický štít in 2022. The majority of the enhancement is presumably caused by radon progenies that are washed out from the air during rain.

enhancements potentially caused by TGFs. Therefore a simple searching algorithm was created. The searching algorithm focuses on thermal neutrons which should be present up to 100 ms after the TGF. The individual thermal neutron events with time stamps are binned into 50 ms bins. The time series data are smoothed by a low-pass Gaussian filter. Then the thermal neutron count in each bin is subtracted by filtered data value. The standard deviation of the resulting difference is calculated and only values that exceed 5 sigma are taken into consideration as potential neutrons caused by TGF. It is assumed that the enhancement of thermal neutrons would be seen in both detectors. Therefore, an additional condition that both detectors must show the enhancement over 5 sigma values is imposed. The anomaly with increase of thermal neutron count rates of 4.77 and 4.71 sigma values is shown in Figure 6.24. Although it is the largest anomaly registered so far, it does not correspond to the expected behavior which can be expected from TGF. There is no increase of fast neutrons along with the increase of thermal neutrons and the increase in thermal neutrons is relatively small. Moreover, during that time there was no thunderstorm or lightning nearby.

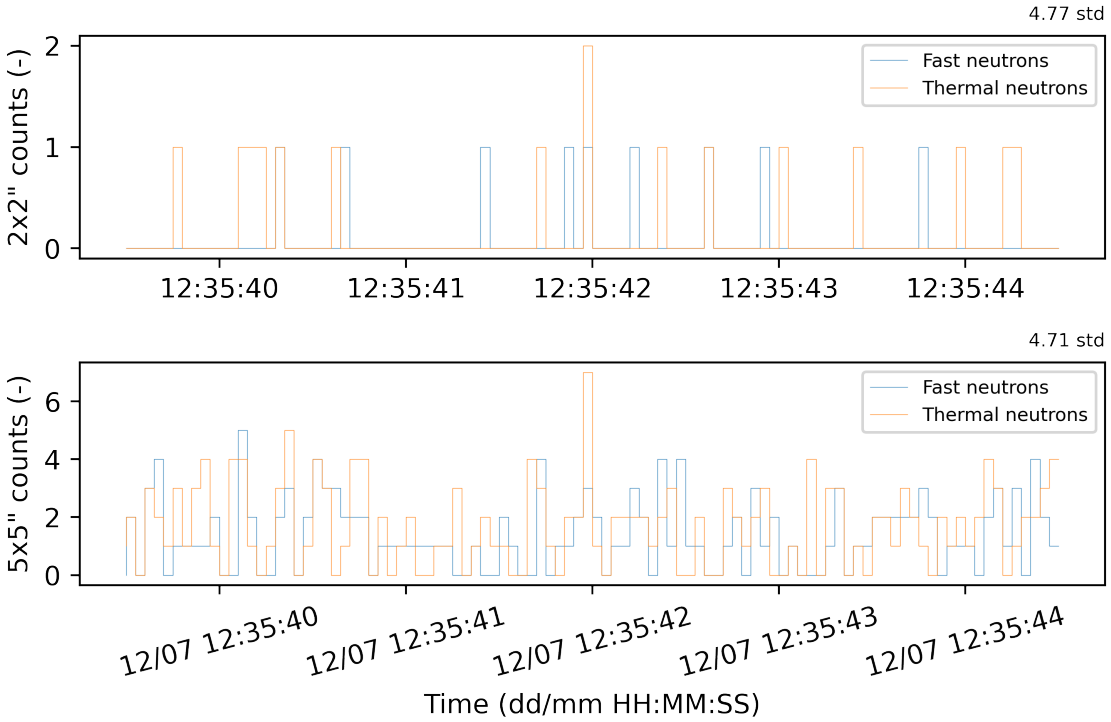

Figure 6.24: The result of TGF searching algorithm showing the largest detected short term increase in count rates of both scintillators.

6.5 Remarks

The SND for measurements of photonuclear neutrons generated by TGFs was designed and constructed. Its parameters and features were chosen in order to meet the expected parameters of photonuclear neutrons from TGF. The SND was extensively tested, calibrated, optimized and characterized in various radiation fields.
The SND was located at a high-mountain observatory at Lomnický štít. It has not registered any significant short term enhancement of fast neutrons nor thermal neutrons that can be expected from TGF. Since it is a very rare phenomenon, it can take years to register one TGF event. Even at places where TGFs were historically measured such as Japan and Florida, the probability is relatively low. The SND has been sent to Kanazawa district in Japan for winter season 2022/2023. It is planned to use SND at various high-mountain observatories in Europe for the summer season.
The main focus was to design a detector which will be able to obtain additional information compared to the previously used detectors such as GODOT and PANDA. The SND can theoretically measure fast neutron component as well as thermalized neutrons which can be measured up to 100 ms after the TGF. It offers higher sensitivity to thermal neutrons than GODOT as it uses a nuclear reaction of boron with a high cross section. Moreover, it can discriminate fast neutrons from photons. Hence, it should be able to extract limited information about the fast neutron energy spectrum. It also features a control PMT so the effect of EMI from lightning on the detector can be observed. All together it should give the unambiguous information

about photonuclear neutrons from TGF.
The future work includes the calculation of response function of fast and thermal neutrons and gamma rays. Another improvement of the SND would be irradiation on the $^{2}H+^{2}H$ generator (2.45 MeV neutrons) so the fast neutron calibration coefficients can be revised.

Chapter 7

Conclusions

The goals introduced in Chapter 1 were fulfilled and completed. The first goal was achieved in Chapter 3 and supported by two published papers [8, 92]. The limitations of semiconductor detectors for measurement in mixed radiation fields were summarized in [92]. It was shown that the neutral particles, gamma rays and neutrons, interact with silicon differently than with tissue and it was quantified in terms of dose equivalent. Moreover, a new method for determination of absorbed dose conversion coefficient based on LET was introduced. This method is applicable for example on silicon telescopes which have been used onboard aircraft and in space environments. Another shortcoming of silicon detectors was demonstrated in their energy calibration methods which likely caused large discrepancies between individual detectors. In [8], a new calibration method based on comparison of silicon detectors with pixel detector Timepix was demonstrated. This method allows precise determination of the detector energy threshold which significantly influences the measurements of absorbed dose (up to tens of percent) and also the calibration coefficients. Therefore, the translation of calibration coefficients which might produce errors between detectors can be minimized. Although the silicon detectors have a long history of being used onboard aircraft, these limitations restrict their capabilities to characterize the mixed radiation fields and to precisely determine the dosimetric quantities such as dose equivalent. Since the silicon detectors rely on a coefficient that is dependent on location in most of the calibration methods, they are not able to indicate changes in the quality of the radiation field especially the changes in neutron component. They might only indicate the changes in the total amount of the charged particles as they are mainly sensitive to them. The use of a silicon detector alone is probably sufficient to monitor and verify the models for calculation of aircrew effective doses; it is not sufficient for research of SPEs which are likely to cause a change in mixed radiation fields composition in the atmosphere or for radiation fields in other than flight altitudes where the composition of the radiation is different.

For that reason, the concept and design of a new detector based on a plastic scintillator was introduced in Chapter 4. This concept is proposed to be able to measure the neutrons and discriminate them based on the PSD parameter. The model of plastic scintillator coupled with SiPM, introduced in [123], helped with the understanding of the detector response and its optimization. The proposed detector was

extensively tested and characterized and finally tested onboard aircraft. The testing campaign consisted of two flights. The measured results suggested a good agreement of the neutron component with software CARI-7 and poor agreement in the low LET component. This is likely caused by the energy quenching of the ionizing radiation in the plastic scintillator. Therefore, a combination of data from silicon detector and proposed detector was used to determine a dose equivalent. This resulted in an excellent agreement between the measurement and CARI-7 data. Hence, it was proven that the detector can be used to enhance the precision for verification of the models and additionally, it can be useful for research of SPE events and monitoring space weather as it is able to determine the contributions of the low and high LET components without being biased by the use of location based coefficients.
The thunderstorm phenomena of TGE and TGF were described in Chapter 5. The chapter is focused on TGF phenomenon measurement description, their deficiencies and limitations. The goal was to design a detector intended for the measurement of neutrons generated by photonuclear reactions taking place during TGF and to enhance the existing measurements. The proposed neutron detector SND is described in Chapter 6. The design with two detectors based on liquid scintillators was introduced. The detector consists of (1) a dummy PMT to analyze the effects of EMI and (2) liquid scintillators that are capable of PSD and are sensitive to thermal neutrons due to the enhancement of natural boron. Due to the excellent time resolution and fast pulses, the detector is able to register large fluxes of ionizing radiation. All these properties make it suitable for measurement of ionizing particles created by TGF. The detector was extensively tested, characterized and optimized for the best performance. It was deployed on a short testing campaign at a high-mountain observatory at Lomnický štít where no TGF has ever been measured. The algorithm for searching of unusual events was proposed and implemented. The current plans include a measurement campaign during winter thunderstorms in Japan where several TGFs have already been registered.

List of Figures

List of Tables

Bibliography

1. ISO. *ISO 15390:2004* [online]. 2004. [visited on 2022-11-01]. Available from: `https://www.iso.org/standard/37095.html` (cit. on p. 9).
2. TYLKA, Allan J; ADAMS, James H; BOBERG, Paul R; BROWNSTEIN, Buddy; DIETRICH, William F; FLUECKIGER, Erwin O; PETERSEN, Edward L; SHEA, Margaret A; SMART, Don F; SMITH, Edward C. CREME96: A revision of the cosmic ray effects on micro-electronics code. *IEEE Transactions on Nuclear Science*. 1997, **44**(6), 2150–2160 (cit. on p. 9).
3. (EURADOS), European Radiation Dosimetry Group. Exposure of air crew to cosmic radiation. A report of EURADOS Working Group 11, EURADOS Report 1996.01. *European Commission Report Radiation Protection 85*. 1996 (cit. on p. 9).
4. LINDBORG, Lennart; BARTLETT, David; BECK, Peter; MCAULAY, Ian; SCHNUER, Klaus; SCHRAUBE, Hans; SPURNÝ, Frantisek. Cosmic radiation exposure of aircraft crew: compilation of measured and calculated data. *Radiation protection dosimetry*. 2004, **110**(1-4), 417–422 (cit. on pp. 9, 26).
5. LANTOS, P; FULLER, N. History of the solar particle event radiation doses on-board aeroplanes using a semi-empirical model and Concorde measurements. *Radiation Protection Dosimetry*. 2003, **104**(3), 199–210 (cit. on p. 9).
6. BOTTOLLIER-DEPOIS, Jean-Francois; BECK, Peter; LATOCHA, Marcin; MARES, Vladimir; MATTHIÄ, D; RÜHM, W; WISSMANN, Frank. Comparison of codes assessing radiation exposure of aircraft crew due to galactic cosmic radiation. *EURADOS report*. 2012, **3**, 2012 (cit. on pp. 9, 65).
7. AMBROŽOVÁ, Iva; BECK, Peter; BENTON, Eric R; BILLNERT, Robert; BOTTOLLIER-DEPOIS, Jean-Francois; CARESANA, Marco; DINAR, Nesrine; DOMAŃSKI, Szymon; GRYZIŃSKI, Michał A; KÁKONA, Martin, et al. REFLECT–research flight of EURADOS and CRREAT: intercomparison of various radiation dosimeters onboard aircraft. *Radiation measurements*. 2020, **137**, 106433 (cit. on pp. 9, 23, 24, 27–29, 46).
8. SOMMER, Marek; ŠTĚPÁNOVÁ, Dagmar; KÁKONA, Martin; VELYCHKO, Olena; AMBROŽOVÁ, Iva; PLOC, Ondřej. CALIBRATION OF SILICON DETECTORS LIULIN AND AIRDOS USING COSMIC RAYS AND TIMEPIX FOR USE AT FLIGHT ALTITUDES. *Radiation Protection Dosimetry*. 2022, **198**(9-11), 597–603 (cit. on pp. 9, 23, 24, 27–31, 34, 100).

9. FISHMAN, Gerald J; BHAT, PN; MALLOZZI, R; HORACK, JM; KOSHUT, T; KOUVELIOTOU, C; PENDLETON, GN; MEEGAN, CA; WILSON, RB; PACIESAS, WS, et al. Discovery of intense gamma-ray flashes of atmospheric origin. *Science*. 1994, **264**(5163), 1313–1316 (cit. on pp. 10, 68).

10. GREFENSTETTE, Brian W; SMITH, David M; HAZELTON, BJ; LOPEZ, LI. First RHESSI terrestrial gamma ray flash catalog. *Journal of Geophysical Research: Space Physics*. 2009, **114**(A2) (cit. on pp. 10, 68).

11. SMITH, DM; DWYER, JR; HAZELTON, BJ; GREFENSTETTE, BW; MARTINEZ-MCKINNEY, GFM; ZHANG, ZY; LOWELL, AW; KELLEY, NA; SPLITT, ME; LAZARUS, SM, et al. A terrestrial gamma ray flash observed from an aircraft. *Journal of Geophysical Research: Atmospheres*. 2011, **116**(D20) (cit. on pp. 10, 68).

12. DWYER, JR; RASSOUL, HK; AL-DAYEH, M; CARAWAY, L; WRIGHT, B; CHREST, A; UMAN, MA; RAKOV, VA; RAMBO, KJ; JORDAN, DM, et al. A ground level gamma-ray burst observed in association with rocket-triggered lightning. *Geophysical Research Letters*. 2004, **31**(5) (cit. on pp. 10, 69).

13. WADA, Yuuki; ENOTO, Teruaki; NAKAZAWA, Kazuhiro; FURUTA, Yoshihiro; YUASA, Takayuki; NAKAMURA, Yoshitaka; MORIMOTO, Takeshi; MATSUMOTO, Takahiro; MAKISHIMA, Kazuo; TSUCHIYA, Harufumi. Downward terrestrial gamma-ray flash observed in a winter thunderstorm. *Physical Review Letters*. 2019, **123**(6), 061103 (cit. on pp. 10, 69).

14. CHILINGARIAN, A; DARYAN, A; ARAKELYAN, K; HOVHANNISYAN, A; MAILYAN, B; MELKUMYAN, L; HOVSEPYAN, G; CHILINGARYAN, S; REYMERS, A; VANYAN, L. Ground-based observations of thunderstorm-correlated fluxes of high-energy electrons, gamma rays, and neutrons. *Physical Review D*. 2010, **82**(4), 043009 (cit. on pp. 10, 67, 70–72).

15. KUDELA, K; CHUM, J; KOLLÁRIK, M; LANGER, R; STRHÁRSKÝ, I; BAŠE, J. Correlations between secondary cosmic ray rates and strong electric fields at Lomnický štít. *Journal of Geophysical Research: Atmospheres*. 2017, **122**(20), 10–700 (cit. on pp. 10, 67).

16. DWYER, JR; SMITH, DM; UMAN, MA; SALEH, Z; GREFENSTETTE, B; HAZELTON, B; RASSOUL, HK. Estimation of the fluence of high-energy electron bursts produced by thunderclouds and the resulting radiation doses received in aircraft. *Journal of Geophysical Research: Atmospheres*. 2010, **115**(D9) (cit. on pp. 10, 69).

17. PALLU, Melody; CELESTIN, Sebastien; TROMPIER, Francois; KLERLEIN, Michel. Estimation of radiation doses delivered by Terrestrial Gamma ray Flashes within leader-based production models. *Journal of Geophysical Research: Atmospheres*. 2021, **126**(8), e2020JD033907 (cit. on pp. 10, 69).

18. HESS, Victor F. On the absorption of gamma-radiation in the atmosphere. *Phys. Zeit.* 1911, **12**(32), 998–1001 (cit. on p. 12).

19. HESS, Viktor F. Uber Beobachtungen der durchdringenden Strahlung bei sieben Freiballonfahrten. *Phys. Zeits.* 1912, **13**, 1084–1091 (cit. on p. 12).

20. HESS, Viktor F. Über den Ursprung der durchdringenden Strahlung. *Z. Phys.* 1913, **14**, 610 (cit. on p. 12).

21. CLAY, Jacob. Penetrating radiation. In: *Proceedings of the royal academy of sciences amsterdam*. 1927, vol. 30, pp. 1115–1127 (cit. on p. 12).

22. JOHNSON, Thomas H; STEVENSON, EC. The azimuthal asymmetry of the cosmic radiation at swarthmore. *Journal of the Franklin Institute*. 1933, **216**(2), 276–280 (cit. on p. 12).

23. ALVAREZ, Luis; COMPTON, Arthur H. A positively charged component of cosmic rays. *Physical Review*. 1933, **43**(10), 835 (cit. on p. 12).

24. ROSSI, Bruno. Directional measurements on the cosmic rays near the geomagnetic equator. *Physical Review*. 1934, **45**(3), 212 (cit. on p. 12).

25. GRIEDER, Peter KF. *Cosmic rays at Earth*. Elsevier, 2001 (cit. on pp. 12, 13, 15–17).

26. GRIEDER, Peter KF. Extensive Air Showers: High Energy Phenomena and Astrophysical Aspects-A Tutorial, Reference Manual and Data Book. 2010 (cit. on pp. 12, 18).

27. BERTOLOTTI, Mario. *Celestial messengers: cosmic rays: the story of a scientific adventure*. Springer Science & Business Media, 2012 (cit. on pp. 12, 13, 16, 17).

28. HILLAS, Anthony Michael. *Cosmic Rays: The Commonwealth and International Library: Selected Readings in Physics*. Elsevier, 2013 (cit. on p. 12).

29. LAGAGE, PO; CESARSKY, CJ. Cosmic-ray shock acceleration in the presence of self-excited waves. *Astronomy and Astrophysics*. 1983, **118**, 223–228 (cit. on p. 12).

30. VOELK, Heinrich J; BIERMANN, Peter L. Maximum energy of cosmic-ray particles accelerated by supernova remnant shocks in stellar wind cavities. *The Astrophysical Journal*. 1988, **333**, L65–L68 (cit. on p. 12).

31. BIERMANN, Peter L. Cosmic rays. 1. The cosmic ray spectrum between 10'GeV and 3 10'GeV. *Astronomy and astrophysics*. 1993, **271**, 649 (cit. on p. 12).

32. FERMI, Enrico. On the origin of the cosmic radiation. *Physical review*. 1949, **75**(8), 1169 (cit. on p. 13).

33. BLANDFORD, Roger; EICHLER, David. Particle acceleration at astrophysical shocks: A theory of cosmic ray origin. *Physics Reports*. 1987, **154**(1), 1–75 (cit. on p. 13).

34. LEMOINE, Martin; SIGL, Günter. *Physics and astrophysics of ultra high energy cosmic rays*. Vol. 576. Springer Science & Business Media, 2001 (cit. on p. 13).

35. ENCRENAZ, Therese; BIBRING, Jean-Pierre; BLANC, Michel; BARUCCI, Maria-Antonietta; ROQUES, Francoise; ZARKA, Philippe. *The solar system*. Springer Science & Business Media, 2013 (cit. on p. 13).

36. SIMPSON, JA. Elemental and isotopic composition of the galactic cosmic rays. *Annual Review of Nuclear and Particle Science*. 1983, **33**(1), 323–382 (cit. on p. 13).

37. TANABASHI, Masaharu; HAGIWARA, K; HIKASA, K; NAKAMURA, Katsumasa; SUMINO, Y; TAKAHASHI, F; TANAKA, J; AGASHE, K; AIELLI, G; AMSLER, Claude, et al. Review of particle physics. *Physical Review D*. 2018, **98**(3), 030001 (cit. on p. 14).

38. SLOAN, T; WOLFENDALE, AW. Cosmic rays and climate change over the past 1000 million years. *New Astronomy*. 2013, **25**, 45–49 (cit. on p. 15).

39. REAMES, Donald V. Particle acceleration at the Sun and in the heliosphere. *Space Science Reviews*. 1999, **90**(3), 413–491 (cit. on p. 15).

40. CANE, HV; MCGUIRE, RE v; VON ROSENVINGE, TT. Two classes of solar energetic particle events associated with impulsive and long-duration soft X-ray flares. *The Astrophysical Journal*. 1986, **301**, 448–459 (cit. on p. 15).

41. MASSON, Sophie; ANTIOCHOS, Spiro K; DEVORE, C Rick. A model for the escape of solar-flare-accelerated particles. *The Astrophysical Journal*. 2013, **771**(2), 82 (cit. on p. 15).

42. HANDS, Alex DP; RYDEN, Keith A; MEREDITH, Nigel P; GLAUERT, Sarah A; HORNE, Richard B. Radiation effects on satellites during extreme space weather events. *Space Weather*. 2018, **16**(9), 1216–1226 (cit. on p. 15).

43. HU, Shaowen; KIM, Myung-Hee Y; MCCLELLAN, Gene E; CUCINOTTA, Francis A. Modeling the acute health effects of astronauts from exposure to large solar particle events. *Health physics*. 2009, **96**(4), 465–476 (cit. on p. 15).

44. CANE, Hilary V. Coronal mass ejections and Forbush decreases. *Cosmic rays and Earth*. 2000, 55–77 (cit. on pp. 15, 16).

45. RAGHAV, Anil; SHAIKH, Zubair; BHASKAR, Ankush; DATAR, Gauri; VICHARE, Geeta. Forbush decrease: A new perspective with classification. *Solar Physics*. 2017, **292**(8), 1–14 (cit. on p. 15).

46. VAN ALLEN, James A; FRANK, Louis A. Radiation Around the Earth to a Radial Distance of 107,400 km. *Nature*. 1959, **183**(4659), 430–434 (cit. on p. 16).

47. STÖRMER, Carl. *The polar aurora*. Clarendon Press, 1955 (cit. on p. 16).

48. PFOTZER, Georg. Dreifachkoinzidenzen der Ultrastrahlung aus vertikaler Richtung in der Stratosphäre. *Zeitschrift für Physik*. 1936, **102**(1), 41–58 (cit. on p. 18).

49. CLOSE, Frank; MARTEN, Michael; SUTTON, Christine. *The particle odyssey: A journey to the heart of matter*. Oxford University Press, 2004 (cit. on p. 18).

50. COPELAND, Kyle. CARI-7A: Development and validation. *Radiation Protection Dosimetry*. 2017, **175**(4), 419–431 (cit. on p. 19).

51. SATO, Tatsuhiko. Analytical model for estimating terrestrial cosmic ray fluxes nearly anytime and anywhere in the world: Extension of PARMA/EXPACS. *PloS one*. 2015, **10**(12), e0144679 (cit. on pp. 19, 46).

52. SATO, Tatsuhiko. Analytical model for estimating the zenith angle dependence of terrestrial cosmic ray fluxes. *PloS one*. 2016, **11**(8), e0160390 (cit. on pp. 19, 46).

53. MEIER, Matthias M; HUBIAK, Melina; MATTHIÄ, Daniel; WIRTZ, Michael; REITZ, Günther. Dosimetry at aviation altitudes (2006–2008). *Radiation Protection Dosimetry*. 2009, **136**(4), 251–255 (cit. on pp. 23, 24).

54. SPURNÝ, F; PLOC, O; JADRNÍČKOVÁ, I; TUREK, K; DACHEV, Ts; GELEV, M. Monitoring of onboard aircraft exposure to cosmic radiation: May–December 2005. *Advances in Space Research*. 2007, **40**(11), 1551–1557 (cit. on pp. 23, 24).

55. LEE, Jaejin; NAM, Uk-Won; PYO, Jeonghyun; KIM, Sunghwan; KWON, Yong-Jun; LEE, Jaewon; PARK, Inchun; KIM, Myung-Hee Y; DACHEV, Tsventan P. Short-term variation of cosmic radiation measured by aircraft under constant flight conditions. *Space Weather*. 2015, **13**(11), 797–806 (cit. on pp. 23, 24).

56. JONES, JBL; BENTLEY, RD; HUNTER, R; ILES, RHA; TAYLOR, GC; THOMAS, DJ. Space weather and commercial airlines. *Advances in Space Research*. 2005, **36**(12), 2258–2267 (cit. on pp. 23, 24).

57. FEDERICO, CA; GONÇALEZ, OL; CALDAS, LVE; PAZIANOTTO, MT; DYER, C; CARESANA, Marco; HANDS, A. Radiation measurements onboard aircraft in the South Atlantic region. *Radiation Measurements*. 2015, **82**, 14–20 (cit. on pp. 23, 24).

58. BECK, P; DYER, C; FULLER, N; HANDS, A; LATOCHA, M; ROLLET, S; SPURNÝ, F. Overview of on-board measurements during solar storm periods. *Radiation protection dosimetry*. 2009, **136**(4), 297–303 (cit. on pp. 23, 24).

59. TOBISKA, W Kent; BOUWER, D; SMART, D; SHEA, M; BAILEY, J; DIDKOVSKY, L; JUDGE, K; GARRETT, H; ATWELL, W; GERSEY, B, et al. Global real-time dose measurements using the Automated Radiation Measurements for Aerospace Safety (ARMAS) system. *Space Weather*. 2016, **14**(11), 1053–1080 (cit. on pp. 23, 24, 28).

60. PLOC, Ondrej; AMBROZOVA, Iva; KUBANCAK, Jan; KOVAR, Ivan; DACHEV, Tsvetan P. Publicly available database of measurements with the silicon spectrometer Liulin onboard aircraft. *Radiation measurements*. 2013, **58**, 107–112 (cit. on pp. 23, 24, 27, 28).

61. WISSMANN, F. Long-term measurements of á¸¢*(10) at aviation altitudes in the northern hemisphere. *Radiation protection dosimetry*. 2006, **121**(4), 347–357 (cit. on pp. 23, 24, 32).

62. GREEN, AR; BENNETT, LGI; LEWIS, BJ; KITCHING, F; MCCALL, MJ; DESORMEAUX, M; BUTLER, A. An empirical approach to the measurement of the cosmic radiation field at jet aircraft altitudes. *Advances in Space Research*. 2005, **36**(9), 1618–1626 (cit. on pp. 23, 24, 33–35).

63. LILLHÖK, J; BECK, P; BOTTOLLIER-DEPOIS, JF; LATOCHA, M; LINDBORG, L; ROOS, H; ROTH, J; SCHRAUBE, H; SPURNÝ, F; STEHNO, G, et al. A comparison of ambient dose equivalent meters and dose calculations at constant flight conditions. *Radiation measurements*. 2007, **42**(3), 323–333 (cit. on pp. 23, 24).

64. LATOCHA, M; AUTISCHER, M; BECK, Peter; BOTTOLIER–DEPOIS, JF; ROLLET, S; TROMPIER, F. The results of cosmic radiation in-flight TEPC measurements during the CAATER flight campaign and comparison with simulation. *Radiation protection dosimetry*. 2007, **125**(1-4), 412–415 (cit. on pp. 23, 24).

65. KÁKONA, Martin; ŠTĚPÁN, Václav; AMBROŽOVÁ, Iva; ARSOV, Todor; CHROUST, Jan; KÁKONA, Jakub; KALAPOV, Ivo; KRIST, Pavel; LUŽOVÁ, Martina; NIKOLOVA, Nina, et al. Comparative measurements of mixed radiation fields using Liulin and AIRDOS dosimeters. In: *AIP Conference Proceedings*. AIP Publishing LLC, 2019, vol. 2075, p. 130003. No. 1 (cit. on pp. 23, 24).

66. VUKOVIĆ, B; POJE, M; VARGA, M; RADOLIĆ, V; MIKLAVČIĆ, I; FAJ, D; STANIĆ, D; PLANINIĆ, J. Measurements of neutron radiation in aircraft. *Applied Radiation and Isotopes*. 2010, **68**(12), 2398–2402 (cit. on pp. 23, 24).

67. YASUDA, Hiroshi; YAJIMA, Kazuaki. Verification of cosmic neutron doses in long-haul flights from Japan. *Radiation Measurements*. 2018, **119**, 6–11 (cit. on pp. 23, 24).

68. BEAUJEAN, R; BURMEISTER, S; PETERSEN, F; REITZ, Günther. Radiation exposure measurement onboard civil aircraft. *Radiation protection dosimetry*. 2005, **116**(1-4), 312–315 (cit. on pp. 23, 24, 28, 34, 35).

69. GERSEY, Brad; TOBISKA, W Kent; ATWELL, William; BOUWER, Dave; DIDKOV-SKY, Leonid; JUDGE, Kevin; WIEMAN, Seth; WILKINS, Richard. Beamline and flight comparisons of the ARMAS flight module with the tissue equivalent proportional counter for improving atmospheric radiation monitoring accuracy. *Space Weather*. 2020, **18**(12), e2020SW002599 (cit. on pp. 23, 24).

70. MEIER, Matthias M; TROMPIER, François; AMBROZOVA, Iva; KUBANCAK, Jan; MATTHIÄ, Daniel; PLOC, Ondrej; SANTEN, Nicole; WIRTZ, Michael. CONCORD: comparison of cosmic radiation detectors in the radiation field at aviation altitudes. *Journal of Space Weather and Space Climate*. 2016, **6**, A24 (cit. on pp. 23, 24).

71. BEAUJEAN, R; KOPP, J; REITZ, G. Radiation exposure in civil aircraft. *Radiation protection dosimetry*. 1999, **85**(1-4), 287–290 (cit. on pp. 23, 24).

72. O'SULLIVAN, D; BARTLETT, D; GRILLMAIER, R; HEINRICH, W; LINDBORG, L; SCHRAUBE, H; SILARI, M; TOMMASINO, L; ZHOU, D. Investigation of radiation fields at aircraft altitudes. *Radiation protection dosimetry*. 2000, **92**(1-3), 195–197 (cit. on pp. 23, 24).

73. RITTER, Birgit; MARŠÁLEK, Karel; BERGER, Thomas; BURMEISTER, Sönke; REITZ, Günther; HEBER, Bernd. A small active dosimeter for applications in space. *Nuclear Instruments and Methods in Physics Research Section A: Accelerators, Spectrometers, Detectors and Associated Equipment*. 2014, **748**, 61–69 (cit. on pp. 23, 24).

74. GRANJA, Carlos; POSPISIL, Stanislav. Quantum dosimetry and online visualization of X-ray and charged particle radiation in commercial aircraft at operational flight altitudes with the pixel detector Timepix. *Advances in Space Research*. 2014, **54**(2), 241–251 (cit. on pp. 23, 24, 28, 34, 35).

75. C. TAYLOR, G; D. BENTLEY, R; J. CONROY, T; HUNTER, R; BL JONES, J; POND, A; J. THOMAS, D. The evaluation and use of a portable TEPC system for measuring in-flight exposure to cosmic radiation. *Radiation protection dosimetry*. 2002, **99**(1-4), 435–438 (cit. on pp. 23, 24, 26).

76. TAKADA, Masashi; YAJIMA, Kazuaki; YASUDA, Hiroshi; SATO, Tatsuhiko; NAKAMURA, Takashi. Measurement of atmospheric neutron and photon energy spectra at aviation altitudes using a phoswich-type neutron detector. *Journal of nuclear science and technology*. 2010, **47**(10), 932–944 (cit. on pp. 23, 24, 35).

77. SPURNÝ, F; DACHEV, Ts. Long-term monitoring of the onboard aircraft exposure level with a Si-diode based spectrometer. *Advances in Space Research*. 2003, **32**(1), 53–58 (cit. on pp. 23, 24).

78. BERGER, Thomas; MEIER, Matthias; REITZ, Günther; SCHRIDDE, M. Long-term dose measurements applying a human anthropomorphic phantom onboard an aircraft. *Radiation measurements*. 2008, **43**(2-6), 580–584 (cit. on pp. 23, 24).

79. KUBANČÁK, J; AMBROŽOVÁ, I; PLOC, O; PACHNEROVÁ BRABCOVÁ, K; ŠTĚPÁN, V; UCHIHORI, Y. Measurement of dose equivalent distribution on-board commercial jet aircraft. *Radiation Protection Dosimetry*. 2014, **162**(3), 215–219 (cit. on pp. 23, 24, 28).

80. INTERNATIONAL COMMISSION ON RADIOLOGICAL PROTECTION, 2007 Recommendations of the. ICRP publication 103. *Ann ICRP*. 2007, **37**(2-4), 1–332 (cit. on p. 26).

81. NAM, Uk-Won; PARK, Won-Kee; LEE, Jaejin; PYO, Jeonghyun; MOON, Bong-Kon; LEE, Dae-Hee; KIM, Sunghwan; JIN, Ho; LEE, Seongwhan; KIM, Jungho, et al. Calibration of TEPC for CubeSat experiment to measure space radiation. *Journal of astronomy and space sciences*. 2015, **32**(2), 145–149 (cit. on p. 26).

82. TECHNOLOGY, Far West. *HAWK_ TEPC* [online]. 2021. [visited on 2021-10-12]. Available from: `https://fwt.com/detector/fw-ad1ds.htm` (cit. on p. 26).

83. BADHWAR, GD; CUCINOTTA, FA; BRABY, LA; KONRADI, A. Measurements on the shuttle of the LET spectra of galactic cosmic radiation and comparison with the radiation transport model. *Radiation Research*. 1994, **139**(3), 344–351 (cit. on p. 26).

84. HAYES, Bryan M; CAUSEY, Oliver I; GERSEY, Brad B; BENTON, Eric R. Active Tissue Equivalent Dosimeter: A Tissue Equivalent Proportional Counter flown onboard the International Space Station. *Nuclear Instruments and Methods in Physics Research Section A: Accelerators, Spectrometers, Detectors and Associated Equipment*. 2022, **1028**, 166389 (cit. on p. 26).

85. DACHEV, TP; SEMKOVA, JV; TOMOV, BT; MATVIICHUK, Yu N; DIMITROV, PG; KOLEVA, RT; BANKOV, NG; SHURSHAKOV, VA; BENGHIN, VV; YARMANOVA, EN, et al. Overview of the Liulin type instruments for space radiation measurement and their scientific results. *Life sciences in space research*. 2015, **4**, 92–114 (cit. on p. 26).

86. KÁKONA, M; ŠLEGL, J; KYSELOVÁ, D; SOMMER, M; KÁKONA, J; LUŽOVÁ, M; ŠTĚPÁN, V; PLOC, O; KODAIRA, S; CHROUST, J, et al. AIRDOS—open-source PIN diode airborne dosimeter. *Journal of Instrumentation*. 2021, **16**(03), T03006 (cit. on pp. 26, 29, 32).

87. LLOPART, Xavier; BALLABRIGA, Rafael; CAMPBELL, Michael; TLUSTOS, Lukas; WONG, Winnie. Timepix, a 65k programmable pixel readout chip for arrival time, energy and/or photon counting measurements. *Nuclear Instruments and Methods in Physics Research Section A: Accelerators, Spectrometers, Detectors and Associated Equipment*. 2007, **581**(1-2), 485–494 (cit. on p. 26).

88. FURNELL, Will; SHENOY, Abhishek; FOX, Elliot; HATFIELD, Peter. First results from the LUCID-Timepix spacecraft payload onboard the TechDemoSat-1 satellite in Low Earth Orbit. *Advances in Space Research*. 2019, **63**(5), 1523–1540 (cit. on p. 27).

89. GRANJA, Carlos; JAKUBEK, Jan; POLANSKY, Stepan; ZACH, Vaclav; KRIST, Pavel; CHVATIL, David; STURSA, Jan; SOMMER, Marek; PLOC, Ondrej; KODAIRA, Satoshi, et al. Resolving power of pixel detector Timepix for wide-range electron, proton and ion detection. *Nuclear Instruments and Methods in Physics Research Section A: Accelerators, Spectrometers, Detectors and Associated Equipment*. 2018, **908**, 60–71 (cit. on p. 27).

90. UCHIHORI, Yukio; KITAMURA, Hisashi; FUJITAKA, Kazunobu; DACHEV, Tsvetan P; TOMOV, Borislav T; DIMITROV, Plamen G; MATVIICHUK, Yura. Analysis of the calibration results obtained with Liulin-4J spectrometer–dosimeter on protons and heavy ions. *Radiation Measurements*. 2002, **35**(2), 127–134 (cit. on pp. 27, 29).

91. DACHEV, Tsvetan; HORNECK, Gerda; HÄDER, Donat-Peter; SCHUSTER, Martin; RICHTER, Peter; LEBERT, Michael; DEMETS, Rene. Time profile of cosmic radiation exposure during the EXPOSE-E mission: the R3DE instrument. *Astrobiology*. 2012, **12**(5), 403–411 (cit. on p. 27).

92. SOMMER, Marek; JOHNOVÁ, Kamila; PLOC, Ondřej; BENTON, Eric R; SIHVER, Lembit. Monte Carlo simulation of semiconductor-based detector in mixed radiation field in the atmosphere. *Life Sciences in Space Research*. 2022 (cit. on pp. 27–29, 34, 35, 46, 47, 61, 100).

93. SAKAGUCHI, T; DOKE, T; HASEBE, N; HAYASHI, T; KASHIWAGI, T; KIKUCHI, J; KONO, S; NAGAOKA, S; NAKANO, T; TAKAGI, T, et al. LET distribution measurement with a new real-time radiation monitoring device-III onboard the Space Shuttle STS-84. *Nuclear Instruments and Methods in Physics Research Section A: Accelerators, Spectrometers, Detectors and Associated Equipment*. 1999, **437**(1), 75–87 (cit. on p. 28).

94. BEAUJEAN, R; KOPP, J; BURMEISTER, S; PETERSEN, F; REITZ, G. Dosimetry inside MIR station using a silicon detector telescope (DOSTEL). *Radiation measurements*. 2002, **35**(5), 433–438 (cit. on p. 28).

95. LABRENZ, Johannes; BURMEISTER, Soenke; BERGER, Thomas; HEBER, Bernd; REITZ, Guenther. Matroshka DOSTEL measurements onboard the International Space Station (ISS). *Journal of Space Weather and Space Climate*. 2015, **5**, A38 (cit. on p. 28).

96. PLOC, Ondřej; SOMMER, Marek; KÁKONA, Martin; KUBANČÁK, Ján; PEKSOVÁ, Dagmar; MOLOKANOV, Alexander; SIHVER, Lembit. Intercomparison of LET spectra measured with Timepix and TEPC in reference radiation field CERF. In: *2018 IEEE Aerospace Conference*. IEEE, 2018, pp. 1–11 (cit. on pp. 28, 34, 35).

97. WISSMANN, F; BURMEISTER, S; DÖNSDORF, E; HEBER, B; HUBIAK, M; KLAGES, T; LANGNER, F; MÖLLER, T; MEIER, M. Field calibration of dosemeters used for routine measurements at flight altitudes. *Radiation protection dosimetry*. 2010, **140**(4), 319–325 (cit. on pp. 28, 32).

98. BENTON, ER; BENTON, EV; FRANK, AL. Conversion between different forms of LET. *Radiation measurements*. 2010, **45**(8), 957–959 (cit. on p. 28).

99. JAKUBEK, Jan. Precise energy calibration of pixel detector working in time-over-threshold mode. *Nuclear Instruments and Methods in Physics Research Section A: Accelerators, Spectrometers, Detectors and Associated Equipment*. 2011, **633**, S262–S266 (cit. on p. 30).

100. KROUPA, M; CAMPBELL-RICKETTS, T; BAHADORI, A; EMPL, A. Techniques for precise energy calibration of particle pixel detectors. *Review of Scientific Instruments*. 2017, **88**(3), 033301 (cit. on p. 30).

101. GEORGE, SP; KROUPA, M; WHEELER, S; KODAIRA, S; KITAMURA, H; TLUSTOS, L; CAMPBELL-RICKETTS, T; STOFFLE, NN; SEMONES, E; PINSKY, L. Very high energy calibration of silicon Timepix detectors. *Journal of Instrumentation*. 2018, **13**(11), P11014 (cit. on p. 30).

102. HOLIK, M; AHMADOV, G; BROULIM, J; ZICH, J; BERIKOV, D; MORA, Y; KOPATCH, Yu; NURUYEV, S; ABBASZADA, N; ZHUMADILOV, K. Alpha calibration of the Timepix pixel detector exploiting energy information gained from a common electrode signal. *Journal of Instrumentation*. 2019, **14**(06), C06022 (cit. on p. 30).

103. SOMMER, Marek; GRANJA, Carlos; KODAIRA, Satoshi; PLOC, Ondřej. High-energy per-pixel calibration of timepix pixel detector with laboratory alpha source. *Nuclear Instruments and Methods in Physics Research Section A: Accelerators, Spectrometers, Detectors and Associated Equipment*. 2022, **1022**, 165957 (cit. on p. 30).

104. KANANEN, H; TANSKANEN, PJ; GENTILE, LC; SHEA, MA; SMART, DF. A quarter of a century of relativistic solar cosmic ray events recorded by the Oulu neutron monitor. In: *International Cosmic Ray Conference*. 1991, vol. 3, p. 145 (cit. on p. 32).

105. WISSMANN, F; REGINATTO, M; MÖLLER, T. The ambient dose equivalent at flight altitudes: a fit to a large set of data using a Bayesian approach. *Journal of Radiological Protection*. 2010, **30**(3), 513 (cit. on p. 32).

106. WISSMANN, F; BURDA, O; KHURANA, S; KLAGES, T; LANGNER, F. Dosimetry of secondary cosmic radiation up to an altitude of 30 km. *Radiation protection dosimetry*. 2014, **161**(1-4), 299–302 (cit. on pp. 32, 33).

107. MITAROFF, Angela; SILARI, Marco. The CERN-EU high-energy reference field (CERF) facility for dosimetry at commercial flight altitudes and in space. *Radiation Protection Dosimetry*. 2002, **102**(1), 7–22 (cit. on p. 34).

108. SPURNÝ, František; DASCHEV, T. On board aircrew dosimetry with a semiconductor spectrometer. *Radiation protection dosimetry*. 2002, **100**(1-4), 525–528 (cit. on p. 34).

109. PLOC, O; PACHNEROVA BRABCOVA, K; SPURNÝ, F; MALUŠEK, A; DACHEV, Ts. Use of energy deposition spectrometer Liulin for individual monitoring of aircrew. *Radiation Protection Dosimetry*. 2011, **144**(1-4), 611–614 (cit. on p. 34).

110. MUSÍLEK, Ladislav; ŠEDA, Josef; TROUSIL, Jaroslav. *Dozimetrie ionizujího záření: (integrující metody)*. Praha: Ediční středisko ČVUT, 1992. ISBN 80-01-00812-6 (cit. on p. 34).

111. CLARKE, RH; FRY, FA; STATHER, JW; WEBB, G AM. 1990 recommendations of the International Commission on Radiological Protection. *Documents of the NRPB (National Radiological Protection Board);(United Kingdom)*. 1993, **4**(1) (cit. on p. 34).

112. HOANG, S; PINSKY, L; VILALTA, R; JAKUBEK, J. LET estimation of heavy ion particles based on a timepix-based Si detector. In: *Journal of Physics: Conference Series*. IOP Publishing, 2012, vol. 396, p. 022023. No. 2 (cit. on p. 35).

113. NABHA, Racell; VAN HOEY, Olivier; GRANJA, Carlos; PARISI, Alessio; DE SAINT-HUBERT, M; STRUELENS, Lara; OANCEA, Cristina; STERPIN, Edmond; ZACH, V; STURSA, Jan, et al. A novel method to assess the incident angle and the LET of protons using a compact single-layer Timepix detector. *Radiation Physics and Chemistry*. 2022, **199**, 110349 (cit. on p. 35).

114. BIRKS, John Betteley. *The theory and practice of scintillation counting: International series of monographs in electronics and instrumentation*. Vol. 27. Elsevier, 2013 (cit. on p. 37).

115. BROOKS, FD. Development of organic scintillators. *Nuclear Instruments and Methods*. 1979, **162**(1-3), 477–505 (cit. on p. 37).

116. WOOLF, Richard S; HUTCHESON, Anthony L; GWON, Chul; PHLIPS, Bernard F; WULF, Eric A. Comparing the response of PSD-capable plastic scintillator to standard liquid scintillator. *Nuclear Instruments and Methods in Physics Research Section A: Accelerators, Spectrometers, Detectors and Associated Equipment*. 2015, **784**, 80–87 (cit. on p. 38).

117. TECHNOLOGY, Eljen. *EJ-276* [online]. 2022. [visited on 2022-11-22]. Available from: `https://eljentechnology.com/products/plastic-scintillators/ej-276` (cit. on p. 38).

118. ONSEMI. *MicroFC-60035* [online]. 2022. [visited on 2022-11-22]. Available from: `https://www.onsemi.com/download/data-sheet/pdf/microc-series-d.pdf` (cit. on p. 38).

119. CORSI, F; FORESTA, M; MARZOCCA, C; MATARRESE, G; DEL GUERRA, Alberto. Current-mode front-end electronics for silicon photo-multiplier detectors. In: *2007 2nd International Workshop on Advances in Sensors and Interface*. IEEE, 2007, pp. 1–6 (cit. on p. 40).

120. LIU, Tianyi; CAI, Zhicheng; ANDERS, Jens; ORTMANNS, Maurits. A bootstrap transimpedance amplifier for high speed optical transcutaneous wireless links. In: *2014 10th Conference on Ph. D. Research in Microelectronics and Electronics (PRIME)*. IEEE, 2014, pp. 1–4 (cit. on p. 40).

121. MARANO, D; BELLUSO, M; BONANNO, G; BILLOTTA, S; GRILLO, A; GAROZZO, S; ROMEO, G; CATALANO, O; LA ROSA, G; SOTTILE, G, et al. Silicon photomultipliers electrical model extensive analytical analysis. *IEEE Transactions on Nuclear Science*. 2013, **61**(1), 23–34 (cit. on p. 40).

122. VILLA, Federica; ZOU, Yu; DALLA MORA, Alberto; TOSI, Alberto; ZAPPA, Franco. SPICE electrical models and simulations of silicon photomultipliers. *IEEE Transactions on Nuclear Science*. 2015, **62**(5), 1950–1960 (cit. on p. 40).

123. SOMMER, Marek; KRIST, Pavel; KÁKONA, Martin; PLOC, Ondřej. Novel Model for Analysis and Optimization of Silicon Photomultiplier-Based Scintillation Systems. *IEEE Transactions on Nuclear Science*. 2021, **68**(12), 2771–2778 (cit. on pp. 41, 66, 100).

124. INSTRUMENTS, Texas. *OPA656* [online]. 2022. [visited on 2022-11-22]. Available from: `https://www.ti.com/product/OPA656` (cit. on p. 41).

125. DEVICES, Analog. *AD8039* [online]. 2022. [visited on 2022-11-22]. Available from: `https://www.analog.com/en/products/ad8039.html` (cit. on p. 41).

126. POWER, RECOM. *RB-3.315D* [online]. 2022. [visited on 2022-11-22]. Available from: `https://g.recomcdn.com/media/Datasheet/pdf/.fcqn_xzW/.tdcfb53000cb64b668e40/Datasheet-0/RB.pdf` (cit. on p. 43).

127. INSTRUMENTS, Texas. *TPS7A3001* [online]. 2022. [visited on 2022-11-22]. Available from: `https://www.ti.com/product/TPS7A3001-EP` (cit. on p. 43).

128. PITAYA, Red. *RED PITAYA* [online]. 2022. [visited on 2022-11-22]. Available from: `https://redpitaya.com/stemlab-125-10/` (cit. on p. 44).

129. GOORLEY, John T; JAMES, Michael R; BOOTH, Thomas E; BROWN, Forrest B; BULL, Jeffrey S; COX, Lawrence J; DURKEE JR, Joe W; ELSON, Jay S; FENSIN, Michael Lorne; FORSTER III, Robert A, et al. *Initial MCNP6 release overview-MCNP6 version 1.0*. 2013. Tech. rep. Los Alamos National Lab.(LANL), Los Alamos, NM (United States) (cit. on p. 46).

130. LIAO, Can; YANG, Haori. Pulse shape discrimination using EJ-299-33 plastic scintillator coupled with a Silicon Photomultiplier array. *Nuclear Instruments and Methods in Physics Research Section A: Accelerators, Spectrometers, Detectors and Associated Equipment*. 2015, **789**, 150–157 (cit. on p. 50).

131. BAI, Huaiyong; WANG, Zhimin; ZHANG, Luyu; LU, Yi; JIANG, Haoyu; CHEN, Jinxiang; ZHANG, Guohui. Calibration of an EJ309 liquid scintillator using an AmBe neutron source. *Nuclear Instruments and Methods in Physics Research Section A: Accelerators, Spectrometers, Detectors and Associated Equipment*. 2017, **863**, 47–54 (cit. on pp. 51, 89, 90).

132. SAFARI, MJ; DAVANI, F Abbasi; AFARIDEH, H. Differentiation method for localization of Compton edge in organic scintillation detectors. *arXiv preprint arXiv:1610.09185*. 2016 (cit. on pp. 51, 90).

133. JOO, HW; PARK, HS; KIM, JH; LEE, JY; KIM, SK; KIM, YD; LEE, Hyun Su; KIM, Sung Hyun. Quenching factor measurement for NaI (Tl) scintillation crystal. *Astroparticle Physics*. 2019, **108**, 50–56 (cit. on pp. 55, 91).

134. REICHHART, L; AKIMOV, D Yu; ARAÚJO, HM; BARNES, EJ; BELOV, VA; BURENKOV, AA; CHEPEL, V; CURRIE, A; DEVIVEIROS, L; EDWARDS, B, et al. Quenching factor for low-energy nuclear recoils in a plastic scintillator. *Physical Review C*. 2012, **85**(6), 065801 (cit. on pp. 55, 91).

135. CHAGANI, H; MAJEWSKI, P; DAW, EJ; KUDRYAVTSEV, VA; SPOONER, NJC. Measurement of the quenching factor of Na recoils in NaI (Tl). *Journal of Instrumentation*. 2008, **3**(06), P06003 (cit. on pp. 55, 91).

136. WILLIAMSON, Jeffrey F; DEMPSEY, JF; KIROV, AS; MONROE, JI; BINNS, WR; HEDTJÄRN, Håkan. Plastic scintillator response to low-energy photons. *Physics in Medicine & Biology*. 1999, **44**(4), 857 (cit. on pp. 55, 91).

137. KORNILOV, NV; FABRY, I; OBERSTEDT, S; HAMBSCH, F-J. Total characterization of neutron detectors with a 252Cf source and a new light output determination. *Nuclear Instruments and Methods in Physics Research Section A: Accelerators, Spectrometers, Detectors and Associated Equipment*. 2009, **599**(2-3), 226–233 (cit. on p. 55).

138. ENQVIST, Andreas; LAWRENCE, Christopher C; WIEGER, Brian M; POZZI, Sara A; MASSEY, Thomas N. Neutron light output response and resolution functions in EJ-309 liquid scintillation detectors. *Nuclear Instruments and Methods in Physics Research Section A: Accelerators, Spectrometers, Detectors and Associated Equipment*. 2013, **715**, 79–86 (cit. on pp. 55, 91).

139. RYABEVA, EV; URUPA, IV; LUPAR, EE; KADILIN, VV; SKOTNIKOVA, AV; KOKOREV, YA; IBRAGIMOV, RF. Calibration of EJ-276 plastic scintillator for neutron–gamma pulse shape discrimination experiments. *Nuclear Instruments and Methods in Physics Research Section A: Accelerators, Spectrometers, Detectors and Associated Equipment*. 2021, **1010**, 165495 (cit. on p. 55).

140. WILSON, Charles TR. The acceleration of β-particles in strong electric fields such as those of thunderclouds. In: *Mathematical Proceedings of the Cambridge Philosophical Society*. Cambridge University Press, 1925, vol. 22, pp. 534–538. No. 4 (cit. on p. 67).

141. GUREVICH, AV; MILIKH, GM; ROUSSEL-DUPRE, R. Runaway electron mechanism of air breakdown and preconditioning during a thunderstorm. *Physics Letters A*. 1992, **165**(5-6), 463–468 (cit. on p. 67).

142. DWYER, Joseph R; BABICH, Leonid P. Low-energy electron production by relativistic runaway electron avalanches in air. *Journal of Geophysical Research: Space Physics*. 2011, **116**(A9) (cit. on p. 67).

143. DWYER, Joseph R; SMITH, David M; CUMMER, Steven A. High-energy atmospheric physics: Terrestrial gamma-ray flashes and related phenomena. *Space Science Reviews*. 2012, **173**(1), 133–196 (cit. on pp. 67, 69).

144. SKELTVED, Alexander Broberg; ØSTGAARD, Nikolai; CARLSON, Brant; GJESTELAND, Thomas; CELESTIN, Sebastien. Modeling the relativistic runaway electron avalanche and the feedback mechanism with GEANT4. *Journal of Geophysical Research: Space Physics*. 2014, **119**(11), 9174–9191 (cit. on p. 67).

145. BABICH, Leonid Petrovich. Relativistic runaway electron avalanche. *Physics-Uspekhi*. 2020, **63**(12), 1188 (cit. on p. 67).

146. CHILINGARIAN, Ashot; MAILYAN, Bagrat; VANYAN, Levon. Recovering of the energy spectra of electrons and gamma rays coming from the thunderclouds. *Atmospheric research*. 2012, **114**, 1–16 (cit. on p. 67).

147. CHILINGARIAN, Ashot; HOVSEPYAN, Gagik; HOVHANNISYAN, Armen. Particle bursts from thunderclouds: Natural particle accelerators above our heads. *Physical review D*. 2011, **83**(6), 062001 (cit. on p. 67).

148. CHILINGARIAN, A; CHILINGARYAN, S; REYMERS, A. Atmospheric discharges and particle fluxes. *Journal of Geophysical Research: Space Physics*. 2015, **120**(7), 5845–5853 (cit. on p. 67).

149. CHILINGARIAN, A; HOVSEPYAN, G; KOZLINER, L. Extensive air showers, lightning, and thunderstorm ground enhancements. *Astroparticle Physics*. 2016, **82**, 21–35 (cit. on p. 67).

150. CHILINGARIAN, A; SOGHOMONYAN, S; KHANIKYANC, Y; POKHSRARYAN, D. On the origin of particle fluxes from thunderclouds. *Astroparticle Physics*. 2019, **105**, 54–62 (cit. on pp. 67, 72).

151. TSUCHIYA, H; ENOTO, T; YAMADA, S; YUASA, T; NAKAZAWA, K; KITAGUCHI, T; KAWAHARADA, M; KOKUBUN, M; KATO, H; OKANO, M, et al. Long-duration γ ray emissions from 2007 and 2008 winter thunderstorms. *Journal of Geophysical Research: Atmospheres*. 2011, **116**(D9) (cit. on p. 67).

152. BRUNETTI, Michele; CECCHINI, Stefano; GALLI, Menotti; GIOVANNINI, Giovanni; PAGLIARIN, Andrea. Gamma-ray bursts of atmospheric origin in the MeV energy range. *Geophysical Research Letters*. 2000, **27**(11), 1599–1602 (cit. on p. 67).

153. CHUM, J; LANGER, R; BAŠE, J; KOLLÁRIK, M; STRHÁRSKÝ, I; DIENDORFER, G; RUSZ, J. Significant enhancements of secondary cosmic rays and electric field at the high mountain peak of Lomnický Štít in High Tatras during thunderstorms. *Earth, Planets and Space*. 2020, **72**(1), 1–20 (cit. on pp. 67, 72, 79).

154. ŠLEGL, J; MINÁŘOVÁ, J; KUČA, P; KOLMAŠOVÁ, I; SANTOLÍK, O; SOKOL, Z; REITZ, G; AMBROŽOVÁ, I; PLOC, O. Response of the Czech RMN network to thunderstorm activity. *Radiation Protection Dosimetry*. 2019, **186**(2-3), 215–218 (cit. on p. 67).

155. KOLMAŠOVÁ, Ivana; SANTOLÍK, Ondřej; ŠLEGL, Jakub; POPOVÁ, Jana; SOKOL, Zbyněk; ZACHAROV, Petr; PLOC, Ondřej; DIENDORFER, Gerhard; LANGER, Ronald; LÁN, Radek, et al. Continental Thunderstorm Ground Enhancement observed at an exceptionally low altitude. *Atmospheric Chemistry and Physics Discussions*. 2022, 1–21 (cit. on p. 67).

156. CUMMER, Steven A; LU, Gaopeng; BRIGGS, Michael S; CONNAUGHTON, Valerie; XIONG, Shaolin; FISHMAN, Gerald J; DWYER, Joseph R. The lightning-TGF relationship on microsecond timescales. *Geophysical Research Letters*. 2011, **38**(14) (cit. on p. 68).

157. CUMMER, Steven A; LYU, Fanchao; BRIGGS, Michael S; FITZPATRICK, Gerard; ROBERTS, Oliver J; DWYER, Joseph R. Lightning leader altitude progression in terrestrial gamma-ray flashes. *Geophysical Research Letters*. 2015, **42**(18), 7792–7798 (cit. on p. 68).

158. ØSTGAARD, Nikolai; CUMMER, SA; MEZENTSEV, Andrey; LUQUE, Alejandro; DWYER, J; NEUBERT, Torsten; REGLERO, Victor; MARISALDI, Martino; KOCHKIN, Pavlo; SARRIA, D, et al. Simultaneous observations of EIP, TGF, Elve, and optical lightning. *Journal of Geophysical Research: Atmospheres*. 2021, **126**(11), e2020JD033921 (cit. on p. 68).

159. MARISALDI, M; FUSCHINO, F; LABANTI, C; GALLI, M; LONGO, Francesco; DEL MONTE, E; BARBIELLINI, G; TAVANI, M; GIULIANI, A; MORETTI, Elena, et al. Detection of terrestrial gamma ray flashes up to 40 MeV by the AGILE satellite. *Journal of Geophysical Research: Space Physics*. 2010, **115**(A3) (cit. on p. 68).

160. MARISALDI, M; FUSCHINO, F; TAVANI, M; DIETRICH, S; PRICE, C; GALLI, M; PITTORI, Carlotta; VERRECCHIA, Francesco; MEREGHETTI, Sandro; CATTANEO, PW, et al. Properties of terrestrial gamma ray flashes detected by AGILE MCAL below 30 MeV. *Journal of Geophysical Research: Space Physics*. 2014, **119**(2), 1337–1355 (cit. on p. 68).

161. MAIORANA, Carolina; MARISALDI, Martino; LINDANGER, Anders; ØSTGAARD, Nikolai; URSI, Alessandro; SARRIA, David; GALLI, M; LABANTI, C; TAVANI, Marco; PITTORI, C, et al. The 3rd AGILE terrestrial gamma-ray flashes catalog. Part II: Optimized selection criteria and characteristics of the new sample. *Journal of Geophysical Research: Atmospheres*. 2020, **125**(11), e2019JD031986 (cit. on p. 68).

162. BRIGGS, MS; FISHMAN, GJ; CONNAUGHTON, V; BHAT, PN; PACIESAS, WS; PREECE, RD; WILSON-HODGE, C; CHAPLIN, VL; KIPPEN, RM; VON KIENLIN, A, et al. First results on terrestrial gamma ray flashes from the Fermi Gamma-ray Burst Monitor. *Journal of Geophysical Research: Space Physics*. 2010, **115**(A7) (cit. on p. 68).

163. BRIGGS, Michael; CONNAUGHTON, Valerie; STANBRO, Matthew; ZHANG, Binbin; BHAT, Narayana; FISHMAN, Gerald; ROBERTS, Oliver; FITZPATRICK, Gerard; MCBREEN, Shelia; GROVE, Eric, et al. The first Fermi gamma-ray burst monitor (GBM) terrestrial gamma-ray flash (TGF) catalog. In: *EGU General Assembly Conference Abstracts*. 2015, p. 9961 (cit. on p. 68).

164. NEUBERT, Torsten; ØSTGAARD, Nikolai; REGLERO, Victor; BLANC, Elisabeth; CHANRION, Olivier; OXBORROW, Carol Anne; ORR, Astrid; TACCONI, Matteo; HARTNACK, Ole; BHANDERI, Dan DV. The ASIM mission on the international space station. *Space Science Reviews*. 2019, **215**(2), 1–17 (cit. on p. 68).

165. DWYER, Joseph R; GREFENSTETTE, Brian W; SMITH, David M. High-energy electron beams launched into space by thunderstorms. *Geophysical Research Letters*. 2008, **35**(2) (cit. on p. 68).

166. MAIORANA, Carolina; MARISALDI, M; FÜLLEKRUG, Martin; SOULA, Serge; LAPIERRE, J; MEZENTSEV, Andrey; SKEIE, CA; HEUMESSER, M; CHANRION, Olivier; ØSTGAARD, N, et al. Observation of terrestrial gamma-ray flashes at mid latitude. *Journal of Geophysical Research: Atmospheres*. 2021, **126**(18), e2020JD034432 (cit. on p. 68).

167. BOWERS, GS; SMITH, DM; KELLEY, NA; MARTINEZ-MCKINNEY, GF; CUMMER, SA; DWYER, JR; HECKMAN, S; HOLZWORTH, RH; MARKS, F; REASOR, P, et al. A terrestrial gamma-ray flash inside the eyewall of hurricane Patricia. *Journal of Geophysical Research: Atmospheres*. 2018, **123**(10), 4977–4987 (cit. on p. 68).

168. DWYER, JR; SCHAAL, MM; CRAMER, E; ARABSHAHI, S; LIU, N; RASSOUL, HK; HILL, JD; JORDAN, DM; UMAN, MA. Observation of a gamma-ray flash at ground level in association with a cloud-to-ground lightning return stroke. *Journal of Geophysical Research: Space Physics*. 2012, **117**(A10) (cit. on p. 69).

169. TRAN, MD; RAKOV, VA; MALLICK, Sh; DWYER, JR; NAG, A; HECKMAN, S. A terrestrial gamma-ray flash recorded at the Lightning Observatory in Gainesville, Florida. *Journal of Atmospheric and Solar-Terrestrial Physics*. 2015, **136**, 86–93 (cit. on p. 69).

170. HARE, BM; UMAN, MA; DWYER, JR; JORDAN, DM; BIGGERSTAFF, MI; CAICEDO, JA; CARVALHO, FL; WILKES, RA; KOTOVSKY, DA; GAMEROTA, WR, et al. Ground-level observation of a terrestrial gamma ray flash initiated by a triggered lightning. *Journal of Geophysical Research: Atmospheres*. 2016, **121**(11), 6511–6533 (cit. on p. 69).

171. SMITH, DM; BOWERS, GS; KAMOGAWA, M; WANG, D; USHIO, T; ORTBERG, J; DWYER, JR; STOCK, M. Characterizing upward lightning with and without a terrestrial gamma ray flash. *Journal of Geophysical Research: Atmospheres*. 2018, **123**(20), 11–321 (cit. on p. 69).

172. ABBASI, RU; ABU-ZAYYAD, T; ALLEN, M; BARCIKOWSKI, E; BELZ, JW; BERGMAN, DR; BLAKE, SA; BYRNE, M; CADY, R; CHEON, BG, et al. Gamma ray showers observed at ground level in coincidence with downward lightning leaders. *Journal of Geophysical Research: Atmospheres*. 2018, **123**(13), 6864–6879 (cit. on p. 69).

173. BELZ, JW; KREHBIEL, PR; REMINGTON, J; STANLEY, MA; ABBASI, RU; LEVON, R; RISON, W; RODEHEFFER, D; ABU-ZAYYAD, T; ALLEN, M, et al. Observations of the origin of downward terrestrial gamma-ray flashes. *Journal of Geophysical Research: Atmospheres*. 2020, **125**(23), e2019JD031940 (cit. on pp. 69, 70).

174. TILLES, Julia N; KREHBIEL, Paul R; STANLEY, Mark A; RISON, William; LIU, Ningyu; LYU, Fanchao; CUMMER, Steven A; DWYER, Joseph R; SENAY, Seda; EDENS, Harald, et al. Radio interferometer observations of an energetic in-cloud pulse reveal large currents generated by relativistic discharges. *Journal of Geophysical Research: Atmospheres*. 2020, **125**(20), e2020JD032603 (cit. on p. 69).

175. ABBASI, RU; BELZ, JW; SABA, MMF; KREHBIEL, PR; REMINGTON, J; STANLEY, MA; SILVA, DR da; RISON, W; RODEHEFFER, Dan; KIEU, N, et al. First High-speed Camera Observations of the Optical Counterpart of a Terrestrial Gamma-ray Flash. *arXiv preprint arXiv:2205.05115*. 2022 (cit. on p. 69).

176. LYU, Fanchao; CUMMER, Steven A; BRIGGS, Michael; MARISALDI, Martino; BLAKESLEE, Richard J; BRUNING, Eric; WILSON, Jennifer G; RISON, William; KREHBIEL, Paul; LU, Gaopeng, et al. Ground detection of terrestrial gamma ray flashes from distant radio signals. *Geophysical Research Letters*. 2016, **43**(16), 8728–8734 (cit. on p. 70).

177. LYU, Fanchao; CUMMER, Steven A; KREHBIEL, Paul R; RISON, William; BRIGGS, Michael S; CRAMER, Eric; ROBERTS, Oliver; STANBRO, Matthew. Very high frequency radio emissions associated with the production of terrestrial gamma-ray flashes. *Geophysical Research Letters*. 2018, **45**(4), 2097–2105 (cit. on p. 70).

178. CUMMER, Steven A; LYU, Fanchao; BRIGGS, Michael S; CRAMER, Eric; STANBRO, Matthew; ROBERTS, Oliver; SMITH, David Miles. The connection between terrestrial gamma-ray flashes and energetic in-cloud lightning pulses. In: *AGU Fall Meeting Abstracts*. 2017, vol. 2017, AE33B–2547 (cit. on p. 70).

179. SHAH, GN; RAZDAN, H; BHAT, CL; ALI, QM. Neutron generation in lightning bolts. *Nature*. 1985, **313**(6005), 773–775 (cit. on p. 70).

180. SHYAM, A; KAUSHIK, TC. Observation of neutron bursts associated with atmospheric lightning discharge. *Journal of Geophysical Research: Space Physics*. 1999, **104**(A4), 6867–6869 (cit. on p. 70).

181. MARTIN, Inácio M; ALVES, Mauro A. Observation of a possible neutron burst associated with a lightning discharge? *Journal of Geophysical Research: Space Physics*. 2010, **115**(A2) (cit. on pp. 70, 71).

182. CHILINGARIAN, Ashot; BOSTANJYAN, Nikolaj; VANYAN, L. Neutron bursts associated with thunderstorms. *Physical review D*. 2012, **85**(8), 085017 (cit. on p. 70).

183. CHILINGARIAN, A; MELKUMYAN, L; HOVSEPYAN, G; REYMERS, A. The response function of the Aragats solar neutron telescope. *Nuclear Instruments and Methods in Physics Research Section A: Accelerators, Spectrometers, Detectors and Associated Equipment*. 2007, **574**(2), 255–263 (cit. on p. 70).

184. CHILINGARIAN, A; REYMERS, A. Investigations of the response of hybrid particle detectors for the Space Environmental Viewing and Analysis Network (SEVAN). In: *Annales Geophysicae*. Copernicus GmbH, 2008, vol. 26, pp. 249–257. No. 2 (cit. on p. 70).

185. CHILINGARIAN, A; HOVSEPYAN, G; ARAKELYAN, K; CHILINGARYAN, S; DANIELYAN, V; AVAKYAN, K; YEGHIKYAN, A; REYMERS, A; TSERUNYAN, S. Space environmental viewing and analysis network (SEVAN). *Earth, Moon, and Planets*. 2009, **104**(1), 195–210 (cit. on p. 70).

186. TSUCHIYA, H; HIBINO, K; KAWATA, K; HOTTA, N; TATEYAMA, N; OHNISHI, M; TAKITA, M; CHEN, D; HUANG, J; MIYASAKA, M, et al. Observation of thundercloud-related gamma rays and neutrons in Tibet. *Physical Review D*. 2012, **85**(9), 092006 (cit. on p. 70).

187. CHILINGARIAN, A; BOSTANJYAN, N; KARAPETYAN, T; VANYAN, L. Remarks on recent results on neutron production during thunderstorms. *Physical Review D*. 2012, **86**(9), 093017 (cit. on p. 70).

188. STARODUBTSEV, Sergei Anatol'evich; KOZLOV, Vladimir Il'ich; TOROPOV, AA; MULLAYAROV, VA; GRIGOR'EV, Vladislav Georgievich; MOISEEV, AV. First experimental observations of neutron bursts under thunderstorm clouds near sea level. *JETP letters*. 2012, **96**(3), 188–191 (cit. on p. 72).

189. GUREVICH, AV; ANTONOVA, VP; CHUBENKO, AP; KARASHTIN, AN; MITKO, GG; PTITSYN, MO; RYABOV, VA; SHEPETOV, AL; SHLYUGAEV, Yu V; VILDANOVA, LI, et al. Strong flux of low-energy neutrons produced by thunderstorms. *Physical review letters*. 2012, **108**(12), 125001 (cit. on p. 72).

190. GUREVICH, AV; ANTONOVA, VP; CHUBENKO, AP; KARASHTIN, AN; KRYAKUNOVA, ON; LUTSENKO, V Yu; MITKO, GG; PISKAL, VV; PTITSYN, MO; RYABOV, VA, et al. The time structure of neutron emission during atmospheric discharge. *Atmospheric Research*. 2015, **164**, 339–346 (cit. on p. 72).

191. GUREVICH, AV; ALMENOVA, AM; ANTONOVA, VP; CHUBENKO, AP; KARASHTIN, AN; KRYAKUNOVA, ON; LUTSENKO, V Yu; MITKO, GG; PTITSYN, MO; PISCAL, VV, et al. Observations of high-energy radiation during thunderstorms at Tien-Shan. *Physical Review D*. 2016, **94**(2), 023003 (cit. on pp. 72, 73).

192. KURODA, Y; OGURI, S; KATO, Y; NAKATA, R; INOUE, Y; ITO, C; MINOWA, M. Observation of gamma ray bursts at ground level under the thunderclouds. *Physics Letters B*. 2016, **758**, 286–291 (cit. on p. 72).

193. OGURI, S; KURODA, Y; KATO, Y; NAKATA, R; INOUE, Y; ITO, C; MINOWA, M. Reactor antineutrino monitoring with a plastic scintillator array as a new safeguards method. *Nuclear Instruments and Methods in Physics Research Section A: Accelerators, Spectrometers, Detectors and Associated Equipment*. 2014, **757**, 33–39 (cit. on p. 72).

194. BOWERS, Gregory S; SMITH, David Miles; MARTINEZ-MCKINNEY, GF; KAMOGAWA, M; CUMMER, SA; DWYER, JR; WANG, D; STOCK, M; KAWASAKI, Z. Gamma ray signatures of neutrons from a terrestrial gamma ray flash. *Geophysical Research Letters*. 2017, **44**(19), 10–063 (cit. on pp. 74, 75, 80).

195. WADA, Yuuki; NAKAZAWA, Kazuhiro; ENOTO, Teruaki; FURUTA, Yoshihiro; YUASA, Takayuki; MAKISHIMA, Kazuo; TSUCHIYA, Harufumi. Photoneutron detection in lightning by gadolinium orthosilicate scintillators. *Physical Review D*. 2020, **101**(10), 102007 (cit. on p. 74).

196. ENOTO, Teruaki; WADA, Yuuki; FURUTA, Yoshihiro; NAKAZAWA, Kazuhiro; YUASA, Takayuki; OKUDA, Kazufumi; MAKISHIMA, Kazuo; SATO, Mitsuteru; SATO, Yousuke; NAKANO, Toshio, et al. Photonuclear reactions triggered by lightning discharge. *Nature*. 2017, **551**(7681), 481–484 (cit. on pp. 74, 76).

197. BABICH, Leonid Petrovich. Thunderstorm neutrons. *Physics-Uspekhi*. 2019, **62**(10), 976 (cit. on p. 74).

198. DINIZ, G; RUTJES, C; EBERT, U; FERREIRA, IS; SÃO SABBAS, EFMT. Modeling neutron emissions in high energy atmospheric phenomena. *Journal of Geophysical Research: Atmospheres*. 2018, **123**(22), 12–726 (cit. on p. 77).

199. WADA, Y; ENOTO, T; NAKAZAWA, K; ODAKA, H; FURUTA, Y; TSUCHIYA, H. Photonuclear reactions in lightning: 1. Verification and modeling of reaction and propagation processes. *Journal of Geophysical Research: Atmospheres*. 2020, **125**(20), e2020JD033193 (cit. on pp. 77, 78, 80).

200. WADA, Y; ENOTO, T; NAKAZAWA, K; YUASA, T; FURUTA, Y; ODAKA, H; MAKISHIMA, K; TSUCHIYA, H. Photonuclear reactions in lightning: 2. Comparison between observation and simulation model. *Journal of Geophysical Research: Atmospheres*. 2020, **125**(20), e2020JD033194 (cit. on pp. 77, 80).

201. CHILINGARIAN, A; HOVSEPYAN, G. The synergy of the Cosmic Ray and High Energy Atmospheric Physics: Particle Bursts Observed by Arrays of Particle Detectors. *New Astronomy*. 2022, 101871 (cit. on p. 79).

202. BOWERS, Gregory S; SHAO, Xuan-Min; BLAINE, William; DINGUS, Brenda; SMITH, David M; CHAFFIN, Jeff; ORTBERG, John; RASSOUL, Hamid K; HO, Cheng; NELLEN, Lukas, et al. Fair Weather Neutron Bursts from photonuclear reactions by Extensive Air Shower core interactions in the ground and implications for Terrestrial Gamma-ray Flash signatures. *Geophysical Research Letters*. 2021, **48**(6), e2020GL090033 (cit. on p. 79).

203. TECHNOLOGY, Eljen. *EJ-309* [online]. 2022. [visited on 2022-11-22]. Available from: `https://eljentechnology.com/products/liquid-scintillators/ej-301-ej-309` (cit. on pp. 81, 91).

204. CAEN. *DT5730* [online]. 2022. [visited on 2022-11-22]. Available from: `https://www.caen.it/products/dt5730/` (cit. on p. 81).

205. SUN, YK; ZHANG, H; ZHAO, XK; SHAO, M; TANG, ZB; LI, C. Identifying thermal neutrons, fast neutrons, and gamma rays by using a scintillator-based time-of-flight method. *Nuclear Instruments and Methods in Physics Research Section A: Accelerators, Spectrometers, Detectors and Associated Equipment*. 2019, **940**, 129–134 (cit. on p. 93).